CONTROL ELECTRONICS FOR MEMS GYROSCOPES AND ITS IMPLEMENTATION IN A CMOS TECHNOLOGY

A THESIS SUBMITTED TO
THE GRADUATE SCHOOL OF NATURAL AND APPLIED SCIENCES
OF
MIDDLE EAST TECHNICAL UNIVERSITY

BY

BURAK EMİNOĞLU

IN PARTIAL FULFILLMENT OF THE REQUIREMENTS
FOR
THE DEGREE OF MASTER OF SCIENCE
IN
ELECTRICAL AND ELECTRONICS ENGINEERING

FEBRUARY 2011

Approval of the thesis:

CONTROL ELECTRONICS FOR MEMS GYROSCOPES AND ITS IMPLEMENTATION IN A CMOS TECHNOLOGY

submitted by **BURAK EMİNOĞLU** in partial fulfillment of the requirements for the degree of
Master of Science in Electrical and Electronics Engineering Department, Middle East Technical University by,

Prof. Dr. Canan Özgen
Dean, Graduate School of **Natural and Applied Sciences**

Prof. Dr. İsmet Erkmen
Head of Department, **Electrical and Electronics Engineering**

Prof. Dr. Tayfun Akın
Supervisor, **Electrical and Electronics Eng. Dept., METU**

Examining Committee Members:

Prof. Dr. Mübeccel Demirekler
Electrical and Electronics Eng. Dept., METU

Prof. Dr. Tayfun Akın
Electrical and Electronics Eng. Dept., METU

Assoc. Prof. Dr. Haluk Külah
Electrical and Electronics Eng. Dept., METU

Assist. Prof. Dr. Barış Bayram
Electrical and Electronics Eng. Dept., METU

Dr. Said Emre Alper
Technical Vocational School for Higher Education, METU

Date:

I hereby declare that all information in this document has been obtained and presented in accordance with academic rules and ethical conduct. I also declare that, as required by these rules and conduct, I have fully cited and referenced all material and results that are not original to this work.

Name, Last Name: BURAK EMİNOĞLU

Signature :

ABSTRACT

CONTROL ELECTRONICS FOR MEMS GYROSCOPES AND ITS IMPLEMENTATION IN A CMOS TECHNOLOGY

Eminoğlu, Burak
M.S., Department of Electrical and Electronics Engineering
Supervisor : Prof. Dr. Tayfun Akın

February 2011, 129 pages

This thesis, for the first time in literature, introduces a comprehensive study about analog controller designs for MEMS vibratory gyroscopes. A controller of a MEMS gyroscope is mandatory for robust operation, which is insensitive to sensor parameters and ambient conditions. Errors in the controller design not only deteriorate transient performance, such as settling time and overshoot, but also cause performance degradation due to stability problems. Accordingly, true controller design for a gyroscope is critical work in terms of functionality and system performance. This thesis gives details for modeling, analysis of closed-loop systems, and design procedure for drive and sense modes. Controller loops are implemented both with discrete components and in a CMOS technology as an integrated circuit. Simulation and test results verify the modeling, analysis, and design procedure discussed in this thesis.

Drive mode system developed previously at METU is optimized by taking circuit imperfections into account, which results in an improved transient performance of 50 msec settling time with no overshoot for a 4μm drive mode oscillation amplitude. This system has a 60° phase margin with the help of the pole-zero cancellation technique. In addition, a new generation and simple drive mode controller for tactical grade applications is designed and verified with a moderate transient performance.

Two different sense mode controller design procedures are also developed according to a new base-band equivalent model derived for mismatch operation, as a new contribution to the literature. Firstly, a PID controller is designed for low frequency separation between the drive and sense modes of the gyroscope. Secondly, an integral controller is used for moderate and high mismatch amount. The controller system designed with the new base-band equivalent model improves the linearity, angle random walk, and bias instability by factors of 4, 9, and 3, respectively.

Proposed drive and sense mode controllers are also designed and implemented using a 0.6μm standard CMOS process. These chips are the first functional chips developed at METU designed for MEMS gyroscopes. Functionality of the proposed three systems, i.e., conventional drive mode controller, new generation drive mode controller, and sense mode controller, are verified with tests. The first prototypes result in $0.033\ ^\circ/\sqrt{hr}$ angle random walk and $3\ ^\circ/hr$ bias instability for open-loop operation, which is very promising and can be improved even further in future designs.

Keywords: MEMS gyroscopes, drive mode controller, sense mode baseband equivalent model, CMOS controller design, analog force feedback

ÖZ

MEMS DÖNÜÖLÇERLER İÇİN KONTROL ELEKTRONİĞİ VE CMOS TEKNOLOJİSİNDE GERÇEKLEŞTİRİLMESİ

Eminoğlu, Burak
Yüksek Lisans, Elektrik ve Elektronik Mühendisliğ Bölümü
Tez Yöneticisi : Prof. Dr. Tayfun Akın

Şubat 2011, 129 sayfa

Bu tez literatürde ilk defa MEMS dönüölçerler ile ilgili kapsamlı bir çalışmayı sunmaktadır. MEMS dönü ölçerlerde kontrol, sensör parametrelerinden ve ortam koşullarında bağımsız çalışma için zorunludur. Kontrolcü tasarımlarındaki hatalar sistemin geçiş zamanındaki performansını etkilemek ile beraber kararsızlık gibi fonksiyonel sorunlara da yol açabilir. Buna bağlı olarak, doğru kontrolcü tasarımı işlev ve sistem performansı acısından kritik rol almaktadır. Bu tez, sürüş ve algılama modu kapalı döngü sistemleri için modelleme, sistem analizi ve kontrolcü tasarımı konularında detaylı bilgiler vermektedir. Kapalı döngüler hem ayrık elemanları kullanarak, hem de CMOS teknolojisinde tümleşik devreler biçiminde oluşturulmuştur. Simülasyon ve test sonuçları da tezde sunulan modelleme, analiz ve tasarım çalışmalarını desteklemektedir.

ODTÜ'de daha önce gerçekleştirilmiş sürüş modu devrelerden gelen kusurlar da hesaba katılarak optimize edilmiştir. Bu optimizasyonla 4μm sürüş modu hareketi için 50 ms yatışma zamanı ve 0 hedefi aşma sonuçlarına ulaşılmştır. 60° faz marjı kutup-sıfır çıkarma metodu ile elde edilmiştir. Buna ek olarak, orta seviye geçiş performansı için yeni nesil ve basit sürüş modu kontrolcü sistemi taktik seviye uygulamaları için tasarlanmıştır.

Literatürde ilk defa sunulan algılama modunun ana-banttaki eşdeğer modeli kullanılarak, iki çeşit kontrolcü tasarımı geliştirilmiştir. İlk olarak, orantılı-entegral-türetme kontrolcüsü düşük eşlememe miktarı için tasarlanmıştır. İkinci olarak, entegral kontrolcüsü kullanılarak orta ve yüksek miktardaki eşleşmeme miktarı için bir tasarım yapılmıştır. Ana-banttaki eşdeğer model kullanılarak gerçekleştirilmiş olan tasarım ile, sabit kayma kararsızlığında, açı rastgele yürüyüşünde ve doğrusalsızlıkta sırasıyla 3, 5 ve 9 katlık iyileşmeler görülmüştür.

Öne sürülen kontrol sistemleri 0.6μm standart CMOS prosesi için tasarlanmış ve bu tasarımlar ürettirilmiştir. Bu üretilen yongalar ODTÜ'de geliştirilen MEMS dönüölçerler için yapılmış ilk fonksiyonel devrelerdir. Geleneksel sürüş modu kontrolcüsü, yeni nesil sürüş modu kontrolcüsü ve algılama modu kontrolcüsü devrelerinin işlevselliği doğrulanmıştır. 0.033 $^{\circ}/\sqrt{hr}$ açı rastgele yürüyüşü ve 3 $^{\circ}/hr$ sabit kayma kararsızlığı değerleri, açık döngü sistemi için elde edilmiştir. Bu sonuçlar ilk prototipler için çok umut vericidir ve gelecekteki çalışmalarda daha da iyileştirilecektir.

Anahtar Kelimeler: MEMS dönüölçer, sürüş modu kontrolcüsü, algılama modu anabandı modellemesi, CMOS kontrolcü tasarımı, analog güç geri besleme

To My Family

ACKNOWLEDGMENTS

First of all I would like to thank my thesis advisor Prof. Dr. Tayfun Akın for his help, guidance and support during my graduate studies. Starting research career in his MEMS group is invaluable for me.

I would like to thank Dr. Said Emre Aper for his guidance and friendly attitude during endless discussions. Without his guidance and help, this study could not exist. I would also like to thank Assoc. Prof. Dr. Haluk Külah for his helps and suggestions in my academic life.

I would like to thank Erdinç Tatar, my smart research partner, for his valuable suggestions in my research and precious friendship. Special thanks to Mert Torunbalcı for his helps in the fabrication of MEMS gyroscopes used in this study and encouragements for my academic research. I would also like to thank Soner Sönmezoğlu for his worthy helps in my tests.

I would like to express my gratitude to Dinçay Akçören, Cavid Musayev, Uğur Sönmez, Alp Oğuz, Alperen Toprak, and Tunjar Askarlı for fruitful discussions we had on circuit design aspects. I am also grateful to Dr. Murat Tepegöz for his support for CAD environment. Special thanks to Ceren Tüfekçi, İlker Ender Ocak, Şeniz Esra Küçük, Başak Kebapçı, and Ufuk Şenveli for their special friendships. Moreover, I would like to thank all members of the METU-MEMS VLSI research group for providing a nice research environment.

Last but not least, I would like to thank my brother Assist. Prof. Dr. Selim Eminoğlu for his invaluable guidance in my academic and non-academic life; and my parents Ayla and Muhittin Eminoğlu for their endless support and encouragement through all my life.

TABLE OF CONTENTS

CHAPTERS

APPENDICES

LIST OF TABLES

TABLES

LIST OF FIGURES

FIGURES

CHAPTER 1

INTRODUCTION

Understanding the behavior of accelerating systems is a big concern of classical and modern physics. All the laws developed for inertial frames are not valid for accelerating systems which are called non-inertial frames. Human being in a non-inertial frame interprets the effects of acceleration as external forces which validate the laws of motions in these frames. They are called *fictitious forces*, since in a non-accelerating system they do not exist. Most popular example among these forces is *gravitational force, (mg)* which stems from gravitational acceleration. Inertial sensors are used to detect these forces to characterize accelerations. Characterization of accelerations provides tracking of the frame position by integrating the acceleration data without taking any external reference. It is an invaluable work, because external reference can be interrupted or corrupted with external effects, as in global positioning systems (GPS). On the other hand, operational principle of inertial sensors only use very fundamental laws of universe: inertial sensors cannot be interfered by external sources.

In order to track the position, angle of rotation should be tracked besides the amount of translational displacement. Both of these rotational and translational motion cause the objects on the corresponding frame feels a force. Amount of this force directly gives information about these motions. Therefore, measuring these forces enable to extract the information about the amount of translational and rotational motions. This can be accomplished by means of force sensors. The sensor, used to measure a translational motion, is called accelerometer and force used to measure a rotation is called gyroscope.

Gyroscopes are fundamental element for inertial measurement units (IMUs). There are different kinds of gyroscopes: mechanical, ring laser, fiber optic, and Micro-electro-mechanical systems (MEMS) [1, 13, 17]. Even if performances of first three systems are very good, their cost is high, they consume large volume and they are susceptible to shock. On the other hand, MEMS provides very simple solution for gyroscopes with low cost, very small size, and high shock immunity. In recent decade, there were significant research on MEMS gyroscopes. Recent results reach the limits of navigation level gyroscopes which can be used in north seeking [16].

The rest of the chapter is organized as follow: Section 1.1 gives a review for MEMS gyroscopes. Section 1.2 gives the basics of Gyroscope theory. Section 1.3 gives front-end electronics of MEMS gyroscope. Section 1.4 explains the metrics of MEMS gyroscopes. Section 1.5 gives a review of control systems used in MEMS gyroscope which constitute the essence of this thesis. Finally, Section 1.6 gives research objectives and organization of the thesis.

1.1 Review of MEMS Gyroscope

MEMS gyroscope history goes back to early 1980's [13, 17]. According to the actuation and sensing mechanisms, MEMS gyroscopes can be classified into several groups: capacitive, optical, piezoresistive, piezoelectric, thermal, tunneling current, resonant, and magnetic types [13, 18]. Capacitive type micro-machined gyroscopes are the most common type among others, because of easy fabrication, high sensitivity, low temperature dependency, integrability with standard CMOS technologies, and simple read-out electronic requirements [13]. In 1997, a tuning fork gyroscope, canceling linear acceleration, was published for automotive applications [20]. In early 2000's, there were significant improvements in mechanical design, eliminating the coupling between the drive mode and sense modes [21]. Acar and Shkel increased the drive mode bandwidth without sacrificing the gain to have a robust performance in 2005 [22]. In addition to developments in sensor production and mechanical design, there were significant improvements in the circuit and system levels [7, 8, 16, 19, 23], as well. Sharma *et al.* introduced mode-matching circuit with 0.2°/hr in 2009 [19]. In 2008, Ezewke and Boser implemented a mode-matching $\Sigma-\Delta$ closed-loop system with a good performance [7]. Sensonor presented a complete gyro system with a digital control and superior performance which have north seeking capability [16]. Tatar and Alper implemented a complete gyro system with a dynamic quadrature cancellation loop [23]. The recent trend in MEMS is miniaturization of the complete system, combining control of the drive mode, sense mode, quadrature cancellation, and mode matching in a digital processor [16, 32, 33].

Researches at METU makes significant contributions to literature. Alper designed a fully decoupled tuning fork gyroscope having a superior performance, meeting tactical grade specifications [1]. Temiz implemented a complete gyro system including drive amplitude control and open-loop rate sensing [25]. Azgin reported development of a multi masses gyroscope with low g-sensitivity [15]. K. Sahin firstly designed and tested double resonance sense system having large mechanical bandwidth without compromising the sensitivity of the system too much [24]. E. Sahin investigated different actuation mechanisms on the gyroscope performance [2]. Finally, Tatar and Alper designed, implemented, and tested a fully decoupled, tunning fork gyroscope with a quadrature cancellation capability. This gyroscope reached to navigation levels of $0.9°/\mathrm{hr}/\sqrt{\mathrm{Hz}}$ angle random walk and $0.35°/\mathrm{hr}$ bias instability [3].

1.2 Gyroscope Theory

Effects of rotation appears in different forms. Most known forms are centrifugal and Coriolis forces. Centrifugal force is a fictitious force which pushes the objects from the center to outward in the radial direction. The Coriolis force is another fictitious force which stems from the interaction of radial and rotation motions. In this case, different radial positions have different tangential velocities in a rotating platform, since it is proportional to the radius of rotational motion. By the same token, change of the velocity vector due to rotation also differs at diverse radial positions. Thus, if an object tries to move in radial direction, it tends to deviate from this path because its inertia wants to preserve its initial states. On the other hand, it must update its states due to its new radial position. This tendency can be considered as a force which tries to deviate the object from radial path. Figure 1.1 visualizes this tendency where an object tries to move in radial direction, but it departs from its original trajectory indicated with solid line because of this phenomenon. The force causing this departure is called the Coriolis force due to its inventor, Gustave Coriolis (1792 - 1843). The most popular affect of this force is the direction difference of the water flowing through water dispel in the south and north hemispheres. Detailed explanation of the Coriolis force is given in [15]. A mathematical expression of this force can be written as:

$$F_{Coriolis} = 2 \cdot m \cdot \overrightarrow{\dot{x}} \times \overrightarrow{\Omega} \tag{1.1}$$

where, $\overrightarrow{\Omega}$ is an angular velocity, $\overrightarrow{\dot{x}}$ is a radial velocity, and m is an object mass.

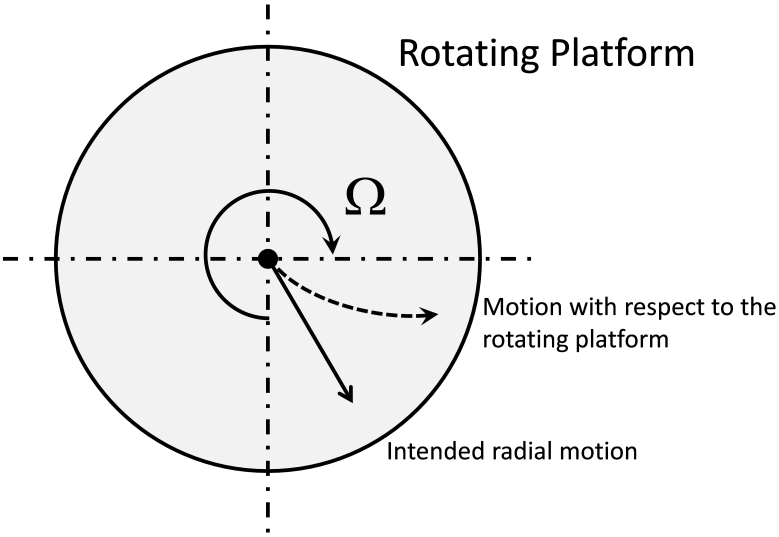

Figure 1.1: Moving object in a rotating platform.

Resultant force's direction is perpendicular to both the rotation and velocity vectors. Moreover, the magnitude of this force is directly proportional to the angular and radial velocity. This result shows that angular velocity can be extracted by measuring the force if the radial motion of the mass is under control; i.e., when its velocity is constant. Angular velocity can also be obtained from measuring centrifugal force, but this force depends on the distance between the object and center of the rotation. This distant is not under control, so it is not feasible to measure the angular velocity by using the centrifugal force.

The gyroscope is a mechanical sensor measuring the angular rate by quantifying the Coriolis force. As it has been mentioned, the Coriolis force is directly proportional to the angular rate. In addition, Eq. 1.1 expresses that the sensor must have a velocity in radial direction in order to induce the Coriolis force. Worded differently, object should move continuously in the radial path to have a certain velocity. This can only be attained by an oscillating motion within a limited area of a sensor. This dynamic of the sensor is called the *drive mode* of a gyroscope.

After the Coriolis force is created with drive mode oscillations, this force can be detected with a force detector. The force detector in MEMS is a basic structure used in different areas. The most popular structure of a force detector is capacitive sensors. The operation principle of this type of a force sensor is firstly based on generating a displacement due to the applied

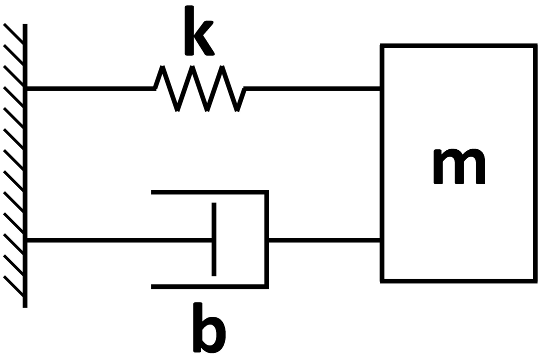

Figure 1.2: Mass-spring-damper behavior of force to displacement process in MEMS gyroscope.

force on a mass. The system characterizing the relation between force and displacement can be considered as a simple mass-spring-damper system, as shown in Figure 1.2. This relation can be expressed as:

$$F = m \cdot \ddot{x} + b \cdot \dot{x} + k \cdot x \tag{1.2}$$

$$\frac{F(s)}{x(s)} = \frac{1}{m} \cdot \frac{1}{s^2 + \frac{b}{m} \cdot s + \frac{k}{m}} \tag{1.3}$$

where, F is the force, x is the displacement, m is the mass, b is the damping factor, and k is the spring constant. In Eq. 1.2 shows a second order system characteristics. It is obvious that if damping of the system (b) is low enough, the system has a very large gain at the resonance frequency. This increase in the gain directly improves the sensitivity of the sensor; therefore, the damping term is tried to be minimized with a proper mechanical design and vacuum packaging. Quality of this low damping term is expressed by the *quality factor (Q)* which is the ratio between the resonance frequency and the bandwidth of the system. The resonance frequency (ω), bandwidth (β), and quality factor (Q) are expressed in the following equations.

$$\beta = \frac{b}{m} \tag{1.4}$$

$$\omega = \sqrt{\frac{k}{m}} \tag{1.5}$$

$$Q = \frac{\omega}{\beta} = \sqrt{\frac{k \cdot m}{b^2}} \tag{1.6}$$

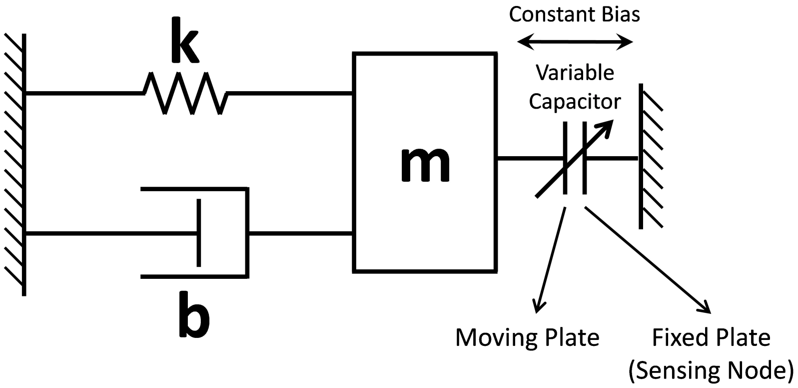

Figure 1.3: Displacement to current process in MEMS gyroscope.

The moving mass is connected to a plate of a capacitor which has a degree of freedom in the axis of the motion to be detected. Other plate is fixed to an anchor which is used as a *read-out* electrode. On that account, when the mass moves due to an applied force, one of the capacitor plate moves. Owing to the this displacement, capacitance changes. Since the voltage across the terminals is constant and capacitance changes, charge accumulated on the capacitor is forced to change, as well. This change causes a current which can be converted easily with a current-to-voltage converter such as a trans-impedance amplifier. The resultant current expression is given in Eq. 1.8. This part of the gyroscope is called the *sense mode*.

$$Q = V \cdot C \tag{1.7}$$

$$I = \frac{dQ}{dt} = \underbrace{\frac{dV}{dt} \cdot C}_{\text{0 for DC bias}} + V \cdot \frac{dC}{dx} \cdot \frac{dx}{dt} \tag{1.8}$$

where, Q is the charge, C is the capacitance, and V is the voltage across the capacitance. In theory, force acting on the sense mass is only due to the Coriolis force; on the other hand, drive mode motions also directly couples to the sense mode owing to the fabrication imperfections [1, 3], even if there is no angular rate. The force generated by this coupling is called the *quadrature force*. A mathematical expression of this force can be shown as followings:

$$F_Q = k_Q \cdot x \tag{1.9}$$

This force is directly proportional to the drive mode displacement, but the Coriolis force is proportional to the velocity of the drive mode displacement. Thus, with a phase sensitive demodulation, it is possible to suppress this force in a considerable amount. Even if this force is tried to be suppressed with a phase sensitive demodulation, there will still be an offset due to the quadrature force. In fact, the offset can be canceled with a simple calibration, but the quadrature force also drifts, which requires an on-line real time cancellation. Otherwise, drift of this force degrades the system performance substantially. As it will be discussed in Chapter 4, it also increases the effect of the phase noise at the output. For this reason, cancellation of this force is urgency for high performance gyroscopes.

Since response of a gyroscope is determined by two independent modes (i.e., drive and sense modes), characteristics of them affect the performance together. The generated Coriolis force is modulated at the drive mode oscillation frequency which is nothing but the drive mode resonance frequency, as it will be discussed later. As a result, frequency of the input signal at the sense mode equals to the drive mode resonance frequency. Since, the sense mode itself behaves as a resonator, the frequency separation between the input and sense mode resonance frequency directly affects the sense mode response. If this amount is very small, the sensor gives a very sensitive response, which is called *matched-operation*, since the drive-mode resonance frequency matches to the sense mode resonance frequency. If this amount is high, then it is called the *mis-matched operation*. The sense mode resonance frequency can be adjusted by a proof mass voltage [1], so there is no need to have different sensor designs for mismatched and matched operations. In addition, the matched operation requires extra control loops, since during the operation drifts in resonance frequencies directly affect the overall system dynamics.

In both drive and sense modes, charge/current to voltage converter is necessary in order to process the mechanical related signals in later stages. This task can be conducted with different types of preamplifiers establishing front-end electronics.

1.3 Front-End Electronics

Amount of the static capacitance ($C_{Sensor,static}$) between the feedback and sensing nodes is very important in sensing of closed-loop systems. In these applications, the feedback voltage of the sensor causes a current flow through the front-end electronics due to the static capacitance between the actuating and sensing electrodes, even if there is no physical input to the system. This response is a pure electrical response, and it is independent from the mechanical response. This zero input response causes several problems. Firstly, there are always errors due to the reading of the electrical response. Non-linearity of the front-end electronics and noise on the actuation voltages are the major reasons for these errors. Amount of these errors directly limit the amount of minimum detectable input of the sensor. Secondly, this electrical response may cause an offset at the system output which decreases the maximum range. Finally, this electrical response also results in functionality problems in some applications. To illustrate, if electrical response is high enough comparing with electro-mechanical response of MEMS resonator, this will prevent the system from locking into the mechanical resonance frequency. Thus, an AC-bridge type interface is used in order to solve these problems by eliminating these errors [30]. This is attained by using an extra reference capacitor which almost equals to $C_{Sensor,static}$. This capacitance and sensor are fed with signals having a 180° phase difference. As a result, in theory at zero-force, the sensor and reference capacitance are same and there is no signal flow to preamplifier including the noises on the actuating signal. In this operation, it is assumed that the sensing node potential is low enough in order to have the same response from the static and reference capacitor in magnitude wise. When a force is applied to the sensor, resultant change in the capacitance yields charge injection, and only this injected charge causes voltage at the preamplifier output. This operation significantly increases the sensitivity of the system. Figure 1.4 shows the configuration of the AC bridge. This configuration is half AC-bridge. In full AC bridge, two sense capacitance is used instead of reference capacitor. On the other hand, in MEMS gyroscopes developed at METU, the mechanical gain is much higher than the electrical response due to two major reasons. 1) There is a large proof mass electrode between actuating and sensing nodes. This large electrode behaves as a shielding, therefore static capacitance between sense and actuating node is very small. 2) MEMS gyroscopes are operating at vacuum, which increases mechanical responsitivity in a considerable amount. As a result, the AC-bridge type is not useful for vibratory MEMS gyroscopes, and the injected current from the sensor is directly sent to the preamplifier. Figure 1.5 shows the equivalent behavior for this case.

The most widespread type of preamplifiers, used in MEMS gyroscope, is the trans-impedance amplifiers (TIA) [27]. These amplifiers convert sensor output current to voltages. The most important advantage of this topology is very low input impedance such that the injected current from the sensor directly enters the amplifier without any loss in capacitance at the node

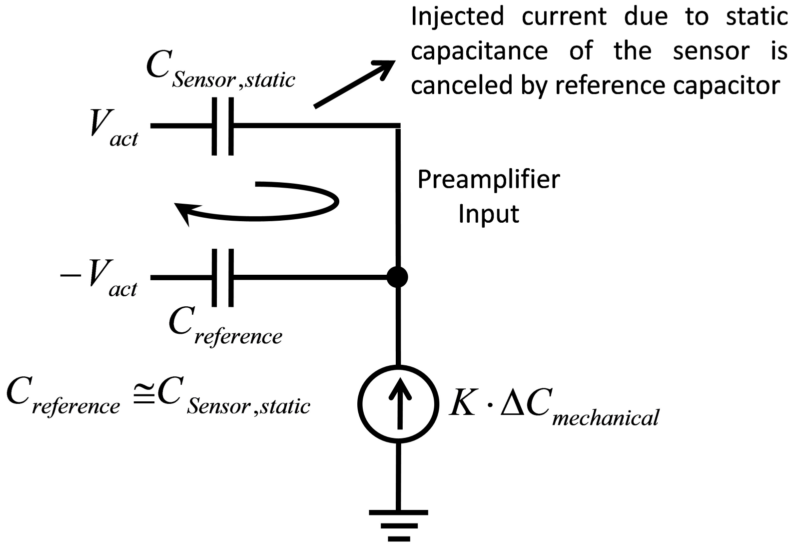

Figure 1.4: AC bridge configuration used in MEMS capacitive inertial sensors.

where preamplifier and sensor connect. This capacitance is mainly composed of the sensor output capacitance, preamplifier input capacitance, and wire-bonding capacitances. Having a low input impedance also ensures that the sensor output is at virtual ground, which is consistent with the assumption of the constant biased sense capacitance in the above derivations. Figure 1.6 shows a typical trans-impedance amplifier. This type of preamplifier can be either capacitive or resistive. Former one is suitable for low noise applications due to lack of thermal noise of resistor. On the other hand, in order to establish DC feedback path in order to operate the Op-Amp in linear region, a large resistor is needed to be used. This is not an easy implementation in ICs. As a result, resistive type TIAs are often used instead of capacitive type TIAs in IC implementations.

Another preamplifier topology is voltage buffer/amplifier type [1, 26]. The injected current from the sensor is converted to a voltage by means of a high impedance, and this voltage is buffered/amplified by means of an Op-Amp. Its major advantage is being low noise if injected current is converted to voltage through a capacitor [26]. In fact, this performance is good comparing to resistive type trans-impedance amplifiers. On the other hand, if buffer type-preamplifier is also implemented with capacitor, these both circuits have same noise performance. In addition, this type of preamplifier has several drawbacks. First of all, parasitic capacitances and input capacitance of the Op-Amp directly degrades the gain and causes

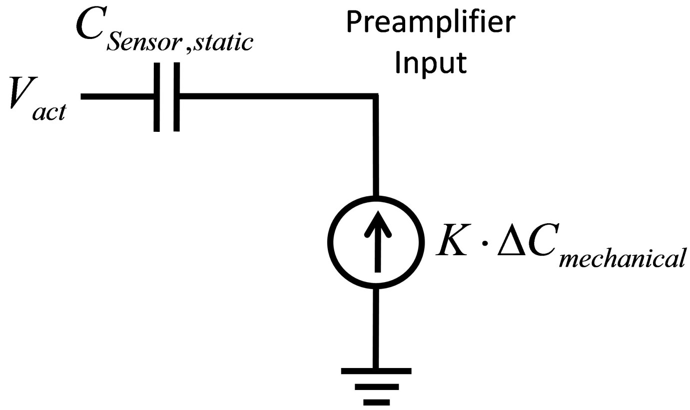

Figure 1.5: Direct injection without a reference capacitor.

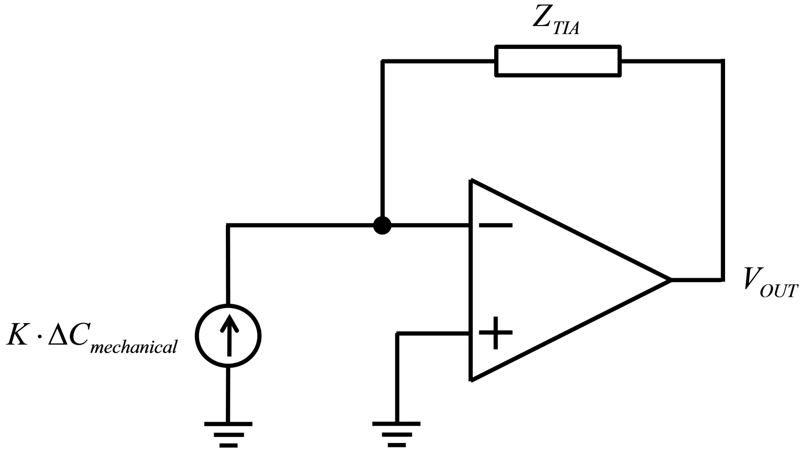

Figure 1.6: Trans-impedance amplifier used in MEMS capacitive sensors.

phase-error which results in problems in signal processing stages. In addition, implementing high-impedance node is not practical in CMOS. Figure 1.7 shows this type of preamplifier.

Switch capacitor type preamplifiers are often used in sampled-data system such as $\Sigma - \Delta$ type controllers [26]. In fact, this topology is nothing but a capacitive type TIA. Contrary to continuous time's version, DC path is provided periodically by resetting the integration capacitance instead of using huge resistances. Operation of this topology is simple: injected current from the sensor is integrated within an integration time. Then, the integrator capacitor is reset. It is an effective method, but the kT/C noise is significant noise source in these types since the sense capacitance used in integrator is pretty low. In order to alleviate this,

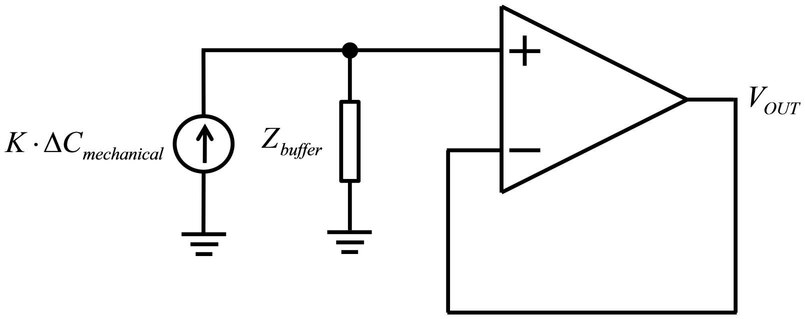

Figure 1.7: Buffer type preamplifier used in MEMS capacitive sensors.

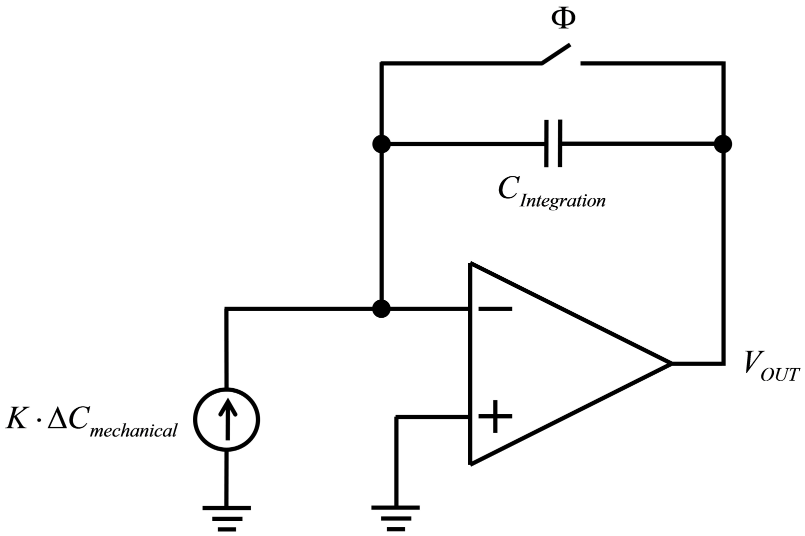

Figure 1.8: Switch-capacitor type pre-amplifier.

correlated-double-sampling (CDS) method is used. Figure 1.8 shows switch capacitor type pre-amplifiers. For continuous time operation, first two types of system are the most commonly used blocks. Buffer type preamplifier has several drawbacks, but it has better noise performance comparing with resistive type TIAs. On the other hand, off-chip resistors enable using continuous time capacitive TIAs. In that, this type of preamplifier is the best candidate for pure analog systems.

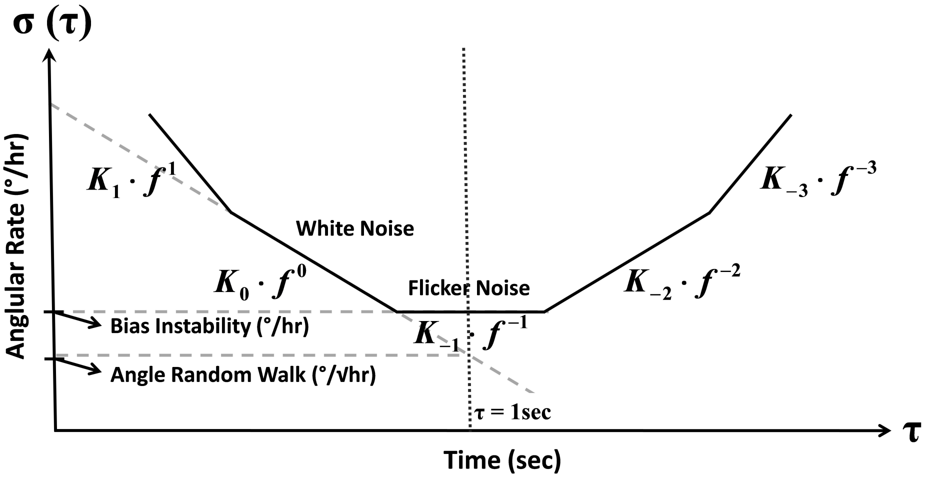

Figure 1.9: Allan variance plot.

1.4 Metrics of MEMS Gyroscopes

Inertial sensors are essentially integrating sensors, and they have no external reference. This property results in integration of instantaneous errors at the output. As a result, noise performance of these sensors depends on the operation length. Expected deviation after this integration also depends on type of noise process. For example, the deviation due to the white noise process after the integration increase with square root of operation length; on the other hand, drift due to Flicker (1/f) noise increases directly with operation length. In a generic system several noise processes take role in the total drift. Especially, noise processes which are effective in low frequency band are very important for long operation length. Therefore, characterizing these noise sources is a valuable task. Use of *Power Spectral Density (PSD)* is not an effective method to characterize them, because power of these noise source becomes very large in very low frequency region which makes impossible separating the different noise processes. In inertial sensors, Allan Variance is used to estimate the total drift after integration: it directly shows estimated drift per operation length. In addition, it also provides characterization of slow noise processes which cannot be performed with standard PSD [28]. Figure 1.9 shows a typical Allan Variance plot.

In tactical grade applications, white noise process and Flicker noise process are two main sources which dominate total drifts, since operation length is not so high. In inertial sensors, metrics for characterizing white noise and Flicker noise are angle random walk and bias instability, respectively. Unit of angle random walk is $°/\sqrt{hr}$, and unit for bias instability is $°/hr$. Drifts due to these process can be found easily by multiplying bias instability with operation length and angle random walk with square root of operation length. Relation between the noise densities for different processes and Allan Variance plot are given in Table 1.1 [34, 35]. These relations are given for single sided PSD and continuous time Allan Variance.

Table 1.1: Allan Variance statistics for different noise processes [34].

Noise Process	$S_Y(f)$	$\sigma^2(\tau)$
Angle Random Walk	$K_0 \cdot f^0$	$K_0 \cdot \frac{1}{2\tau}$
Bias Instability	$K_{-1} \cdot f^{-1}$	$K_{-1} \cdot 2ln(2)$
Rate Random Walk	$K_{-2} \cdot f^{-2}$	$K_{-2} \cdot \frac{2\pi^2\tau}{3}$

It was mentioned that the bias instability is the measure of the Flicker noise, but this statement is not correct for a generic case. Bias instability is the minimum amount of drift per operation length [36]. Therefore, other drift processes such as as rate random walk, may dominate Flicker noise. Therefore, bias instability is the point in Allan Variance plot where drift due to the slow noise processes (e.g., rate random walk) becomes comparable with drift due to the fast noise processes (e.g., white noise). In Allan Variance plot, bias instability is the minimum value of the curve. On the other hand, angle random walk is the value of the white noise trend line at $\tau = 1sec$, as Figure 1.9 shows.

Other significant metrics for MEMS gyroscopes are full scale range, non-linearity, settling time, and bandwidth [29]. The full scale range tells the difference between the maximum and minimum signals which can be read. Non-linearity describes the linearity of the relation between the gyroscope output and angular rate. Settling time is another significant parameter characterizing start-up time of a gyroscope. In some of the applications (e.g., tactical grade) the operation length of time is just tens of seconds. As a result, the start-up time is important for these applications. Finally, the bandwidth characterizes the maximum frequency of the angle rate that system can give response.

MEMS gyroscopes can be classified into several groups according to their performances which are briefly discussed above. Table 1.2 shows the major performance parameters for these gyroscopes.

Table 1.2: Different classes of gyroscopes [54].

Parameters	Rate Grade	Tactical Grade	Inertial Grade
Bias Instability ($^\circ/hr$)	10-1000	0.1-10	<0.01
Angle Random Walk ($^\circ/\sqrt{hr}$)	>0.5	0.5-0.05	<0.001
Full Scale Range ($^\circ/sec$)	50-1000	>500	>400
Bandwidth (Hz)	70	~100	~100

1.5 Controllers in MEMS Gyroscopes

Control of the drive and sense modes is a significant task in a MEMS gyroscope not only for functionality, but also for a good performance. Since gyroscope is an electro-mechanical system, feedback signal in the closed-loop system should be converted to force. This type of feedback is called *electrostatic feedback*. The voltage-to-force conversion comes from the conservation of energy, as it is shown in [1]. Expression between voltage and force can be written as:

$$F = V_{PM} \cdot \frac{\partial C_{act}}{\partial x} \cdot V_{act} \tag{1.10}$$

where, C_{act} is the capacitor used for actuation, and V_{PM} is the proof mass voltage used to bias the actuation and sensing capacitances.

Controllers in MEMS gyroscope need to carry out several tasks: self-oscillation in drive mode, regulation of drive and sense motions.

Drive mode oscillations can be generated externally. Critical point is that amplitude of drive oscillation is needed to be maximized in order to increase the sensitivity of the overall system. This can be achieved by actuating drive mode with large voltages but this will increase the electrical coupling to sense mode which will degrade the operation. Therefore, actuation of drive mode is needed to be carried out with small signals. It cannot be attained if oscillation frequency does not equal to the resonance frequency of drive mode dynamics expressed in Eq. 1.11 [2].

$$H_{drive,OL}(s) = \frac{V_{drive,out}}{V_{act}} = \frac{K_{drive} \cdot s}{s^2 + \beta_D \cdot s + \omega_D^2} \tag{1.11}$$

As it will be discussed in Chapter 4, large quality factor improves noise performance of the system. Thus, MEMS gyroscope are preferred to operate at vacuum. Gyroscopes used in this thesis have a quality factor (ω_D/β_D) larger than 30000 for drive modes. This large value neces-

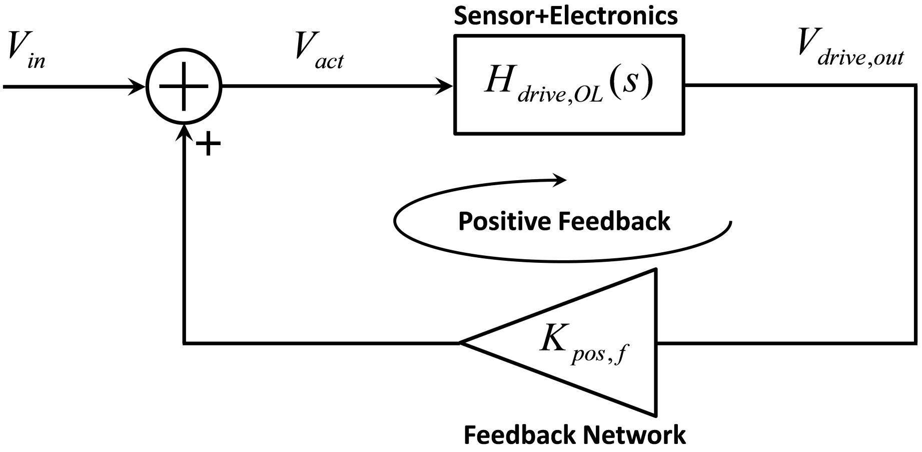

Figure 1.10: Positive feedback loop used as a self-oscillation loop in the drive mode.

sitates very low bandwidth (β_D). External matching, therefore, is not so easy and impractical. Instead of external excitation, self-oscillation loop is constructed to lock into the drive mode resonance frequency. Self-oscillation is performed by constructing a positive feedback with a very large open-loop gain as shown in Figure (1.10). Mathematics of positive feedback can be expressed as followings:

$$H_{drive,pos} = \frac{V_{drive,out}}{V_{in}} = \frac{H_{drive,OL}(s) \cdot K_{pos,f}}{1 - H_{drive,OL}(s) \cdot K_{pos,f}} = \frac{K_{drive} \cdot K_{pos,f} \cdot s}{s^2 + \left(\beta_D - K_{pos,f}\right) \cdot s + \omega_D^2} \tag{1.12}$$

If the positive feedback gain ($K_{pos,f}$) equals to the bandwidth of the drive mode (β_D), then system is at the edge of stability. In other words, it has a sustain oscillation at drive mode resonance frequency. If positive feedback gain is larger than the bandwidth, system has a growing oscillation until electronics saturate. Output of the feedback network is square wave at saturation, but high-Q filter characteristic of drive mode rejects harmonics of the square wave rather than fundamental harmonic at drive mode resonance frequency. After electronics saturate, system has a sustain oscillation as in the former case. In fact, loop gain drops to unity at saturation since gain of positive feedback network decreases: the ratio between input and output of feedback network reduces. The easiest implementation of the positive feedback network only requires a comparator which has a very large feedback gain before saturation.

In addition to the self-oscillation loop, velocity of the drive mode must be under control in order to have a certain relation between angular rate and Coriolis force. Otherwise, actuating the sensor with a constant voltage (saturation level of positive feedback network) yields an oscillation depending on sensor parameters and ambient conditions. In addition, settling time of drive oscillation takes a plenty of time exceeding tens of seconds if drive mode oscillation is not regulated. These requirements obligate drive mode control. By the same token, open-loop rate sensing has several drawbacks. Firstly, performances of the sensor depend on sensor and ambient conditions. This results in short and long term drifts. Secondly, sensing mechanism of sense mode of gyroscope is non-linear: responsivity changes with larger displacement [1]. Finally, bandwidth of the sense system needs to meet certain specifications for certain applications. These three limitations of sense mode can be alleviated by means of a controller. In summary, control must be performed for both drive and sense modes.

1.5.1 Drive Mode Controllers

Stability of the drive motion is very critical in terms of short and long term operations. Coriolis force directly depends on the amplitude of drive oscillation: any drift and instability on drive oscillation cause drifts and instability at the output. In addition, settling time of drive oscillations should be minimized to shorten the overall start-up time of MEMS gyroscope system. Quality factor of the sensor is very high in order to have less mechanical noise. If drive motions are not under control, settling time of the sensor will be above tens of seconds. On the other hand, for tactical grade applications, settling time of the system should be kept below a few hundreds of milliseconds. Regulation of the drive amplitude is also significant for a good bias instability and robust scale factor which is independent from sensor parameters and ambient conditions.

In literature, there are several approaches for drive mode control. Pure analog controllers are often preferred due to their simple implementation and simple design procedure [3, 12, 21, 42, 47]. In these works, proportional-integrator (PI) controller is mostly used. Besides, for these controllers it is concluded that there is a trade-off between fast settling and the stability of the system because of the low frequency pole coming from the drive mode envelope model. Stability of the system directly affects the overshoot and the ringing of the closed-loop system. For this reason, in order to have a sufficient phase margin such that the overshoot of the system is in a tolerable amount, loop gain is needed to be low for these systems. On the other hand, this results in very large settling times. In literature, same design procedure is also applied for a digital controller; settling time is a few hundreds of milliseconds for this system, as well

[43]. In order to cope with this trade-off, there are modified drive mode controller systems increasing the complexity. There is a semi-analog system whose settling process is carried out by a large proportional controller [44]. Since there is no integrator, there is no important stability problem. When the amplitude of the drive mode oscillation is around the vicinity of the desired level, system switches to PI mode to have a good amplitude regulation due to the zero steady state error of the systems including integrator. However, at steady state there is an undesired oscillation because of switching dynamics. There is also a high performance digital controller which uses *active disturbance rejection control* with an advanced controller implemented in FPGA [45]. Settling time of this system is just a few tens of milliseconds, but the proposed system is quite complex owing to its digital implementation. There are also PLL-based self-oscillation loops reducing the phase errors and phase noise of the drive mode system [42,46]. These deterministic and stochastic errors degrade the overall system performance if they are not small enough. Finally, the $\Sigma - \Delta$ modulator type controller is also reported for the drive mode controller, but use of such a system is not practical for drive mode [41]. Finally, there is a universal topology which can operate in a wide range of sensor parameters and ambient conditions [31] by using a current commutating switching mixer. Same complexity is valid for this system, as well.

Even if, there are a lot of works about analog drive mode controller designs for last two decades, a complete and correct analytical design procedure has not been presented up to now. Trade-off between settling time and overshoot mentioned in literature can be easily be tackled with correct design procedure which will be discussed in details in Chapter 2. Therefore, modified topologies increasing system complexity are not necessary for low settling time and robust operation. Although supply limitations of the electronics are mentioned in [42], in literature non-linear behavior of the electronics has not been analyzed in details. This topic is also investigated in Chapter 2.

1.5.2 Sense Mode Controllers

Sense mode is the most significant portion of MEMS gyroscope, because rate information flows through this loop. Any noise source and stability problems in this loop directly couple to the output. Open-loop rate sensing is a simple solution for sense mode electronics; however, linearity, bandwidth and settling controls are not possible for it. Furthermore, open-loop rate sensing is susceptible to sensor parameters which vary with sensors and ambient conditions. This results in poor bias repeatability and bias instability for long term operations.

Closed-loop rate sensing is mandatory for high dynamic range, otherwise responsivity of sense mode to angular rate changes considerably for large amount of angular rate due to the highly non-linear characteristics of varying-gap type capacitive fingers in sense system. In literature, there are basically three types of controllers in sense mode: 1) Pure analog controller [2, 5, 6, 14]. 2) $\Sigma-\Delta$ modulator type controllers [7, 8, 9]. 3) Digital controllers [11, 16, 33]. Firstly, pure analog system is a simple solution for sense control. Mature techniques developed for continuous-time system provide analytical design procedures and very strong verification environments for this method. Secondly, $\Sigma-\Delta$ modulator type controller is a very common technique for MEMS inertial sensor control. In this technique, sense resonator is utilized as a second order integrator of the $\Sigma-\Delta$ modulator. Its output is inherently digital that is the most appealing side of this type of controller. A decimation filter is sufficient to extract the angular rate information. Finally, digital controller provides smart controller implementation that can be configured for a wide range of sensor parameters. Different types of control loops can be embedded in one controller giving the optimum solution. In addition, it also enables to insert signal conditioning algorithms into the micro-controller. These algorithms may improve the system performance further. Unfortunately, this type of controller requires ADC, DAC and a moderate performance micro-controllers. Design and implementation of such a system are quite complex comparing with previous systems.

Among these three systems, $\Sigma-\Delta$ modulator type controllers is the most prominent type because of its simplicity and inherent digital output. In this type of controllers, feedback signal is not analog, it is *pulse density modulated* (PDM) signal. This feedback is mandatory for MEMS capacitive accelerometers, because feedback factor in these sensors is highly non-linear: the amount of the feedback force directly depends on the square of the actuating voltage. For this reason, analog force feedback cannot be used in capacitive type MEMS accelerometers for a reasonable linearity. On the other hand, feedback factor is linear in MEMS gyroscopes, and $\Sigma-\Delta$ is not the only solution, as it was mentioned above.

MEMS vibratory gyroscope are operating at drive resonance frequency in contrary with accelerometers working at base-band. This difference prevents use of low-pass $\Sigma-\Delta$ modulators in MEMS gyroscope. Otherwise, sampling rate should reach very high frequencies to obtain high over-sampling ratio for having low quantization noise. In that, band of interest is itself around 10 kHz for a typical MEMS gyroscope in literature. Band-pass type $\Sigma - \Delta$ modulators are used in MEMS gyroscopes in order to relive this speed challenge in electronic design. In that type of modulators, sharp magnitude characteristics of the band-pass filters, which can be considered as resonators, rejects quantization noise in a considerable amount. Although, over-sampling ratio is not high, this filtering provides high resolution. In MEMS, mechanical sensor can be used as resonators. Nevertheless, its noise rejection performance is only valid for a narrow band. Extra electronic resonators are necessary in order to obtain better quantization noise rejection in a sufficient band. These electronic filters reduce the integrated noise before quantizer, as well, so that signal dependent gain of integrator increases. Correspondingly, input referred noise decreases. If these resonators are not used, quantization noise will result in poor performance. These electronic filters and mechanical resonator form $\Sigma - \Delta$ modulator. Mode-matching circuitry is required to utilize the mechanical sensor as a resonator, otherwise all resonators must be implemented in electronic domain. There are good results for systems using fourth order $\Sigma - \Delta$ modulators in sense control whose two order comes from mechanical sensor and other two order comes from electronic implementation [19].

Problem of a $\Sigma - \Delta$ modulator type controller is the lack of modeling of its exact behavior. Design procedures of this type of controller rely on a set of rule of thumbs coming from experimental results. There is no analytical design procedure, since this system is highly non-linear. Because of analysis difficulty of $\Sigma - \Delta$ modulators, careful simulations should be performed for a true prediction of stability. Stability of MEMS gyroscope is not only important for functionality, but also for settling performance which is critical for tactical grade applications. In addition, stability of $\Sigma - \Delta$ modulators strictly depends on sensor parameters, such that controller is needed to be updated carefully for each sensor. In brief, use of $\Sigma - \Delta$ type controller has a few limitations in terms of controller design and implementations. On the other hand, it is still a good candidate for being a controller owing to its digital output.

Analog force-feedback is a simple system and its output is at base-band. As a result, digitization at analog output is much simpler at base-band than digitization at drive resonance frequency. Over-sampling based analog-to-digital converters (ADC) can be used easily, since bandwidth of the output is very low. Best candidate for this type of ADC is $\Sigma - \Delta$ modulator ADC. Low bandwidth allows simple $\Sigma - \Delta$ architectures to digitize analog output with very high accuracy. Thus, a hybrid system composed of analog controller and simple second order low-pass $\Sigma-\Delta$ type ADC combines all the advantageous of analog controller and digital output of $\Sigma-\Delta$ type controllers. Robust and mature controller design procedures for analog system enables the designer to understand the system in details and make optimizations basing on analytical approaches. In addition, use of ADC provides digital output. Second order electronic low-pass $\Sigma-\Delta$ type ADC topologies is simpler than the fourth order electro-mechanical band-pass $\Sigma-\Delta$ modulators. Therefore, complexity of this resultant system is not more complex than complete higher order band-pass $\Sigma-\Delta$ type controllers. Furthermore, this system eliminates all the disadvantageous of $\Sigma-\Delta$ type controllers coming from its complex behavior. On the other hand, in this system $\Sigma-\Delta$ ADC works after the controller, so it has no effect on controller performance. Sensor dependency of the complete system can be minimized with a true controller design. $\Sigma-\Delta$ modulator for such a system is a pure electronic modulator which is a mature topic in electronics, as well. Very high performance with high over-sampling ratio can be obtained with even second order $\Sigma-\Delta$ modulators, since bandwidth is low.

Analog controller can be applied with two different approaches: 1) wide band controller 2) narrow band controller [49]. In the former controller, front-end electronics output, which is around drive mode resonance frequency, directly feeds the controller. In this type, analog controller operates around drive mode resonance frequency [2, 5, 49]. Even if implementation is very simple, this architecture has several drawbacks. Firstly, regulation strength is poor, since it is almost impossible to have a zero steady state error owing to the operation at drive mode resonance frequency. Regulation strength can be improved by increasing proportional controller gain; on the other hand, this will lead significant stability problems. In addition, regulated signal is not only the Coriolis force, but it is a combination of quadrature and Coriolis force. As a result, feedback signal not only composed of rate signal, but also quadrature signal. In a typical gyroscope, amount of quadrature signal reaches to a very high value which is comparable with the maximum input rate signal. This will reduce the maximum detectable rate in a substantial amount for wide band controller. Finally, any phase error in this loop directly hardens to distinguish the rate signal from the quadrature signal [49]. In brief, this type of controller is not effective, because control operation is not carried out in the band of interest.

In narrow band controllers, control operation is performed in the band of interest [6,49]. In addition, input of the control signal comes from the phase sensitive demodulation output;

therefore, it is free of the quadrature signal. Effective controllers can be implemented, since the input of the controller directly gives information about the sense mode motion. With these controllers, it is possible to have a very good regulation of sense mode motion by using an integrator based controller. In addition, this topology only includes an extra modulator which is not necessary in the wide-band controller. This modulator can be implemented with simple switches, as it will be shown in Chapter 4. In other words, implementation complexity is almost same with the wide-band controller. To conclude, this type of controller is much more effective comparing with the wide band controller.

Even if narrow band analog controller seems a simple and effective solution, sense system of vibratory MEMS gyroscope is not linear-time-invariant (LTI). Sensor and front-end electronics operate at the drive mode resonance frequency, whereas controller takes role at DC band. In literature, there are studies for sense mode analog controller designs basing on *modern control theory*. Most of these works focus on *adaptive* controllers [11, 50, 51] and *robust* controllers [52, 53]. The fundamental scope of these controllers is to have a robust system which is insensitive to fabrication imperfection and environmental variations. Design procedures in modern control theory are very effective for non-linear systems, multi-input/multi-output (MIMO) systems, and multi-loop systems [48]. On the other hand, proposed analysis and design procedures require careful modeling and design work. These design approaches prevent developing an intuition for understanding the system dynamics. In addition, careful simulation is needed to be carried out in order to identify systems in details [48]. These problems are almost same as the problems encountered in $\Sigma - \Delta$ modulator type controller. Furthermore, implementation of these controllers with analog electronics is difficult.

On the other hand, it is possible to transform the sensor and front-end electronics dynamics into base-band, as it is achieved in drive mode controller designs. Due to this transformation, the resulting system is completely LTI. LTI systems which is single-input/single-output (SISO) and composed of single loop can be analyzed easily using *classical control theory*. Moreover, simple, robust, and very effective design procedures can be developed by using the mature techniques used in classical control theory. In this theory, frequency domain and s-plane provides invaluable intuition for understanding the system dynamics in details [48].

In literature, base-band transformation has been carried out for gyroscopes operating at matched conditions requiring advanced control; on the other hand, there is no detailed study for the controller design [6]. There is also a work giving a generic envelope behavior of MEMS gyroscope [10]. Nevertheless, the proposed model is too generic, and it is not linear. Controller design approach in this work necessitates complicated analyses, as well. To summarize, in literature there is no simple and LTI model characterizing the envelope behavior of the MEMS gyroscope operating at mismatched conditions. In addition, there is no analytical design procedure developed for LTI sense mode systems operating at matched and mismatched conditions.

1.6 Research Objectives and Thesis Organization

The main goal of this study is to characterize the drive and sense mode closed-loops, design controllers for them, and implement the controllers in a CMOS technology. The specific objectives can be listed as follows:

1. Optimization of the drive mode controller. Transient performance of drive oscillation is critical for tactical grade applications. The drive mode controller should work with an enough safe margin at the steady state such that the system is robust to change in ambient conditions and aging of the product. Controller design procedure should take imperfections coming from the implementation into account for the optimum performance.

2. Sense mode controller design. For a linear operation in a wide range, the sense mode motion should be controlled. In addition, a correct design approach is needed to be developed, otherwise system may have significant problems regarding functionality and performance. Base-band equivalent models of the sense dynamics should be derived in order to follow an analytical design procedure. For the best performance, closed-loop rate sensing should be analyzed in details.

3. Performance analysis. Performance analysis should be carried out in details. Noise characteristics of the non-linear elements such as switching modulators should be studied. Effects of the feedback on the system performance are needed to be analyzed.

4. Implementation and Tests: The proposed controller approaches should be verified with tests. Effect of the control parameters over the system performance is needed to be in-

vestigated. Functionality and noise performance of the implemented CMOS controllers should be verified. Discrepancies should be discussed.

The organization of the thesis and the contents of the following chapters are as follows.

Chapter 2 introduces a complete design procedure for drive mode amplitude control. Circuit imperfections are taken into account and resultant non-linear system is optimized. Finally, a new simplified, moderate performance control loop is introduced. Simulations of that system are conducted.

Chapter 3 gives, firstly in literature, base-band model for sense dynamics for mismatched operation. Analytical design procedure is also developed using this model. Bandwidth and transient performance are optimized. Models and analytical controller design procedures are verified in simulations.

Chapter 4 gives the CMOS implementation of the controller. Detailed system level noise analysis is performed. A non-linear effect of the modulator on the noise behavior of closed-loop system is discussed. Output noise and input referred noise expressions are derived for the closed-loop system, and secondary noise sources are studied.

Chapter 5 gives test results. Functionality of the CMOS chips are verified. Effects of the controller design on the system performance are also discussed. In addition, performance of the chips are given, and discrepancies are discussed in details.

Finally, Chapter 6 summarizes the complete work and future research topics are given.

CHAPTER 2

DRIVE MODE CONTROLLER

The drive deflection directly affects the performance of a MEMS gyroscope because both Coriolis and quadrature force are directly proportional to the drive mode displacement. Therefore, stability of the drive motion is very critical for both short term and long term stabilities such as the bias instability and scale factor repeatability, respectively. Drive mode of a MEMS gyroscope is very high-Q system which can easily enter self oscillation with a positive feedback loop. Positive feedback limits the actuating voltage to a certain value, which determines the amount of actuating force applying on the drive mode mass. Even if this force is not much sensitive to ambient and process variations, the deflection of the mass due to the drive actuating force is very susceptible to vacuum level, temperature, and process variations. As a result, the amount of the drive oscillation amplitude must be under control instead of controlling the actuating voltage. Organization of this chapter is as follows. Section 2.1 discusses the closed-loop drive mode system and develops a controller design procedure with an optimum transient performance for an ideal LTI system. Section 2.2 explains the effects of circuit imperfections on system behavior and modifies the design procedure according to these effects. Section 2.3 gives a new generation simplified drive mode controller. Section 2.4 summarizes this chapter.

2.1 Drive Mode Controller

The idea behind the conventional solution for the drive amplitude regulation loop is very simple: amplitude of drive deflection is firstly detected by means of an envelope detector. The amount of this voltage is then compared with a reference voltage and the error signal feeds the controller. Finally, the output of the controller is modulated at the self-oscillation frequency and this modulated voltage is fed back to mechanical sensor. At steady state, the

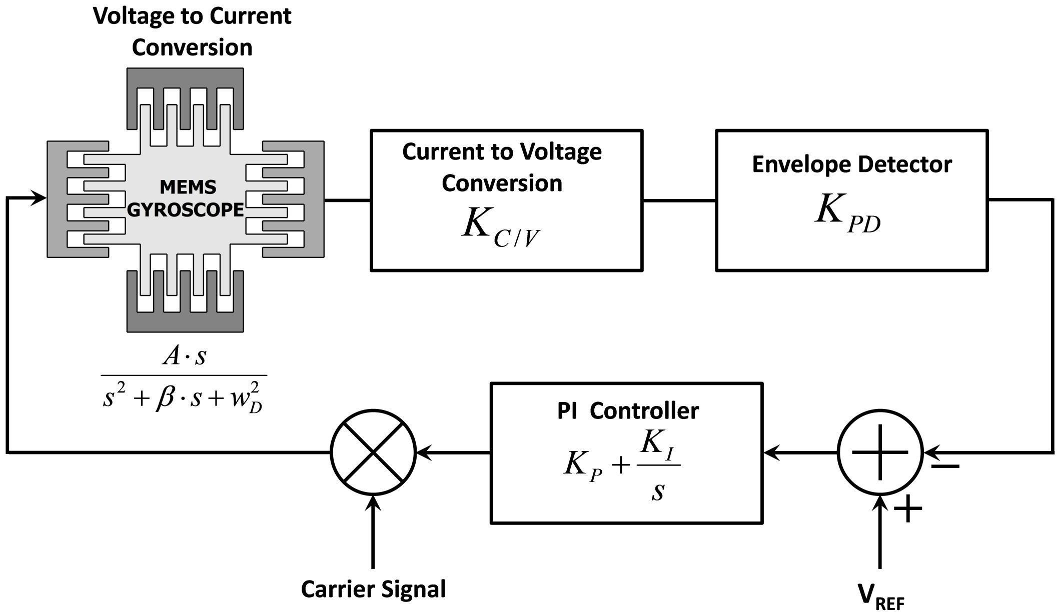

Figure 2.1: Conventional drive mode system.

error signal goes to very low values; therefore, amount of the deflection is regulated by the reference voltage. In fact, the regulated parameter is not drive displacement, but its derivative which is the velocity of the drive motion. On the other hand, Coriolis force is proportional to the velocity, not drive displacement. For this reason, regulation of the drive mode velocity is more effective method instead of the regulation of the drive mode displacement: change in frequency does not affect scale factor. On the other hand, bias is mainly determined by the quadrature force that is proportional to the drive mode displacement in contrast to Coriolis force. As a result, the instability of the frequency directly affects this parameter. This will lead a significant problem in terms of bias instability for a typical gyroscope system, but cancellation of quadrature force solves this problem [3].

Controller design is very significant in terms of system stability. There are three significant issues for the controller design: steady state error, over shoot and settling time. Firstly, steady state error is critical for the drive amplitude regulation. The amount of the steady state error directly indicates the strength of the controller. In order to reduce this error, loop gain is needed to be increased as much as possible. The best solution for reduction of steady state error is using integrator based controller such that its gain at DC (steady state) is infinite therefore steady state error is zero. Secondly, over shoot is another parameter for drive mode controller. This parameter is very important for the operation in which large drive displacement is required for better performances. Since the sensitivity of MEMS gyroscope is directly proportional to the drive mode oscillation amplitude, performance will be improved with larger drive mode deflection. As a result, the maximum amount of deflection is limited by the sensor design and over shoot. In other words, the amount of the over shoot is needed to be minimized. Finally, the settling time of the drive mode oscillation should be minimized for the tactical grade applications whose operation time may be needed be below a few tens of seconds considering the possible delays coming from other loops.

Figure 2.1 shows the block diagram and Figure 2.2 shows the simplified circuit level diagram of the conventional drive amplitude control system . The system portion between the modulator and demodulator, which operates around the drive mode resonance frequency, but other portion operates at baseband. In other words, the complete system is not a LTI system and its analysis and controller design are not straightforward, owing to the lack of LTI analytical analysis and design methods. On the other hand, only the envelope behavior of the modulated system is under interest instead of its complete characteristics. Therefore, envelope model of the modulated system is used instead of the complete system model as summarized in Figure 2.4. Derivation of the envelope model can be performed in either time domain or frequency domain. Frequency domain envelope model derivation will be discussed in Chapter 3. Envelope model derivation of a sense mode dynamics in time-domain for matched-condition is given in [4]. This case is identical for the drive mode dynamics.

Drive mode system shown in Eq. 2.1 has the envelope model shown in Eq. 2.2

$$H(s) = \frac{A \cdot s}{s^2 + \beta \cdot s + w_D^2} \tag{2.1}$$

$$\tilde{H}(s) = \frac{1}{4} \cdot \frac{A}{s + \frac{\beta}{2}} \tag{2.2}$$

Open-loop gain of this system has a low frequency pole which degrades the bandwidth of the closed-loop system. In fact, low bandwidth does not directly reduce the bandwidth of the system. On the other hand, in order to increase the bandwidth of a closed loop system, gain is needed to be increased. This gain causes instability because of the poles coming from the envelope model, integrator used to have a zero state error, and low pass filter used in demodulator. Owing to the fact that, gain is increased to decrease settling time and phase drops

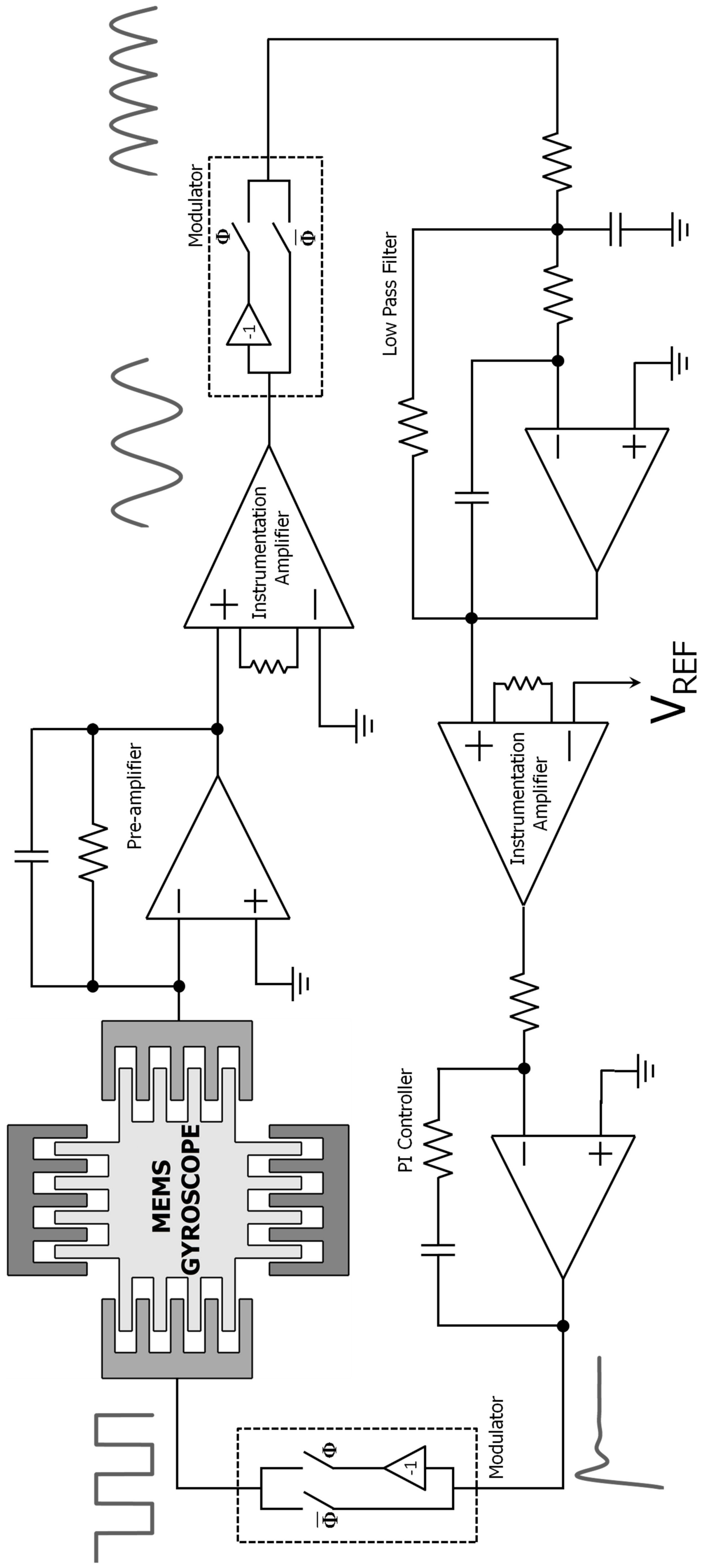

Figure 2.2: Simplified circuit level diagram of the closed-loop drive mode system.

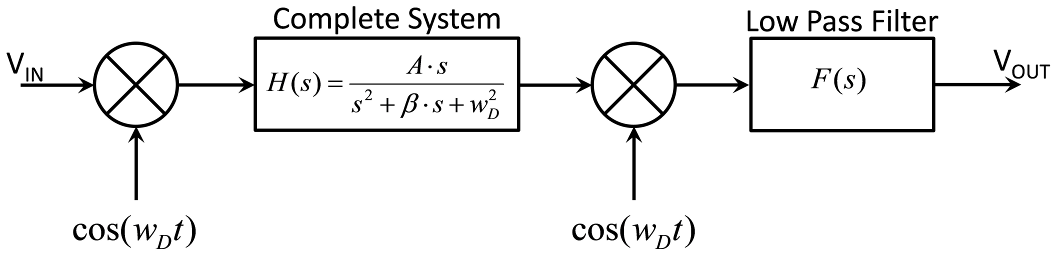

Figure 2.3: Complete drive dynamics.

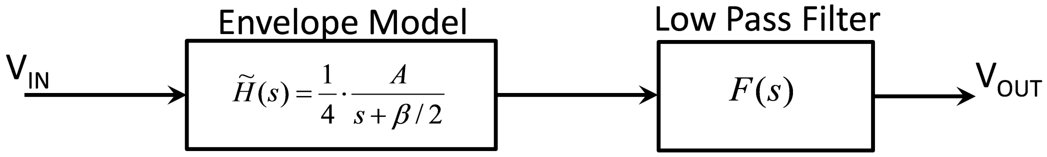

Figure 2.4: Envelope model of drive mode dynamics of MEMS gyroscope.

due to these poles, the phase of the open-loop system is very low at the unity gain frequency. To illustrate, assume that bandwidth of the closed loop system is desired to be 50 Hz which roughly corresponds to tens of millisecond settling time. Besides, phase contribution of the low frequency pole coming from the envelope model, which is smaller than 1Hz for low settling time, and integrator reaches 90° even for very low frequencies. Therefore, phase drop of the open-loop system reaches 180° at unity gain frequency, that should be much higher than 1Hz (envelope pole), excluding low pass filter phase contribution. Taking the effect of the low pass filter into account, total phase drop exceeds 180°, which is the critical value for stability. This handicap for stability hinders using large loop gain for better settling time, such that open loop gain should drop to unity around the envelope pole. Therefore, settling time of the overall system cannot be smaller than hundreds of milliseconds with a sufficient phase margin. In brief, a pure integrator is a poor controller in terms of transient response. To improve the transient response to a step input, the low frequency pole coming from envelope model should be canceled with pole-zero cancellation. PI controller is an effective method to achieve it. With this controller, not only is the low frequency pole of the system envelope canceled, but its integrator behavior reduces the steady state error to zero.

Controller design procedure; therefore, is mainly composed of two major steps: 1) Pole-zero cancellation to enable low settling time with sufficient phase margin. 2) Determination of the controller gain for the precise control over the phase margin and bandwidth. The first step is very trivial such that zero of the PI controller cancels the pole coming from the envelope model. In other words, Eq.2.3 is needed to be met for pole-zero cancellation.

$$\begin{aligned} \tilde{H}(s) &= \frac{1}{4} \cdot \frac{A}{s+\beta/2} \\ C(s) &= \frac{K_P \cdot s + K_I}{s} \\ \Rightarrow s + \frac{K_I}{K_P} &= s + \frac{\beta}{2} \Rightarrow \frac{K_I}{K_P} = \frac{\beta}{2} \end{aligned} \tag{2.3}$$

After pole-zero cancellation step is performed, open-loop gain of the drive mode system is needed to be adjusted such that bandwidth of the system is maximized with a sufficient phase margin. Phase margin directly affects settling time and over-shoot, therefore optimum phase margin is needed to be targeted in the designs. Drive mode is a 3^{rd} order system after pole-zero cancellation. One order comes from the integrator and two order comes from the low pass filter. In addition, optimum phase margin for the second order systems is between 55° and 60°. In drive-mode designs, same rule of thumb is applied, as well. After analytical design, small adjustments are done according to simulation results. These results show that optimum phase margin occurs between 65° and 70° for our system. At this phase margin, system is near the critically damped case in which settling time is very sensitive to parameter variations. As a result, 60° is targeted for the controller designs for drive modes even if this value is not optimum. In order to have a 60° phase margin, phase contribution of the low pass filter is needed to be 30°. Therefore, taking the phase drop due to integrator into account, over-all phase drop equals to 120° which corresponds to 60° phase margin. Frequency corresponding to 30° phase contribution of the low pass filter is a certain value, since the circuit topology used in drive mode system is fixed. As it will be shown in Chapter 4, multi-feedback type Butterworth filter is used in our drive mode systems. Cut-off frequency of the low pass filter is also fixed at 100Hz for a reasonable rejection of high frequency components which are around 20kHz. Frequency characteristics of this filter are shown in Figure 2.5. As this figure shows, phase of the low pass filter drops $-30°$ at 35Hz. As a result, unity gain frequency should occur at 35Hz for 60° phase margin. Eq. 2.4 shows the second condition for a reasonable phase margin with maximum bandwidth according to these results.

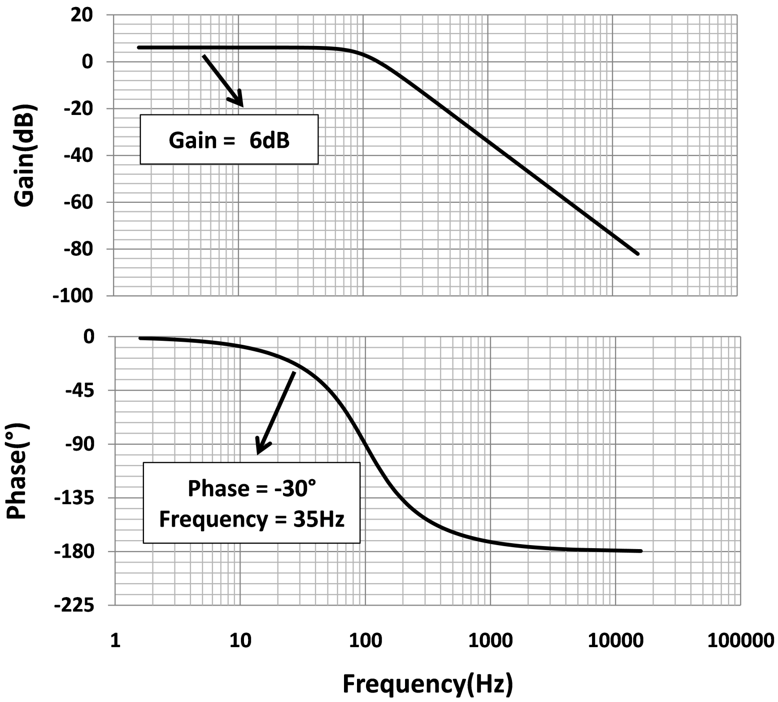

Figure 2.5: Frequency characteristics of the low pass filter used in drive mode system.

$$\begin{aligned} \frac{K_P \cdot s + K_I}{s} \cdot \frac{K_{env}}{s + \beta/2} \cdot F(s) &= 1|_{f=35Hz} \\ \frac{K_{env} \cdot K_P}{2 \cdot \pi \cdot 35} &= 1 \\ K_{env} \cdot K_P &= 220 \end{aligned} \tag{2.4}$$

where,

$$K_{env} = \frac{A}{4} \cdot K_{pre-amp} \cdot K_{mod} \cdot K_{LPF} \cdot K_{dmod} \tag{2.5}$$

$$F(s) : \text{Normalized transfer function of the low-pass filter} \tag{2.6}$$

In the above and below expressions, gain of the low pass filter is expressed in the envelope model constant (K_{env}).

Finally, the drive mode oscillation is needed to be maximized for a better performance. The amount of the deflection is determined by the relation which Eq. 2.7 shows. For a certain process, the gain between the output current of the sensor and displacement is almost con-

Table 2.1: Drive Mode Loop Parameters.

A	Numerator of the mechanical sensor's transfer fucntion
$K_{pre-amp}$	Pre-amplfier gain
K_{mod}	Modulator gain
K_{LPF}	Low Pass Filter Gain
K_{dmod}	Demodulator Gain

stant. In addition, current to voltage conversion gain is fixed with the preamplifier. Besides, reference voltage should be a low noise and low drift signal for better bias instability. For this reason, it is taken from a band-gap reference, so that this voltage is constant, as well. As a result, low pass filter gain is needed to be fixed for a certain value of the drive deflection . Eq. 2.8 shows the value for a desired drive displacement. For the current sensors, the amount of the generated voltage per 1um is 190mV. This amount equals to the multiplication of the gains between displacement-to-current gain in the sensor and current-to-voltage gain of the preamplifier and following gain stage, as Eq. 2.7 shows.

$$X_{drive} \cdot \underbrace{K_{X/C} \cdot K_{C/V}}_{K_{X/V}=190mV} \cdot K_{mod} \cdot K_{LPF} = V_{ref} \tag{2.7}$$

$$K_{LPF} = V_{ref}/X_{drive} \cdot K_{X/C} \cdot K_{C/V} \cdot K_{mod}$$

$$K_{LPF} = \frac{V_{ref}}{X_{drive} \cdot K_{X/V} \cdot K_{mod}} \tag{2.8}$$

Combining Eqs. 2.5, 2.4 and 2.8, Eq. 2.10 can be obtained. Using this relation and the condition for pole zero cancellation, integrator coefficient can be found easily as Eq. 2.10 indicates. These both equations shows the controller values for a desired deflection amount X_d and 60° phase margin. Unity-gain frequency of this system is fixed at 35 Hz which satifies the 60° phase margin.

$$K_P = \frac{f_{unity\,gain} \cdot 2\pi}{K_{env}} = \frac{f_{unity\,gain} \cdot 2\pi}{\frac{A}{4} \cdot K_{pre-amp} \cdot K_{mod} \cdot \frac{V_{ref}}{X_{drive} \cdot K_{X/V} \cdot K_{mod}} \cdot K_{dmod}} \tag{2.9}$$

$$\boxed{\begin{array}{c} K_P = \dfrac{f_{unity\,gain} \cdot 2\pi}{K_{env}} = \dfrac{f_{unity\,gain} \cdot 2\pi}{\dfrac{A}{4} \cdot K_{pre-amp} \cdot \dfrac{V_{ref}}{X_{drive} \cdot K_{X/V}} \cdot K_{dmod}} \\ K_I = K_P \cdot \dfrac{\beta}{2} \end{array}} \tag{2.10}$$

Figure 2.6 shows settling of the system constructed with envelope model. Settling time is 21msec. In addition, complete system is also simulated. Figure 2.7 shows the modulator input signal which gives direct information about the drive velocity. Envelope model carries the characteristics between low pass filter output after demodulator and modulator input. This low pass filter causes a delay between the modulator input and the peak detector output. As a result, some slight discrepancy between the demodulator output and actual envelope output is expected. This fact is shown in Figure 2.7: settling time is 18 msec. Moreover, the regulated signal is the velocity of the drive mode motion, not the displacement. In other words, preamplifier output is the derivative of the actual drive mode displacement. As a result, settling of demodulator input does not show real settling of drive motion. Fortunately, envelopes before and after differentiator are almost same. Envelope characteristics of the differentiator can be found in time or Laplace domain as it will be done in Chapter 4. Time domain analysis of such a simple system is much easier than analysis in Laplace domain. Assuming the bandwidth of the message (envelope) signal is much smaller than the carrier frequency, this signal, which is an input of the differentiator in our case, can be expressed in Eq. 2.11.

$$V_{dif,in} = m(t) \cdot cos(\omega \cdot t) \tag{2.11}$$

Taking the derivative of this equation, Eq. 2.12 is obtained.

$$V_{dif,out} = \frac{V_{dif,in}}{dt} = \dot{m}(t) \cdot cos(\omega_D \cdot t) - m(t)\omega_D \cdot sin(\omega_D \cdot t). \tag{2.12}$$

Second term is much stronger than the first term, since $\dot{m}(t)$ can be maximum $\Omega \cdot m(t)$ where, Ω is the maximum frequency (bandwidth) of the input signal. Therefore, output signal can be expressed in Eq. 2.13.

$$V_{dif,out} = -m(t)\omega_D \cdot sin(\omega_D \cdot t) \tag{2.13}$$

As a result, envelope of the signal after differentiator can be expressed in Eq. 2.14.

$$m_O(t) = m(t) \cdot \omega_D \tag{2.14}$$

In brief, differentiator only behaves as a gain stage for the envelope signals assuming envelope signal bandwidth is much smaller than the drive mode resonance frequency. This condition is mostly valid in gyroscope applications. Simulation results of drive displacement is completely consistent with these results.

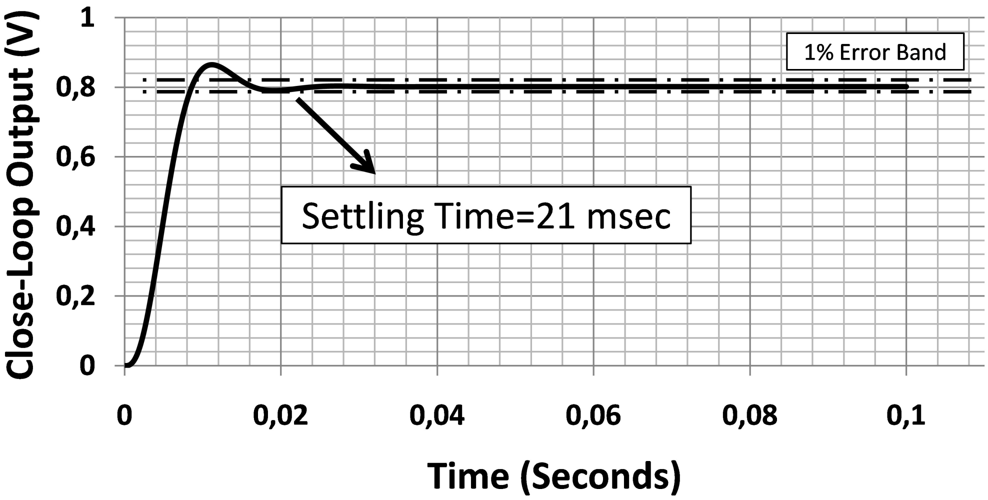

Figure 2.6: Settling of drive mode system constructed with the envelope model.

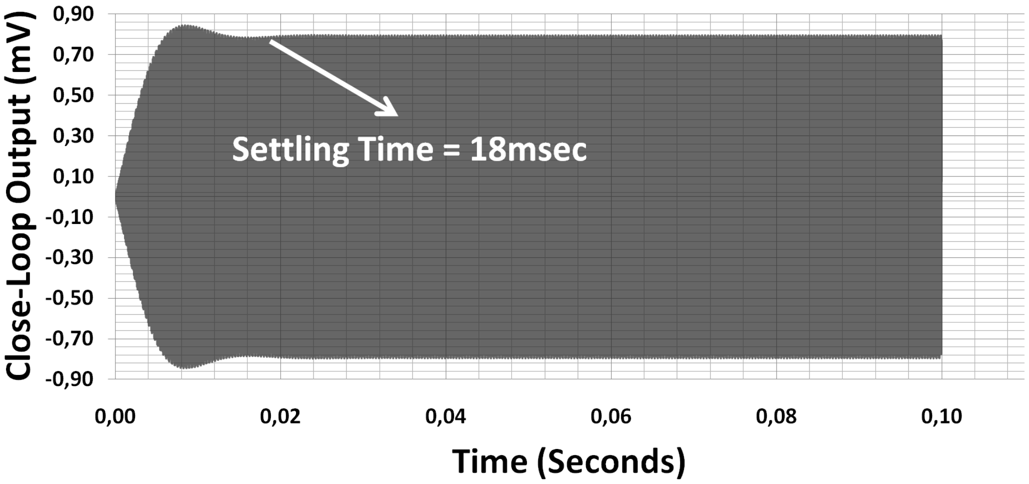

Figure 2.7: Settling of the complete drive mode system.

2.2 Effects of Circuit Imperfections

In the above analysis, effect of the circuit imperfections are not taken into account. Just after the system is powered up, output of the demodulator is around zero and instrumentation amplifier directly gives the reference voltage value to the PI controller input. At these times, capacitor is initially discharged and behaves as a short circuit. Therefore, PI controller is simply an inverting amplifier whose gain equals to proportional controller gain, K_P. In our cases, this value is larger than 10. Consequently, Op-Amp used in PI controller saturates because of this voltage gain and large input signal whose value is 2.048V. Since PI controller output saturates, negative-feedback loop is broken and mechanical sensor operates in open-loop. Furthermore, it is actuated with a very large force which is generated by modulated signal with amplitudes around supply voltages of the Op-Amp used in PI controller. Until negative feedback loop for the amplitude regulation is formed, system dynamics is completely different than the classical system approach in which saturation of the controller is not taken into account, as discussed above.

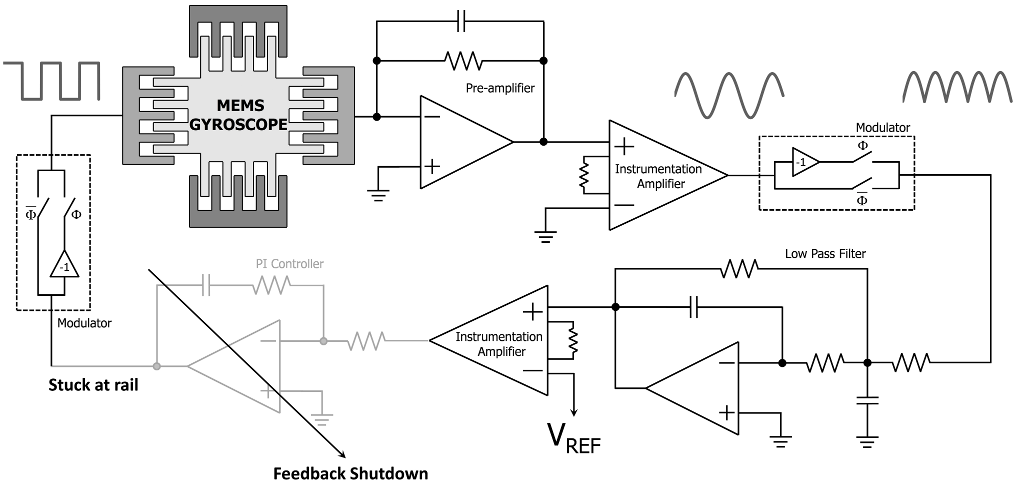

Figure 2.8: Drive mode system with broken feedback due to saturation of Op-Amp in the PI controller.

Figure 2.8 shows the equivalent system until negative feedback loop forms. The instant where Op-Amp cancels saturation and enters linear region is the time when the voltage of the inverting terminal times the proportional gain equals to saturation level of the Op-Amp. After that instant, closed-loop system discussed above starts to operate. As a result, the over-all system is needed to be optimized for the best performance instead of taking the only closed-loop system into account. Open-loop system dynamics shown in the Figure 2.8 is quite different from the closed-loop system. First of all, as it was mentioned above, system is actuated by a constant force which is generated by a square wave having $2.5V_{\text{Peak}}$. This 2.5V is the saturation level of the Op-Amp used in PI controller. Since this voltage is constant, sensor settles to its steady state value in a slowly manner. Nevertheless, the input force is very large, so that the steady state value is very high and the necessary voltage which cancels the Op-Amp from the saturation can be reached in a small portion of the over-all settling process. In the open-loop, output of the low pass filter can be expressed with Eq.2.15.

$$V_{LPF,OUT} = V_{PI,Out} \cdot \tilde{H}(s) \cdot F(s) \tag{2.15}$$

where,

$$\begin{gathered}
\tilde{H}(s) : \text{Envelope Model} = \frac{1}{4} \cdot \frac{K_{Sensor} \cdot K_{Pre-Amp} \cdot K_{Ins-Amp} \cdot \overbrace{K_{Demod}}^{\frac{4}{\pi}} \cdot \overbrace{K_{Mod}}^{\frac{8}{\pi}} \cdot K_{LPF}}{s + \beta/2} \\
F(s) : \text{Normalized Low Pass Filter}
\end{gathered} \tag{2.16}$$

In Eq. 2.15 pole coming from the envelope model is much smaller than the poles of the low pass filter. Therefore, in this analysis low pass filter can be expressed as a single gain stage as shown in Eq. 2.17 where K_{env} is given in Eq. 2.5.

$$V_{LPF,OUT} = V_{PI,Out} \cdot \frac{K_{env}}{s + \beta/2} \tag{2.17}$$

The expression of this equation in time domain is simply an exponential decaying signal whose relation is expressed in Eq. 2.18. Steady state level is much higher than the critical voltage which starts closed-loop operation. Eq. 2.20 expresses this critical voltage which provides the closed-loop operation. As a result of this significant ratio, low pass filter output settles to the critical voltage almost linearly. Figure 2.9 shows this linear settling and Eq. 2.19 expresses its rate. As it was discussed before, the rate of change at the output is very high, though over all settling time exceeds tens of seconds. For the current sensor design [3], speed of the open loop settling can be found as approximately 45mV/msec. Time elapsed until low pass filter output reaches the critical voltage is expressed by Eq. 2.21.

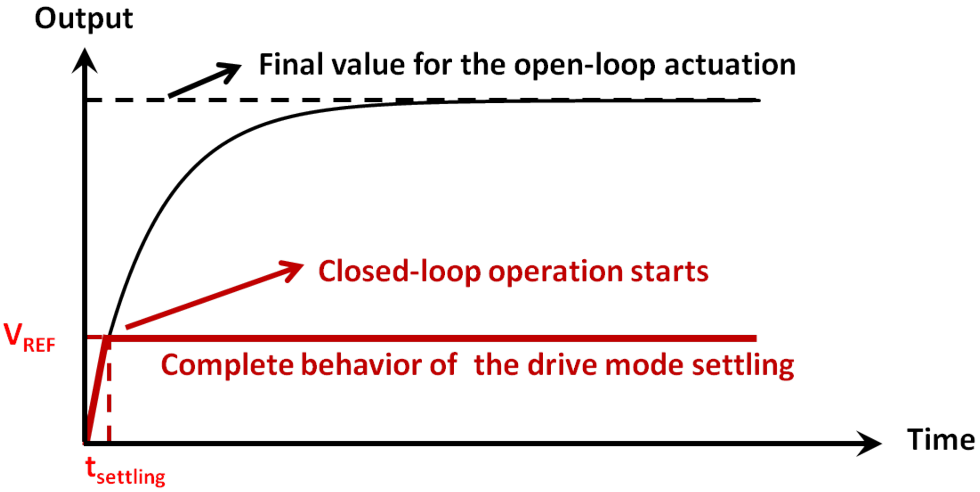

Figure 2.9: Visualization of linear settling of the closed-loop drive mode system for non-ideal case.

$$V_{LPF,OUT} = \overbrace{V_{PI,Out}}^{V_{PI,Supply}} \cdot \overbrace{K_{env} \cdot 2/\beta}^{\text{Steady State Value}} \cdot (1 - e^{-t\cdot\frac{\beta}{2}}) \tag{2.18}$$

$$v_{OL} = \left.\frac{dV_{LPF,OUT}}{dt}\right|_{t\to 0} = V_{PI,Supply} \cdot K_{env} \tag{2.19}$$

$$V_C = V_{ref} - V_{PI,Supply}/K_P \tag{2.20}$$

$$t_{set,OL} = \frac{V_C}{v_{OL}} = \frac{V_{ref} - V_{PI,Supply}/K_P}{V_{PI,Supply} \cdot K_{env}} \tag{2.21}$$

Since we want to minimize the overall settling, we should make optimization for the settling time including the open-loop and the closed-loop dynamics. Settling process of the open-loop system is simple, but the transient dynamics of the closed-loop system is quite complicated. In order to simplify this analysis, dominant pole approximation can be done for the closed loop system. In fact, this assumption makes sense especially for the under-damped system. Closed-loop transfer function can be expressed as Eq. 2.22 shows. In this expression, effect of the low pass filter is not taken into account assuming there is enough phase margin to satisfy the under-damped condition.

$$\begin{aligned} G_{OL}(s) &= \frac{K_{env} \cdot K_P}{s} \\ G_{CL}(s) &= \frac{G_{OL}(s)}{1 + G_{OL}(s)} \\ G_{CL}(s) &= \frac{K_{env} \cdot K_P}{s + K_{env} \cdot K_P} \end{aligned} \tag{2.22}$$

Equation given in Eq.2.22 is defined between the reference terminal of the instrumentation amplifier and output of the low pass filter. Since this system is a single pole system, low pass filter output can easily be expressed with the exponential function as Eq. 2.23 shows.

$$V_{LPF,OUT} = V_f + (V_i - V_f) \cdot e^{-t \cdot K_{env} \cdot K_P}$$

where,
V_i: initial value of the output=V_C
V_f: steady state value of the output=V_{ref}

$$V_{LPF,OUT} = V_{ref} + (V_C - V_{ref}) \cdot e^{-t \cdot K_{env} \cdot K_P} \tag{2.23}$$

Elapsed time between the instant when the low pass filter output reaches the critical voltage and final value for 1 % error band is expressed in Eq. 2.24.

$$\begin{aligned} t_{set,CL} &= ln\left(\frac{V_{ref} - V_C}{V_{ref} - V_{ref} \cdot 0.99}\right) \cdot \frac{1}{K_{env} \cdot K_P} \\ t_{set,CL} &= ln\left(\frac{V_{ref} - V_C}{V_{ref}} \cdot 100\right) \cdot \frac{1}{K_{env} \cdot K_P} \end{aligned} \tag{2.24}$$

where,

$$V_C = V_{ref} - \frac{V_{PI,Supply}}{K_P} \tag{2.25}$$

Combining Eqs. 2.24 and 2.21, overall settling time can be obtained.

$$\begin{aligned} t_{set} &= t_{set,OL} + t_{set,CL} \\ &= \frac{V_C}{V_{PI,Supply} \cdot K_{env}} + ln\left(\frac{V_{ref} - V_C}{V_{ref}} \cdot 100\right) \cdot \frac{1}{K_{env} \cdot K_P} \end{aligned} \tag{2.26}$$

In order to minimize settling time, Eq. 2.26's derivative with respect to the proportional controller parameter can be found as shown in Eq. 2.27.

$$\frac{dt_{set}}{dK_P} = 0$$

$$\frac{1}{K_{env} \cdot K_P^2} - \frac{ln(100 \cdot V_{PI,Supply}/V_{ref})}{K_{env} \cdot K_P^2} + \frac{ln(K_P)}{K_{env} \cdot K_P^2} - \frac{1}{K_{env} \cdot K_P^2} = 0$$

$$\frac{1}{K_{env} \cdot K_P^2} \left(-ln\left(100 \cdot V_{PI,Supply}/V_{ref}\right) + ln(K_P)\right) = 0$$

$$K_{P,1} = 100 \cdot \frac{V_{PI,Supply}}{V_{ref}} \tag{2.27}$$

$$K_{P,2} \rightarrow \infty \tag{2.28}$$

Eq. 2.27 shows that there is one finite solution for the critical point. The slope is negative for K_P smaller than $K_{P,1}$ and positive for K_P larger than $K_{P,1}$. These results show that the critical point is the minimum settling time. Note that, this minimum settling time is very large such that system is unstable. Therefore, we can conclude that proportional controller should be maximized in over-damped case. The maximized proportional controller in dominant-pole approximated system is around 10. In fact, same situation may be available in under-damped case. But, even if it is not true, since critical voltage is almost equal to the reference voltage, settling of the drive-mode system is dominated by the open-loop dynamics as discussed above. In other words, using larger values does not cause significant improvement in the settling time. This is also verified with simulation results. Moreover, there is no over-shoot in the system if the controller value is selected for the over-damped case. Even if this controller is selected for the under-damped case, over-shoot will be very low due to the dominancy of the open-loop dynamics over drive-settling. This new settling time, therefore, can be expressed as it is defined for open-loop dynamics, shown in Eq. 2.24 for which critical voltage almost equals to reference voltage. To conclude, according to this new analysis proportional controller can be selected according to the same procedure as discussed for the closed-loop dynamics. In addition, integrator coefficient should be selected to cancel the pole of the envelope model: Although, settling of the system is dominated by open-loop dynamics, stability of the overall system is characterized by closed-loop dynamics. Besides, settling-time of the closed-loop dynamics is still important if there is a disturbance during the operation. If it is not fast enough, recovery of the system will take a plenty of time which will spoil the complete operation of the gyroscope.

$$\boxed{t_{set} = \text{settling time} \approx \frac{V_{ref}}{V_{PI,Supply} \cdot K_{env}}} \tag{2.29}$$

In the current system implemented with discrete components, reference potential (V_{ref}) is 2.048V, supply potential ($V_{PI,Supply}$) of PI controller is 2.5V and K_{env} is 17.5. Inserting these parameters in Eq. 2.29, settling time is found 47msec. In simulations, 49msec settling time is observed, as Figure 2.10 shows.

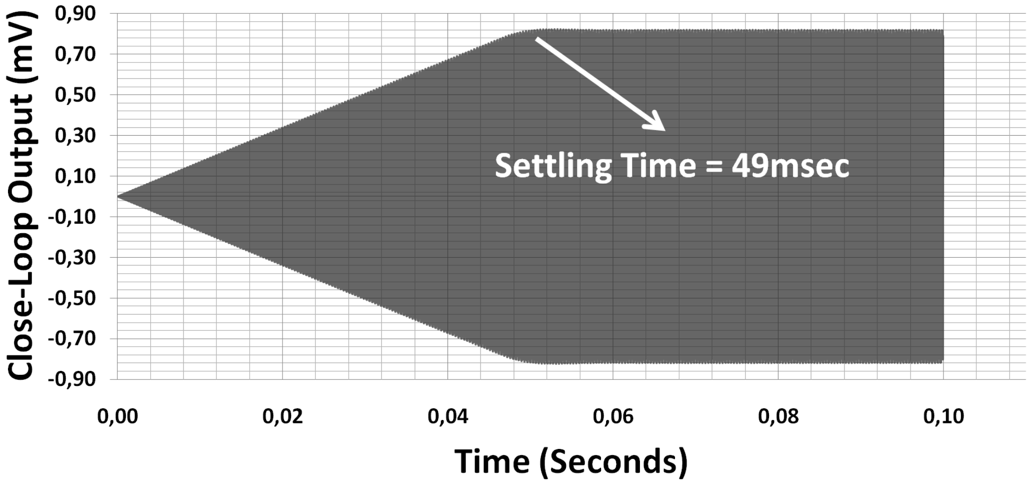

Figure 2.10: Settling of drive mode close-loop system including saturation of Op-Amps.

Settling time of this system is low enough for tactical grade applications. It can be decreased more by increasing the ratio between reference voltage and K_{env} but it decreases the oscillation amplitude in drive mode. As it was emphasized, this oscillation amplitude is the most important parameter in drive mode. As drive mode oscillation amplitude increases, performance of the complete system increases directly. In other words, there is a trade-off between settling time and system performance. This trade-off is expressed in Eq. 2.30.

$$t_{set} \cdot \wp = \kappa \tag{2.30}$$

where, $\wp$: Noise performances (angle random walk and bias instability)

κ: Constant defining the metric for the optimum settling time and noise performances.

Latter constant includes several parameters such supply voltages of PI controller, noise sources in sense system, scale factor, and gyro parameters. This metric expresses that for a given drive system optimum settling time can only be decreased by forfeiting the noise performance of the complete system. Therefore, according to the application needs settling time and noise performances are determined. In our system, settling time is below 50msec for a sufficient amplitude, therefore we do not need to consider this trade-off in details.

Another important issue in the controller design is the repeatability of the controller parameters for different sensors. At the begging of this section, it is mentioned that pole-zero cancellation is needed to be done for a good settling time and phase margin. On the other hand, in order to achieve this cancellation, the ratio between integrator and proportional controller gains should equal to the half of the drive mode system bandwidth. Unfortunately, this bandwidth strictly depends on the vacuum level which varies between sensor to sensor, so controller parameters are needed to be updated. Though pole-zero cancellation provides an advantage in the design procedure, it is not mandatory for a good settling time and phase margin. In controller design, zero of the controller should compensate the phase drop coming from its pole before gain reaches the unity gain frequency. As a result, even if pole-zero cancellation is not performed but above condition is done, same transient performance with same phase margin can be attained. In brief, same controller parameters can be used for different sensors whose bandwidth can vary in a large range.

Usage of the integrator stems from zero steady-state error requirement. On the other hand, in spite of excluding the integrator from the system, steady error is still very low since over-all loop gain is large in order to have a good settling time. If same controller design procedure mentioned above is applied, steady state error is in 0.4% error band. In fact, exclusion of this integrator capacitor will provide some advantageous. If initial value of the integrator capacitance is not zero before the system starts up, transient dynamics mentioned above will change completely. In this context, time constants of the PI controller are quite large so that discharge of the capacitor which can be considered as recovery time, will take a plenty of time. This problem can be visualized as followings: If output of the PI controller is negative, positive feedback path becomes negative feedback path since its polarity changes. Furthermore, because of very large high gain in the positive feedback loop due to the gain of the comparator in the modulator, system becomes instable and locks to an electrical oscillation. Even in this electrical oscillation, output of the peak detector circuitry gives positive signal since it only detects the amplitude of a modulating wave. Therefore, instrumentation amplifier output gives negative voltage, because in this state amplitude of electrical oscillation is lower than the reference voltage and reference voltage is connected to inverting terminal of the instrumentation amplifier. Negative voltage output of an instrumentation amplifier discharges the capacitor in the PI controller because of inverting amplifier characteristics of this controller. This discharge provides recovery of the system and enables it to lock into mechanical resonance frequency. Unfortunately, this recovery time is large owing to the fact that resistors and capacitor of the controller are very large. Maximum discharge current is around 10uA for a typical system. As a result, recovery of this system can take hundreds of millisecond for a 1μF PI capacitor. If this PI capacitor is removed from the system, such a start-up problem will be solved.

2.3 Modified Drive Mode Controller Circuit

In drive controller, regulation of the drive oscillation is important for a robust scale factor and good bias instability. On the other hand, drive mode system includes several block operating at DC frequencies. Since these blocks are operating at DC frequencies, they are susceptible to offsets, their drifts and Flicker (1/f) noise. To put it differently, though system is insensitive to drifts of the sensor, it is sensitive to circuit drifts and noises. High performance Op-Amps and instrumentation amplifier solve this problem in a substantial amount but their implementation in CMOS is quite difficult. For CMOS implementation, a new drive controller system is proposed in this thesis. Figure 2.11 shows this system. This controller does not have a strong regulation over the drive oscillation as the previous one performs. On the other hand, it provides a simple, low noise solution and it is insensitive to offset drifts. In theory, settling time of this system can be very low with no over-shoot. In addition, this transient performance is same in a very wide range of quality factor. In practice, this fact is limited by the gain bandwidth product of the Op-Amps used in the systems. In contrast with the low offset and 1/f noise Op-Amp design in CMOS, high-speed Op-Amp design is quite straight forward which only conflicts with the current.

Operation of this circuit is simple comparing to the conventional drive controller system. Positive feedback loop provides self-oscillation. Output of the preamplifier is fed back to the sensor and it is mixed with the output of the positive feedback path. This path forms the negative feedback which regulates the drive oscillation amplitude. Actuating signal is nothing but

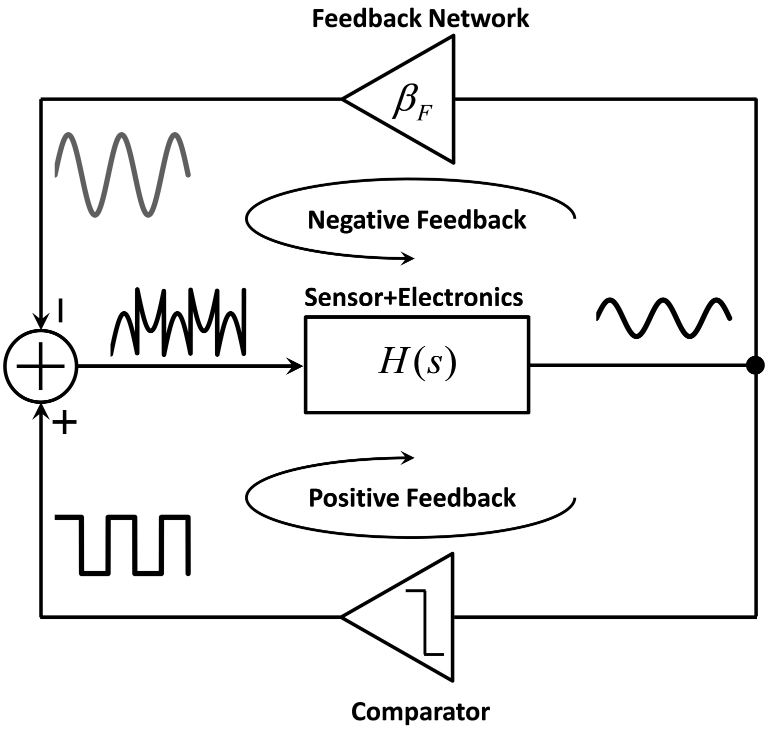

Figure 2.11: Simplified block diagram of the modified drive controller.

their difference which can be considered as an error signal. If loop gain of the negative feedback is high enough, error signal is very low such that output of the negative feedback follows the first harmonic of the positive feedback output. Accordingly, drive deflection is regulated, because the relation between the drive oscillation amplitude and negative feedback output is only a gain. Strength of the oscillation amplitude regulation strictly depends on the loop gain, since system behaves as a simple proportional controller. In order to provide this loop gain, feedback gain factor β can be increased. Nonetheless, the amount of the drive-oscillation amplitude decreases with increasing loop gain which reduces noise performance of the system. This problem can be tackled with putting a gain stage behind the sensor instead of using large feedback factor. This is a good solution but error signal is the difference between square wave and sinusoidal wave which are in phase. The resultant wave, which is shown in Figure 2.11, has very large edges even the first harmonic is very low. The peak of this signal equals to the supply level of the comparator used in the positive feedback loop. Therefore, putting a gain stage before the sensor is not possible, otherwise waveform spoils which will reduce the first harmonic. In other words, oscillation amplitude decreases. Fortunately, increase in the loop gain is larger than the reduction of the first harmonic for small gains before the sensor, and the overall loop gain can be increased by inserting this small gain stage preceding the gyroscope. This improvement is around 2 and it cannot be improved further.

To improve system performance, output of the positive feedback should have slower transition around zero crossings as in sinusoidal wave and triangular waveforms. Thus, error signal peak is consistent with its first harmonic; peak value is low. In this configuration, a gain stage before the sensor can be used. But, these will complicate the system, especially for pure sinusoidal output of the feedback case. Triangular waveform can be generated easily using simple digital blocks and integrator, but the error between the peak of the triangular wave and its first harmonic equals 20% percentage of triangular waveform peak. As a consequence, maximum gain before the sensor is around 5.

In addition to the regulation strength, the settling time also directly depends on the loop gain. Eq. 2.39 and same limitations are valid for it but for a reasonable drive oscillation, settling time can be kept below 100 msec which is sufficient in most of the applications. Correspondingly, same loop gain can suppress the drifts of the sensor in 99 %: if gain of the sensor decreases to half of its initial, drive deflection changes in an amount of 2%. Furthermore, the drift of the drive deflection does not directly affect the output. Only a portion of it will cause drift at the output and this portion is directly proportional to the quadrature amount. If system is quadrature free, then drive deflection will not cause any drift in the system. Current systems in our research has quadrature cancellation loop which provides this condition [3]. On the other hand, drive oscillation regulation is not necessary only for a good bias instability but it is also necessary for a robust scale factor: Scale factor is desired to be insensitive to parameter variations of different sensor such as quality factor and ambient conditions such as temperature. But regulation mentioned above will be enough in most conditions. In fact, considering this drive loop's offset and Flicker noise free operation, this system is better in terms of scale factor repeatability than the conventional system implemented in CMOS. Mathematical description of this system is simpler than the conventional drive loop's. Envelope model of the sensor can also be used but it is not necessary for this system, because all the amplitude control operation is performed in high frequency region, not in base-band. First of all, closed loop gain be described as Eq. 2.33.

$$G_{CL}(s) = \frac{H(s)}{1 + H(s) \cdot \beta_F} \tag{2.31}$$

where, β_F: Feedback factor

$$A(s) = \frac{\overbrace{K_{Sensor} \cdot K_{Pre-Amp} \cdot K_{Ins-Amp}}^{\text{Forward Gain: } K_{FG}} \cdot s}{s^2 + \beta s + \omega_D^2} \tag{2.32}$$

$$G_{CL}(s) = \frac{K_{FG} \cdot s}{s^2 + (\beta + K_{FG} \cdot \beta_F \cdot)s + \omega_D^2} \tag{2.33}$$

$$\tag{2.34}$$

In resonance frequency, the gain of the closed-loop system is expressed in 2.35. Using Taylor's series, steady state error percentage can be found as Eq. 2.38 expresses.

$$G|_{f=f_D} = \frac{K_{FG}}{\beta + K_{FG} \cdot \beta_F} \tag{2.35}$$

$$= \frac{1}{\beta_F} \cdot \frac{1}{1 + \frac{\beta}{K_{FG} \cdot \beta_F}} \tag{2.36}$$

$$\approx \frac{1}{\beta_F} \cdot (1 - \frac{\beta}{K_{FG} \cdot \beta_F}) \tag{2.37}$$

$$e_{SS,\%} = \frac{\beta}{K_{FG} \cdot \beta_F} \cdot 100 \tag{2.38}$$

Amount of this error describes the strength of the regulation. It mainly depends on feedback factor and forward gain. Especially, if this system is high-Q than system has almost perfect amplitude regulation. In current works, quality factor larger than 100.000 is observed for wafer-level vacuumed gyroscopes. For such levels, bandwidth of the system is 0.12 Hz which corresponds to β =1 rad/sec. Typical value for forward gain, K_{GF} is around ten. As a result, if feedback factor is around 10, steady state error can be below 1% error as it was mentioned above.

Closed-loop system is also a second order system whose envelope behavior can be expressed with Eq. 2.2. As a result, this system settles to its steady state value in an exponential manner. This is described in Eq. 2.39 for 1% error band.

$$t_{set} = 4.5 \cdot \tau = 4.5 \cdot \frac{2}{\beta + K_{FG} \cdot \beta_F} \approx \frac{9}{K_{FG} \cdot \beta_F} \tag{2.39}$$

This equation shows that if the feedback and forward gain factors are 10, settling time is around 90 msec which is a good value in most of the applications. Figure 2.12 shows the simulation results of the settling of the new generation drive mode controller. In addition, this amount can further be improved with increasing loop gain. Only limitation is the speed of the Op-Amps used in the system. This can be increased to 100MHz with a reasonable power consumption for folded-cascode Op-Amps. Another limitation for this system is the maximum drive oscillation amplitude: It decreases with increasing feedback factor. Likewise, conventional drive controller has similar restriction which is expressed in Eq. 2.30. For current design for this new drive system, κ is lower than conventional loop's κ. But it can be further be increased by putting a gain stage before the sensor and changing the output waveform of the positive feedback which will complicate the over all system.

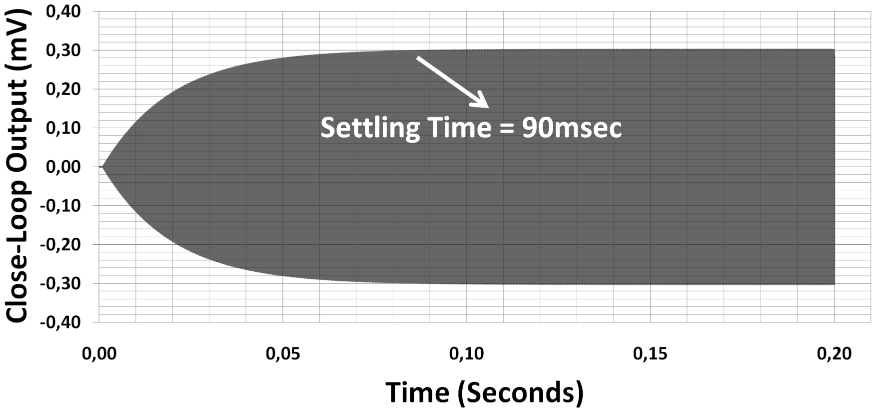

Figure 2.12: Settling of the new generation drive mode controller.

2.4 Summary

The drive mode transient performance is optimized with the pole-zero cancellation technique, but transient performance is mainly limited by the circuit imperfections coming from the saturation of electronics. Fortunately, it is derived that optimum solution for an ideal system also gives the best solution for non-ideal case. Finally, a new drive controller is introduced. This system has a very simple architecture, but the trade-off between the transient performance and maximum drive oscillation amplitude is worse than the trade-off in the conventional drive mode controller.

CHAPTER 3

SENSE MODE MODELING AND ANALOG FORCE FEEDBACK CONTROLLER DESIGN

In a MEMS gyroscope the open-loop systems have a sensitive and low noise operation, but the linearity is a major problem for high ranges above a 100°/sec. Besides, the responsivity of the system directly depends on the sensor parameters which are likely to vary with ambient and time. These changes in the system operation worsen the repeatability of the sensor without calibration. Finally, the speed of the overall system is out of control in open loop operation. Especially the systems, working at matched mode and mismatched mode in which the amount of mode separation is not high enough, speed is a significant restriction. Closed-loop operation solves the above problems in a considerable amount. On the other hand, system complexity and design procedure harden for a robust system. In literature there are basically two kinds of closed-loop sense mode systems: analog force feedback and digital force feedback. Analog force feedback simplifies the systems. Nevertheless, because of signal processing task is carried out in analog domain, the system is sensitive to environmental noise and design is not flexible. For different sensors, the hardware is needed to be changed. On the other hand, systems relying on the digital force feedback are complex but they are less sensitive to environment and design of the controller is flexible. It can be re-programmed via software. This chapter, firstly in literature, presents a comprehensive study on analog force feedback. Section 3.1 explains the base-band equivalent model of sense dynamics. Section 3.2 gives a design procedure with PID controller. Section 3.3 explains the integrator based controller design and its restrictions. Finally, Section 3.4 summarizes this chapter.

3.1 Base-Band Equivalent Model of Sense Dynamics

In gyroscopes, rate information is at the amplitude of the Coriolis force. As a result, before processing the rate data and feeding back to the sensor, demodulation is needed. Unfortunately, the system dynamics are changed owing to this operation. Demodulation changes the overall frequency response by its inherent frequency up/down conversion at sense output. Therefore, it is not easy to follow a straightforward sense controller design procedure. On the other hand, it is possible to develop a system mimicking the envelope behavior of the Coriolis force. In fact, envelope model for drive-mode dynamics is available which is discussed in details in Chapter 2. But, such a simple model for sense mode operating at mismatched conditions is not available in literature.

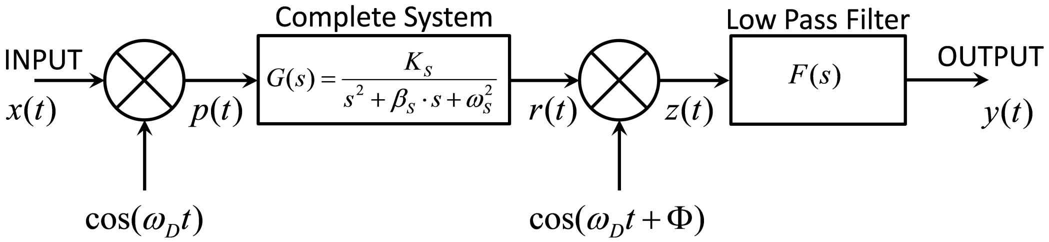

Figure 3.1: Generic configuration of open-loop sense system.

A generic open loop sense mode of MEMS gyroscope can be shown as in Figure 3.1. Modulator in this system is not an electronic modulator; it can be considered as a mechanical one. Rate signal is mixing with the drive oscillation which constitutes Coriolis force and sense mass moves according to this force. Because of the fact that Coriolis force is proportional to the velocity of drive motion, carrier of this mechanical modulator can be considered as a signal which leads the drive oscillation: there is a 90° phase difference between drive oscillation. By the same token, quadrature signal is also an input for the system shown in Figure 3.1. Here, only difference is the phase of the mechanical modulator carrier which is in phase with drive mode oscillation. These both forces produces motion in sense mode and this motion is converted to current by the sensor, then voltage by the preamplifiers. This signal is a modulated signal whose carrier is drive oscillation and it is composed of two out phase signals. In order to obtain rate information, phase sensitive demodulation must be carried out instead of using peak detector whose carrier equals to its input as in drive mode system. In addition, carrier of the demodulator should be in-phase with the Coriolis component to obtain rate information. The phase of this signal can be found easily by applying a DC rate to the input. Phase contribution of the sensor changes whether it operates under matched condition or mismatched condition. If system operates under matched condition, sensor gives in-phase current to the preamplifier. Since capacitive preamplifier is used in sense mode for low noise operation, output of the preamplifier will have 90° phase difference between Coriolis force. So, resultant signal is out-phase with velocity of Drive mode oscillation. Since, drive mode system preamplifier output is in phase with drive mode oscillation velocity, true carrier for matched mode can be obtained by using a 90° phase shifter between drive preamplifier output and demodulator carrier. In a similar way, for mismatched operation, the carrier of demodulator in sense mode must be in-phase with drive preamplifier output. Since extra mode-matching loop is needed to operate the sensor in matched-mode, control of sense mode is carried out in mismatched condition.

Input and output of this system are in base-band but system between modulator and demodulator is operating at carrier frequency. As a result, it is not possible to use this direct model to express the relation between input and output. In addition, drive mode envelope model is not valid for a generic sense system, since this model is derived for a second order modulated system which is operating at its resonance frequency. It will be shown later that new derived sense model converges to this drive model for matched condition, as well.

Derivation procedure can be performed in time domain or Laplace domain. Latter is easier than former one. Eq. 3.1 shows the expression for Laplace transformation.

$$\int_0^{\infty} e^{-s \cdot t} \cdot g(t) \cdot dt \tag{3.1}$$

Relation between modulated signal, $p(t)$ and input signal, $x(t)$ is shown in Eq.3.2. Eq. 3.3 shows Laplace transform of this equation. This equation is obtained using shifting property of Laplace transformation. The resultant signal is The Coriolis Force which makes the sense mass move.

$$p(t) = x(t) \cdot cos(\omega_D t) = x(t) \cdot \frac{e^{j\omega_D t} + e^{-j\omega_D t}}{2} \tag{3.2}$$

$$P(s) = X(s) * \frac{\delta(s + j\omega_D) + \delta(s - j\omega_D)}{2} = \frac{X(s + j\omega_D) + X(s - j\omega_D)}{2} \tag{3.3}$$

Output of this system equals to the multiplication of the input signal and transfer function of the sense mode of gyroscope.

$$R(s) = P(s) \cdot G(s) = \frac{X(s + j\omega_D) + X(s - j\omega_D)}{2} \cdot G(s) \tag{3.4}$$

Relation between demodulator output and gyroscope output is same as Eq. 3.3.

$$Z(s) = \frac{R(s + j\omega_D) + R(s - j\omega_D)}{2} \tag{3.5}$$

$$Z(s) = \frac{X(s + 2j\omega_D) + X(s)}{4} \cdot G(s + j\omega_D) + \frac{X(s) + X(s - 2j\omega_D)}{4} \cdot G(s - j\omega_D) \tag{3.6}$$

Demodulator output includes high frequency terms at two times of the drive mode resonance frequency. These terms come from both input signal, rate and gyro sense mode transfer function. Since, the input signal is band-limited, which is expected to be lower than hundreds of 100 Hz, its expected power around two times of drive resonance frequency is almost negligible. Furthermore, in the closed-loop operation feedback does not allow to produce these high frequency signals because of band-limiting blocks used in the loop. Due the fact that high frequency components in Eq. 3.6 ($X(s \pm 2j\omega_D)$) are cascaded with the low pass filter, only a portion of these high frequency terms smaller than the cut-off frequency of the low pass filter can pass through the filter. Since, input and feedback signals are band-limited, $X(s \pm 2j\omega_D)$ has a negligible power in the band of the low pass filter. To put it differently, this part has no effect at the output and it can be ignored. Therefore, this system is simplified to Eq. 3.7.

$$\begin{aligned}
Y(s) &= Z(s) \cdot F(s) \\
&= X(s) \cdot \frac{G(s + j\omega_D) + G(s - j\omega_D)}{4} \\
&\quad \underbrace{+ \left(\frac{X(s + 2j\omega_D)}{2} \cdot G(s + j\omega_D) + \frac{X(s - 2j\omega_D)}{4} \cdot G(s - j\omega_D) \right)}_{\text{Filtered out by the Low Pass Filter for band-limited input}} \cdot F(s) \\
&\cong X(s) \cdot \frac{G(s + j\omega_D) + G(s - j\omega_D)}{4}
\end{aligned} \tag{3.7}$$

The sense mode dynamics for capacitive preamplifier can be expressed in Eq. 3.8.

$$G(s) = \frac{K_S}{s^2 + \dfrac{\omega_S}{Q_S} \cdot s + \omega_S^2} \tag{3.8}$$

where,

$$K_S = \underbrace{\frac{\partial C_{S,act}}{\partial x} \cdot V_{PM}}_{\alpha_{V/F}} \cdot \underbrace{\frac{\partial C_{S,sense}}{\partial x} \cdot V_{PM}}_{\alpha_{x/I}} \cdot \underbrace{\frac{1}{C_{Pre-amp}}}_{\alpha_{I/V}} \cdot \frac{1}{m_S}$$

In the above equation, $\alpha_{V/F}$, $\alpha_{x/I}$, and $\alpha_{I/V}$ are not the gains for different conversion processes, but they are the scalar appearing in these processes. Eq. 3.8 can be expanded as Eq. 3.9 shows.

$$G(s) = \frac{K_S}{2j\omega_S\sqrt{1-1/4Q_S^2}}\left(\frac{1}{s+\dfrac{\omega_S}{2\cdot Q_S}-j\omega_S\sqrt{1-1/4Q_S^2}} - \frac{1}{s+\dfrac{\omega_S}{2\cdot Q_S}+j\omega_S\sqrt{1-1/4Q_S^2}}\right) \tag{3.9}$$

Inserting Eq. 3.9 into Eq. 3.7, Eq. Eq. 3.10 is obtained.

$$\begin{aligned}Y(s) = X(s)\cdot F(s)\cdot \frac{K_S}{8j\omega_S\sqrt{1-\dfrac{1}{4Q_S^2}}}\Bigg(&\frac{1}{s+\dfrac{\omega_S}{2\cdot Q_S}-j\omega_S\sqrt{1-1/4Q_S^2}+j\omega_D}\\ &+\frac{1}{s+\dfrac{\omega_S}{2\cdot Q_S}-j\omega_S\sqrt{1-1/4Q_S^2}-j\omega_D}-\frac{1}{s+\dfrac{\omega_S}{2\cdot Q_S}+j\omega_S\sqrt{1-1/4Q_S^2}+j\omega_D}\\ &-\frac{1}{s+\dfrac{\omega_S}{2\cdot Q_S}+j\omega_S\sqrt{1-1/4Q_S^2}-j\omega_D}\Bigg)\end{aligned} \tag{3.10}$$

Combining the conjugate terms, Eq. 3.10 takes the following form.

$$\begin{aligned}Y(s) = X(s)\cdot F(s)\cdot \frac{K_S}{8j\omega_S\sqrt{1-\dfrac{1}{4Q_S^2}}}\Bigg(&\frac{2j\left(\omega_S\sqrt{1-\dfrac{1}{4Q_S^2}}+\omega_D\right)}{s^2+\dfrac{\omega_S}{Q_S}\cdot s+\underbrace{\left(\dfrac{\omega_S}{4Q_S}\right)^2+\left(\omega_S\sqrt{1-\dfrac{1}{4Q_S^2}}+w_D\right)^2}_{\omega_H^2}}\\ &+\frac{2j\left(\omega_S\sqrt{1-\dfrac{1}{4Q_S^2}}-\omega_D\right)}{s^2+\dfrac{\omega_S}{Q_S}\cdot s+\underbrace{\left(\dfrac{\omega_S}{4Q_S}\right)^2+\left(\omega_S\sqrt{1-\dfrac{1}{4Q_S^2}}-w_D\right)^2}_{\omega_L^2}}\Bigg)\end{aligned} \tag{3.11}$$

This equation also shows two resonator system: one of them has a resonance frequency around ω_H and other has a resonance frequency around ω_L. Second term, whose resonance frequency is around ω_L, is rejected by the low pass filter. Thus, over-all system is expressed by Eq.3.12.

$$Y(s) = X(s) \cdot F(s) \cdot \frac{K_S}{4} \cdot \frac{1 - \dfrac{\omega_D}{\omega_S \sqrt{1 - 1/(4Q_S)^2}}}{s^2 + \underbrace{\dfrac{\omega_S}{Q_S}}_{\beta_S} \cdot s + \omega_L^2} \tag{3.12}$$

Moreover the gyroscope is operating at high vacuum levels. This fact allows us to neglect $1/4Q_S^2$ expressions but for matched mode this assumption fails because this term becomes comparable with frequency terms. For better approximation, it is better to use Taylor's series approximation.

$$\frac{1}{\sqrt{1-x}} \cong 1 + \frac{x}{2} \Rightarrow \frac{1}{\sqrt{1 - \dfrac{1}{4Q_S^2}}} \cong 1 + \frac{1}{8Q_S^2} \tag{3.13}$$

Combining Eqs. 3.12 and 3.13, Eq. 3.14 can be obtained.

$$Y(s) = X(s) \cdot F(s) \cdot \frac{K_S}{4} \cdot \frac{1 - \dfrac{\omega_D}{\omega_S} - \dfrac{\omega_D}{\omega_S} \cdot \dfrac{1}{8Q_S^2}}{s^2 + \beta_S \cdot s + \omega_L^2} \tag{3.14}$$

ω_L can be simplified for high vacuum levels as following equation shows.

$$\omega_L \cong \left(\frac{\omega_S}{2Q_S}\right)^2 + (\Delta\omega)^2$$

where,

$$\Delta\omega = \omega_S - \omega_D$$

In Eq. 3.14, there is a strict relation between input, $X(s)$ and output, $Y(s)$. This relation can directly be used in system analysis. In fact, it is *base-band equivalent model* of a sense mode of MEMS gyroscope whose demodulator carrier is in-phase with drive mode preamplifier output. This model can also be considered as an envelope model and it is denoted by $G_{env}(s)$.

$$G_{env}(s) = F(s) \cdot \frac{K_S}{4} \cdot \frac{1 - \dfrac{\omega_D}{\omega_S} - \dfrac{\omega_D}{\omega_S} \cdot \dfrac{1}{8Q_S^2}}{s^2 + \beta_S \cdot s + \omega_L^2} \tag{3.15}$$

If system is operating at matched conditions, then above system can be expressed with Eq. 3.16.

$$G_{env}(s) = -F(s) \cdot \frac{K_S}{32Q_S^2} \cdot \frac{1}{\left(s + \dfrac{\beta_S}{2}\right)^2} \tag{3.16}$$

This result shows that if system mismatch amount is low, then response of this system is inversely proportional to the square root of the drive/sense mode resonance frequency. For this reason, for mode-matched system demodulator carrier must have 90° phase difference between drive deflection.

For mis-matched operation, 3.15 converges to simple relation shown in Eq. 3.17.

$$\boxed{G_{env}(s) = F(s) \cdot \frac{K_S}{4 \cdot \omega_S} \cdot \frac{\Delta\omega}{s^2 + \beta_S + (\Delta\omega)^2}} \tag{3.17}$$

This base-band equivalent model is valid for a sense mode operating at mismatched condition and having a sufficiently large quality factor.

Table 3.1 shows envelope models for four possible sense system shown in Figure 3.1. Envelope model changes with the type of the preamplifier and relative phase difference between mechanical modulator and electronic demodulator carriers, Φ. These types are capacitive interface and in-phase carriers, capacitive interface and out-of phase carriers, resistive interface and in-phase carriers and finally resistive interface and out-of phase carriers. Derivation for the first case has been performed above and other's derivations are available in the Appendix. Transfer function for trans-resistive preamplifier is also given in Eq. 3.18. Step responses of these four systems are shown in Figure 3.2. In these figures, both complete systems and their envelope model simulations are performed.

$$G(s) = \frac{K_S \cdot s}{s^2 + \beta_S \cdot s + \omega_S^2} \tag{3.18}$$

Table 3.1: Envelope models of the sense mode of a MEMS gyroscope for the different preamplifiers and demodulator carriers.

	Resistive Preamplifier	Capacitive Preamplifier
$\Phi = 0°$	$\frac{K_S \cdot F(s)}{4} \cdot \frac{s + \frac{\omega_S}{2 \cdot Q_S}}{s^2 + \beta_S \cdot s + \omega_L^2}$	$\frac{K_S \cdot F(s)}{4\omega_S} \cdot \frac{\Delta\omega - \frac{\omega_D}{8Q_S^2}}{s^2 + \beta_S \cdot s + \omega_L^2}$
$\Phi = 90°$	$\frac{K_S \cdot F(s)}{4} \cdot \frac{\frac{s}{2 \cdot Q_S} + \Delta\omega + \frac{\omega_D}{8Q_S^2}}{s^2 + \beta_S \cdot s + \omega_L^2}$	$-\frac{K_S \cdot F(s)}{4\omega_S} \cdot \frac{s + \frac{\omega_S}{2 \cdot Q_S}}{s^2 + \beta_S \cdot s + \omega_L^2}$

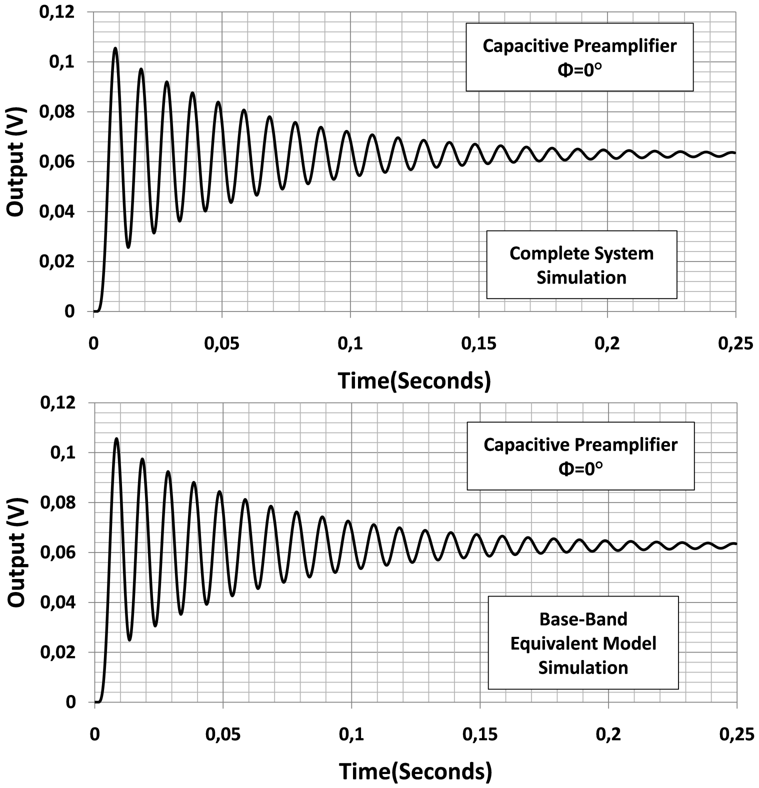

(a) Capacitive preamplifier and $\Phi = 0°$.

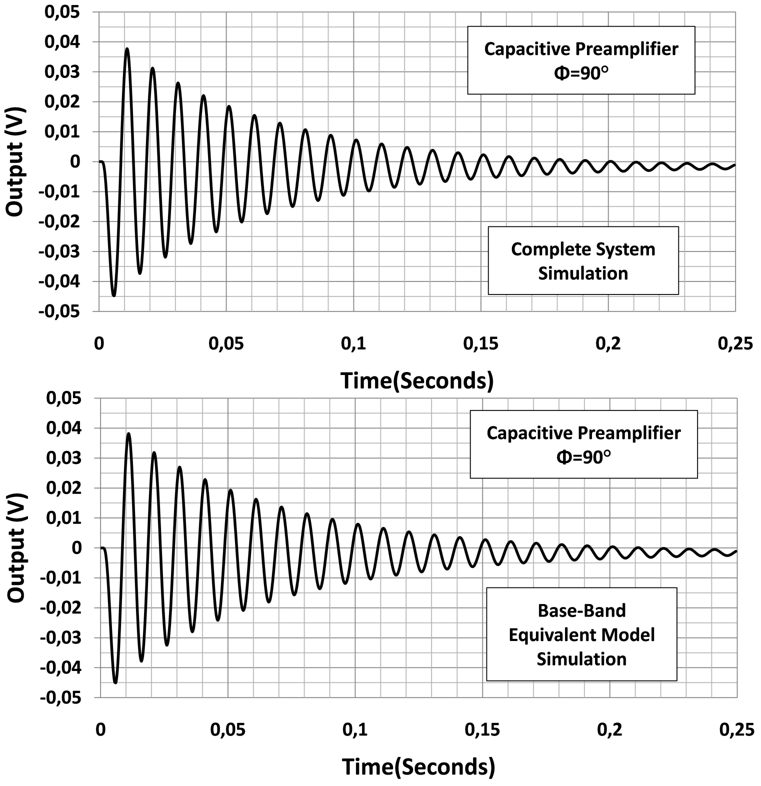

(b) Capacitive preamplifier and $\Phi = 90°$.

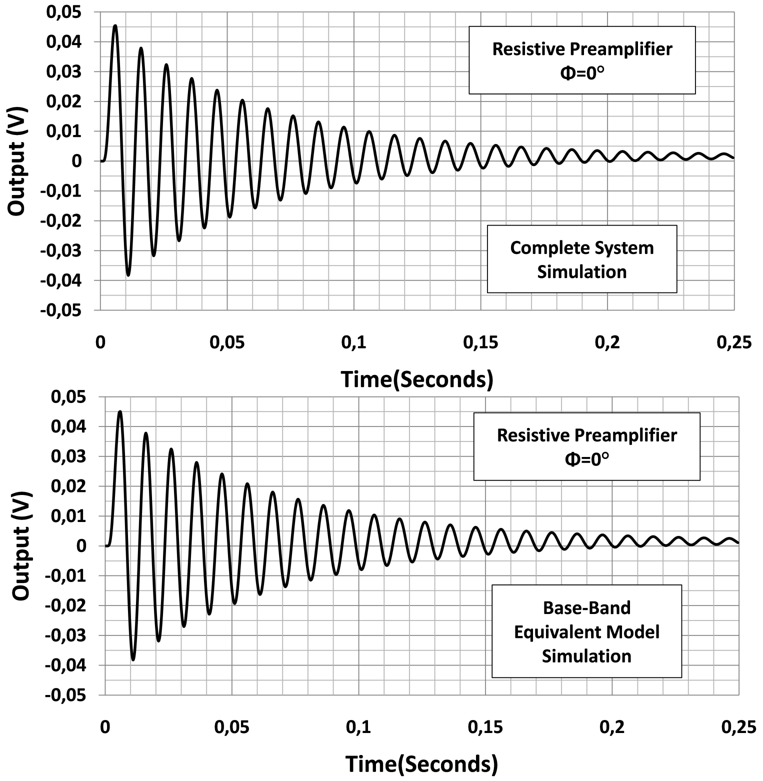

(c) Resistive preamplifier and Φ = 0°.

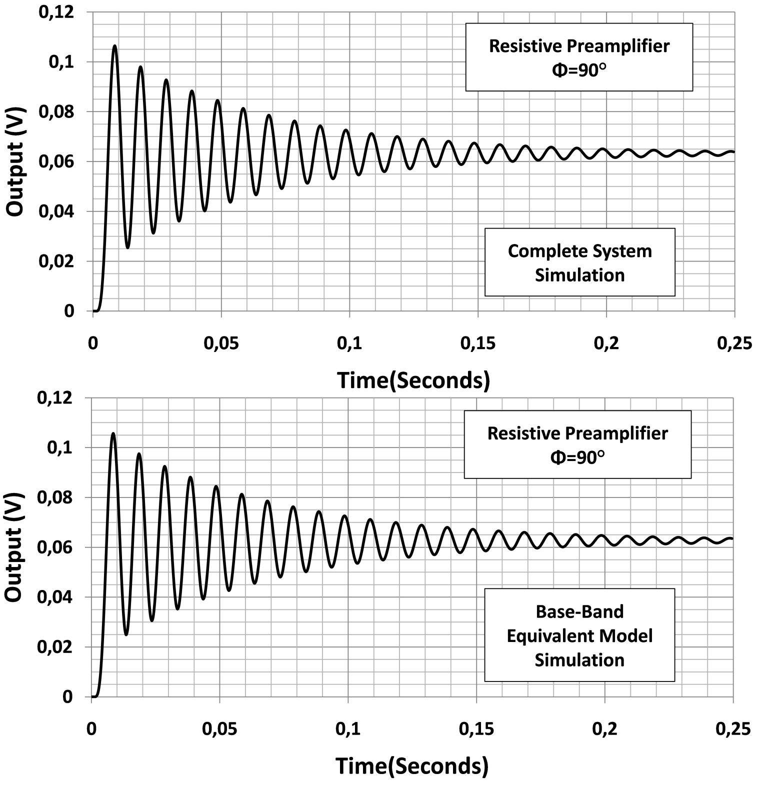

(d) Resistive preamplifier and Φ = 90°.

Figure 3.2: Open-loop simulation results for complete system and proposed base-band equivalent models.

where,

$$\omega_L^2 = \left(\frac{\omega_S}{2Q_S}\right)^2 + (\Delta\omega)^2$$
$$\Delta\omega = \omega_S - \omega_D$$
$$\beta_S = \frac{\omega_S}{Q_S}.$$

Open-loop simulation parameters for the system, shown in Figure 3.1, are given in Table 3.2. In this table, $K_{S,C}$ is the numerator of sense mode transfer function with capacitive preamplifier and $K_{S,R}$ is the numerator for resistive type preamplifier. Simulation results show that base-band equivalent models are completely consistent with complete system simulation. These models can also be verified for other mismatch amount. Since, characteristics of the proposed base-band models are same as the actual system characteristics, these models can safely be used in analyzing envelope performance of gyro system and designing controllers. These models provide several advantages: 1) Proposed models are LTI systems which enable to use strong design methods developed for LTI systems. 2) System become much more simple relieving analyze and design procedure. 3) New system is operating at base-band. On the other hand, original system works in around drive resonance frequency. Time step of the simulation must be low enough to characterize the system sufficiently but it took a plenty of time comparing with simulation periods of base-band models.

Table 3.2: Open-loop simulation parameters.

ω_S	$10.1kHz \cdot 2\pi$
ω_D	$10kHz \cdot 2\pi$
β_S	$5Hz \cdot 2\pi$
$K_{S,C}$	10^7
$K_{S,R}$	$\frac{10^7}{\omega_D} = 160$
$\omega_{LPF,-3dB}$	$100Hz \cdot 2\pi$

In Table 3.1, there are only two assumptions: 1) Quality factor is high enough such that Eq. 3.19 holds. 2) Mismatch amount is much smaller than the resonance frequencies of drive and sense modes. This condition is necessary to neglect resonator of the base-band equivalent model with higher resonance frequency as shown in Eq. 3.10. This condition also simplifies some of the base-band equivalent models more as it is shown in Appendix. Eq. 3.20 shows mathematical description of this assumption.

$$\frac{1}{4Q_S^2} \ll 1 \tag{3.19}$$

$$\Delta\omega \ll \omega_S + \omega_D \tag{3.20}$$

This table also gives important information about what the correct phase is for different applications. Correct phase can be found by investigating the gain of the base-band equivalent model for s=0. If it is very low such that its responsivity is inversely proportional to the quality factor, system should be operated for the other phase. To illustrate, either capacitive preamplifier with 0° phase or resistive preamplifier with 90° phase can be used for mismatch operation.

Similarly, if rate sensing is desired to be performed at matched condition, then other cases should be selected. Similar analysis can be done for quadrature detection. On the other hand, in that case since modulator carrier is itself lags the drive preamplifier output with 90°, transfer functions given in the table are valid for the other phase. To illustrate, for quadrature detection, mismatch sense system with capacitive preamplifier should have a carrier lagging the drive preamplifier output in 90°.

Using the results of Table 3.1, it is possible to obtain both base-band equivalent models for matched and mismatched operation. For matched operation, $\Delta\omega$ becomes zero and Table Table 3.1 simplifies to Table 3.3. In this table, resistive preamplifier with 0° phase is same as the envelope model used in drive mode. In fact, these conditions are same as the ones using in drive amplitude control system. In addition, similar envelope model is seen for capacitive preamplifier type with 90° phase. This model is useful in sense system, if mode-matching is done. Other models have very low gains which are not functional in any loop.

Since, complicated mode matching control loop is required for mode-matched operation, work in this thesis focus on systems operating at mismatched conditions. Therefore, Table 3.1 can be simplified as Table 3.4 shows.

In the above tables, there is a significant similarity between the cases which differ in preamplifier type and demodulator phase. Only difference comes from gain and polarity. The difference between gains stem from the current to voltage conversion process of the different preamplifier types. Voltage to current conversion gain for capacitive type trans-impedance

Table 3.3: Envelope models of the sense mode of a MEMS gyroscope for the matched operation.

	Resistive Preamplifier	Capacitive Preamplifier
$\Phi = 0°$	$\frac{K_S \cdot F(s)}{4} \cdot \frac{1}{s + \frac{\beta_S}{2}}$	$-\frac{K_S \cdot F(s)}{32Q_S^2} \cdot \frac{1}{\left(s + \frac{\beta_S}{2}\right)^2}$
$\Phi = 90°$	$\frac{K_S \cdot F(s)}{32Q_S^2} \cdot \frac{\omega_D}{\left(s + \frac{\beta_S}{2}\right)^2}$	$-\frac{K_S \cdot F(s)}{4\omega_S} \cdot \frac{1}{s + \frac{\beta_S}{2}}$

Table 3.4: Envelope models of the sense mode of a MEMS gyroscope for the mis-matched operation.

	Resistive Preamplifier	Capacitive Preamplifier
$\Phi = 0°$	$\frac{K_S \cdot F(s)}{4} \cdot \frac{s + \frac{\omega_S}{2 \cdot Q_S}}{s^2 + \beta_S \cdot s + (\Delta\omega)^2}$	$\frac{K_S \cdot F(s)}{4\omega_S} \cdot \frac{\Delta\omega}{s^2 + \beta_S \cdot s + (\Delta\omega)^2}$
$\Phi = 90°$	$\frac{K_S \cdot F(s)}{4} \cdot \frac{\Delta\omega}{s^2 + \beta_S \cdot s + (\Delta\omega)^2}$	$-\frac{K_S \cdot F(s)}{4\omega_S} \cdot \frac{s + \frac{\omega_S}{2 \cdot Q_S}}{s^2 + \beta_S \cdot s + (\Delta\omega)^2}$

amplifiers, is inversely proportional to operation frequency since impedance of the capacitor equals to $1/(j\omega)$. On the other hand, gain of the resistive type preamplifier does not depend on frequency. The scalar, K_S for both cases does not include any frequency term. For this reason, frequency parameter of the current-to-voltage conversion process appears in the envelope model. Therefore, constants in these tables can be interpreted as multiplication of the numerator for the sense mode, electronics gains and scaling coming from modulation-demodulation. Last term is due to the multiplication of two sinusoidal signals. There are two mixing operation resulting in scaling with 0.25. This fact is shown in Eq. 3.2.

$$G_{env}(s) = \underbrace{\overbrace{\frac{K_{Sense} \cdot K_{Electronics}}{4}}^{K_G} \cdot E(s)}_{\tilde{G}(s)} \cdot F(s) \tag{3.21}$$

where,

K_{Sense}: Numerator of sense mode of MEMS Gyroscope

$K_{Electronics}$: Electronic Gain between sensor and modulator

$E(s)$: Base-band equivalent model core

$F(s)$: Low Pass Filter.

$\tilde{G}(s)$: Envelope model excluding low pass filter.

Table 3.4 show all possible base-band equivalent model cores. Models marked with † can be used in gyroscope systems. Gains of other models are very low, so they cannot take role in any gyroscope control loops.

Table 3.5: Envelope model cores.

Operation	Φ	Resistive Preamplifier	Capacitive Preamplifier
Matched	0°	$\frac{1}{s+\frac{\beta_S}{2}}\dagger$	$-\frac{\omega_S}{32Q_S^2\cdot\left(s+\frac{\beta_S}{2}\right)^2}$
	90°	$\frac{\omega_S}{32Q_S^2\cdot\left(s+\frac{\beta_S}{2}\right)^2}$	$-\frac{1}{s+\frac{\beta_S}{2}}\dagger$
Mis-matched	0°	$\frac{s+\frac{\omega_S}{2\cdot Q_S}}{s^2+\beta_S\cdot s+(\Delta\omega)^2}$	$\frac{\Delta\omega}{s^2+\beta_S\cdot s+(\Delta\omega)^2}\dagger$
	90°	$\frac{\Delta\omega}{s^2+\beta_S\cdot s+(\Delta\omega)^2}\dagger$	$-\frac{s+\frac{\omega_S}{2\cdot Q_S}}{s^2+\beta_S\cdot s+(\Delta\omega)^2}$

Using Table 3.5 and Eq. 3.2 any system in vibratory MEMS gyroscope can be transformed to base-band easily. As it was mentioned before, because of the additional control loop requirement of mode-matched operation, force-feedback loop is implemented for mis-matched operations. In addition, capacitive type trans-impedance amplifier is used in sense electronics because of its lower noise performance comparing with trans-resistance amplifier. Therefore, in preceding works only the base-band equivalent model, which Figure 3.3 shows, will be used in controller design.

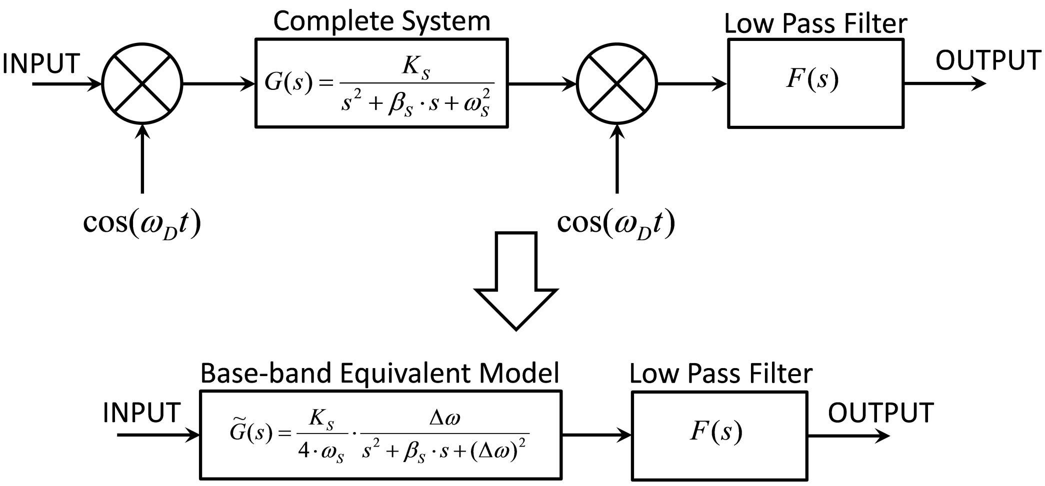

Figure 3.3: Base-band equivalent model of sense mode for capacitive type preamplifier and mis-matched operation.

3.2 Controller Design-Type I

Idea behind sense control is almost same as in the drive mode controller design. Figure 3.4 shows system level, and Figure 3.5 shows the circuit level descriptions of the sense mode controller. First of all, rate information is needed to be extracted by means of phase sensitive demodulation. After the envelope of the sense motion is obtained, resultant signal is sent to a controller. Aim of this controller is to regulate the motion of the sense mode such that sense mass does not move. To conduct this task, controller applies an actuating voltage generating electrostatic force. This force re-balances the Coriolis force to stabilize the sense mass. As it was mentioned at the beginning of this chapter, this enhances overall linearity. The reason for the non-linearity is the non-linear relation between the force and displacement for varying gap type capacitive fingers. On the other hand, using such a controller sense displacement in response to the Coriolis force is eliminated.

The strength of the improvement in the linearity strictly depends on the amount of the error signal. The significance of this signal is much more comparing to the error signal in drive mode. Therefore, sense mode controller should include an integrator to completely remove errors signal. In other words, use of an integrator based controller completely ensures that very good linearity values.

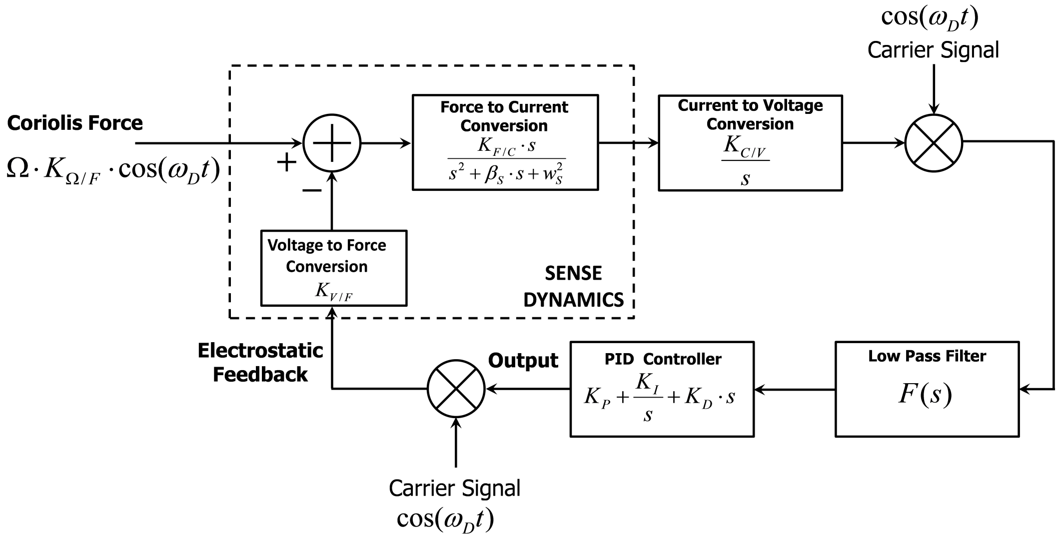

Figure 3.4: Simplified close-loop sense mode system.

In addition, bandwidth of the sense system is another significant parameter in a typical application. Especially, bandwidth of a gyroscope should be at least 100Hz for tactical grade gyroscopes. On the other hand, mismatch amount should be minimized as possible to reduce to contribution of electronics noise at the output as it will be shown in Chapter 4. Both of these tasks conflicts with each other. Over all bandwidth of the system can be extended using more gain in the controller but this will reduce the phase margin. Phase of the open-loop system is mainly contributed by three items. 1) Use of integrator based controller cause 90° phase drop. 2) Low pass filter contributes phase drop. 3) Envelope model shows that system behaves as a resonator with $f_S - f_D$ resonance frequency. There is a sudden phase drop around this frequency. Phase contribution of the sense system dynamics (its envelope characteristics) becomes especially important, if mismatch amount is low. Correspondingly, maximum gain is restricted by the phase contribution of the sense mode envelope model. Fortunately, this phase drop can be compensated using PID (proportional-integral-gain) controller such that numerator of this system cancels the denominator of the envelope model. As a result, sense dynamics will behave as a simple gain stage since its poles are canceled. This will completely simplify the system and now sense loop characteristics completely converge to the loop characteristics of drive mode.

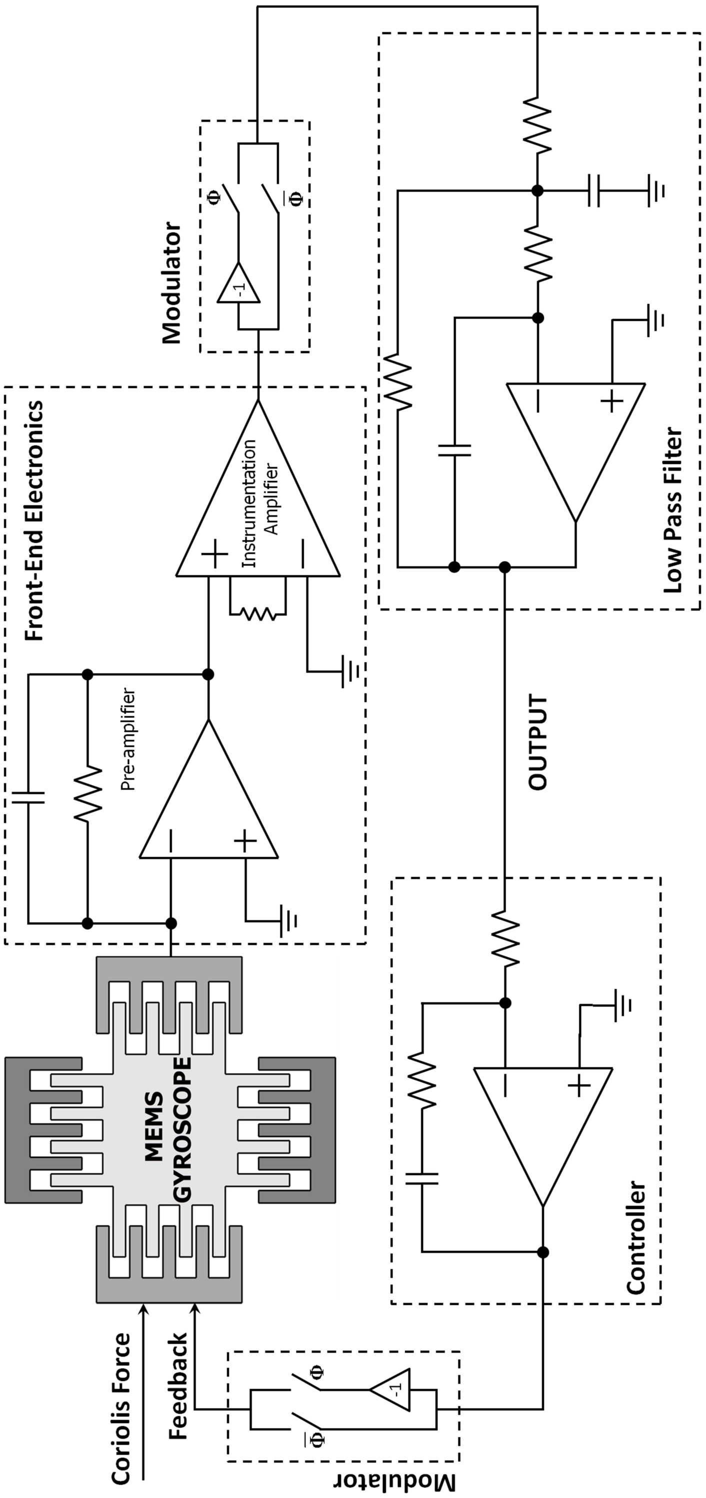

Figure 3.5: Simplified circuit level diagram of the sense mode system.

Controller design procedure is almost same as the design procedure in drive mode controller: 1) Determine the ratio between PID parameters to cancel to sense mode base-band equivalent model poles. 2) Determine the optimum phase margin for the best bandwidth. 3) Determine the derivative gain, K_P, of the controller to satisfy the phase margin found in the second step. 4) Find other controller parameters, K_P and K_I according to the ratios found in the first step.

First step can be performed by equalizing the poles of the base-band equivalent model of sense dynamics and zeros of a PID controller. Eq. 3.22 shows the mathematics of this step.

$$\begin{aligned}
C(s) &= K_D \cdot s + K_P + \frac{K_I}{s} \\
C(s) &= \frac{K_D \cdot s^2 + K_P \cdot s + K_I}{s} \\
\tilde{G}(s) &= \frac{K_G \cdot \Delta\omega}{s^2 + \beta_S \cdot s + (\Delta\omega)^2} \\
s^2 + \beta_S \cdot s + \omega_S^2 &= K_D \cdot s^2 + K_P \cdot s + K_I \qquad (3.22)
\end{aligned}$$

K_G in the base-band equivalent model is a scalar which is shown in Eq. . Eqs. 3.23 and 3.23 indicate the relations between controller parameters:

$$\frac{K_P}{K_D} = \beta_S \quad \frac{K_I}{K_D} = (\Delta\omega)^2 \qquad (3.23)$$

$$(3.24)$$

In the second step, safe phase margin should be at least 45°. For the system including a MFB (multi-feedback) single ended Buttorworth low pass filter having 100Hz cutoff frequency, optimum phase margin in terms of the best bandwidth is also obtained around 45° phase margin with 90Hz bandwidth. On the other hand, settling time of the sense system should also be investigated since this settling time will affect over all start-up time. It is observed that this amount is around 25 msec for 45° phase margin and 22 msec for 60° phase margin. In fact, it can be improved further up to nearly 10 msec but system becomes very susceptible to variations in controller and system parameters. Accordingly, 45° phase margin seems the best solution considering both bandwidth and settling time.

In order to obtain this settling time, overall loop gain must be equal to unity at the frequency where overall phase of open-loop system drops to $-135°$. Since $-90°$ out of $-135°$ comes from the controller pole (at 0), frequency where the phase contribution of the low pass filter is −45° must be the unity-gain frequency. This frequency almost equals to 50Hz. Eq. 3.25 shows the mathematical relations for unity-gain frequency.

$$
\begin{gathered}
|S_{OL}|_{s=j\cdot 2\pi\cdot f_{unity\,gain}} = \left|\tilde{G}(s)\cdot K_{mod}\cdot K_{dmod}\cdot F(s)\cdot C(s)\right|_{s=j\cdot 2\pi\cdot f_{unity\,gain}} = 1 \\
\left|\frac{K_G\cdot\Delta\omega}{s^2+\beta_S\cdot s+\Delta\omega_S{}^2}\cdot K_{mod}\cdot K_{dmod}\cdot F(s)\cdot K_D\cdot\frac{s^2+\frac{K_P}{K_D}\cdot s+\frac{K_I}{K_D}}{s}\right|_{s=j\cdot 2\pi\cdot f_{unity\,gain}} = 1
\end{gathered}
\tag{3.25}
$$

Low pass filter's gain is for 50Hz equals to its DC gain. In addition, denominator of the envelope model is canceled by the zeros of the controller. Therefore, Eq. 3.25 simplifies to Eq. 3.26.

$$
\frac{K_G\cdot\Delta\omega\cdot K_{mod}\cdot K_{dmod}\cdot K_{LPF}\cdot K_D}{2\pi\cdot f_{unity\,gain}} = 1 \tag{3.26}
$$

Therefore, derivative controller can be found using Eq. 3.27.

$$
K_D = \frac{2\cdot\pi\cdot f_{unity\,gain}}{K_G\cdot\Delta\omega\cdot K_{mod}\cdot K_{dmod}\cdot K_{LPF}} \tag{3.27}
$$

Combining Eqs. 3.27 with the result of Eq. 3.23 and Eq. 3.23, Eqs. 3.28 are obtained.

$$
\boxed{\begin{gathered}
K_D = \frac{2\cdot\pi\cdot f_{unity\,gain}}{K_G\cdot\Delta\omega\cdot K_{mod}\cdot K_{dmod}\cdot K_{LPF}} \\
K_P = \beta_S\cdot K_D \\
K_I = (\Delta\omega)^2\cdot K_D
\end{gathered}} \tag{3.28}
$$

These equations give controller parameters for PID controller providing 85 Hz bandwidth, 25 msec settling time with 45° phase margin.

Figure 3.6 shows the open-loop bode plot of the system for the designed controller as Eqs. 3.28 indicates. Parameters of the gyroscope sense system is given in Table 3.6. Owing to the fact that modulators and demodulators used in sense controllers are switching modulators, they can be considered as multiplication block with square wave. Sensor and system rejects higher harmonics, so only the first harmonic of the square wave will be under interest. In addition, demodulator itself has a gain of 2. Similarly, sensor is actuating with differential electrodes which is fed by two modulators whose output are inverse of each other. In other words, modulation process has also 2 extra gains as in demodulation.

Table 3.6: Gyroscope sense system parameters.

Sensor Module Parameters		
K_S	Sense Mode Constant	10^8
ω_S	Sense mode resonance frequency	$13.783kHz \cdot 2\pi$
ω_D	Drive mode resonance frequency	$13.683kHz \cdot 2\pi$
β_S	Bandwidth of the sense dynamics	30 rad/sec
System Parameters		
K_G	Envelope model Constant $= \frac{K_S}{4\omega_S}$	290
$\Delta\omega$	Mismatch amount	$100Hz \cdot 2\pi$
K_{demod}	Demodulator Gain	$4/pi \cdot 2$
K_{LPF}	Low pass filter gain Gain	6.5
K_{mod}	Modulator Gain	$4/pi \cdot 2$

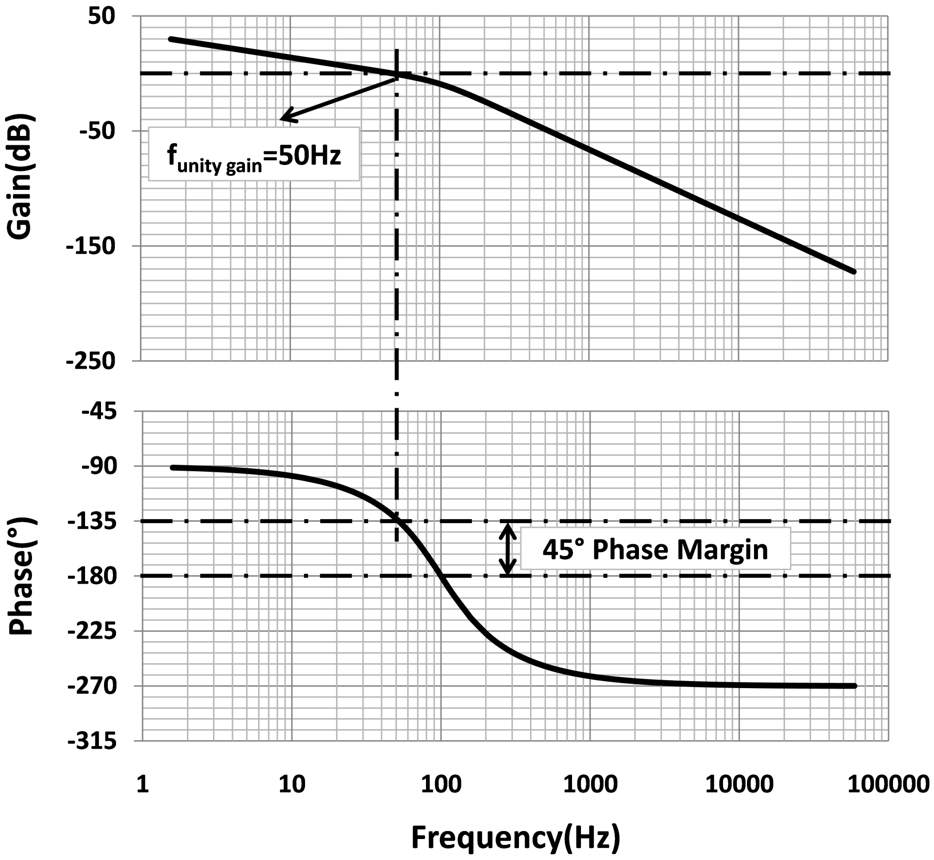

Figure 3.6: Open-loop bode plot of sense system.

Close-loop bode plot of this system is shown in Figure 3.7. It shows that bandwidth of the system is around 85 Hz which is a good value for most of the tactical grade applications. In fact, this bandwidth can easily be improved by increasing the cut-off frequency of the low pass filter. This action, on the other hand, deteriorates suppression of high harmonics of demodulator at the output. Moreover, there is a small peak around 65 Hz. This peak comes from the under-damped characteristics of the system which is designed for 45° phase margin. Step response of this system is also shown in Figure 3.8. This figure shows that settling time is around 25 msec.

These results are also verified with complete system simulations in Simulink. Figure 3.9 shows the gyroscope output as the frequency of the input varies linearly with time. Since this system is not a LTI system, conventional tools for analyzing LTI systems cannot be used such as Bode plots and step response. In order to obtain frequency characteristics, a chirp signal is applied to the input of this complete system. Its frequency changes with time, so that it is possible to observe the frequency characteristics of such a non-LTI system.

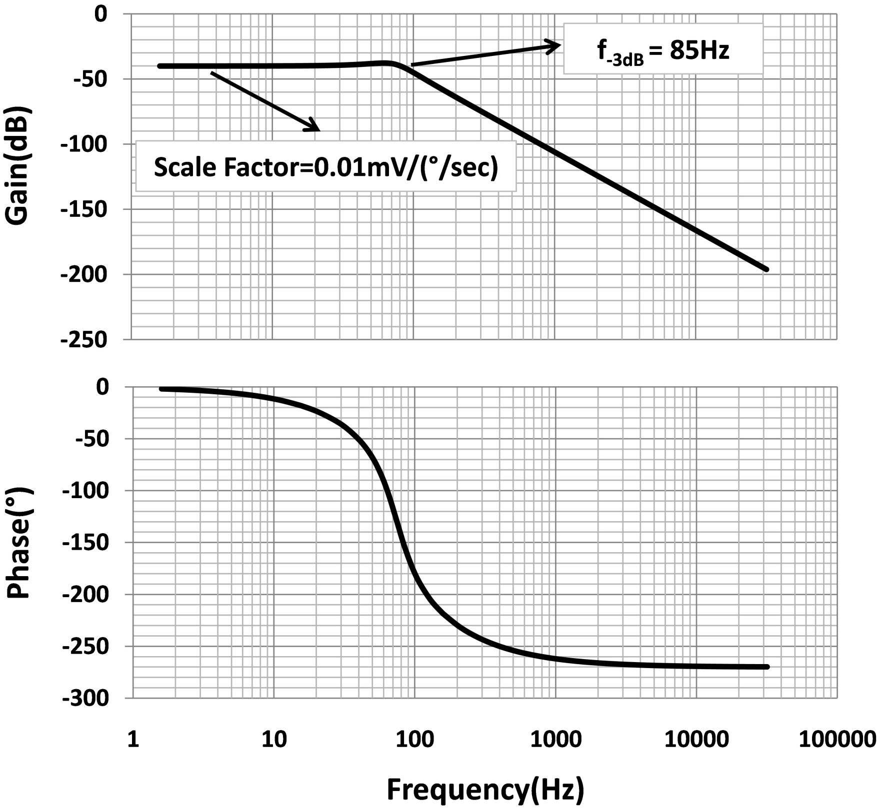

Figure 3.7: Close-loop bode plot of sense system.

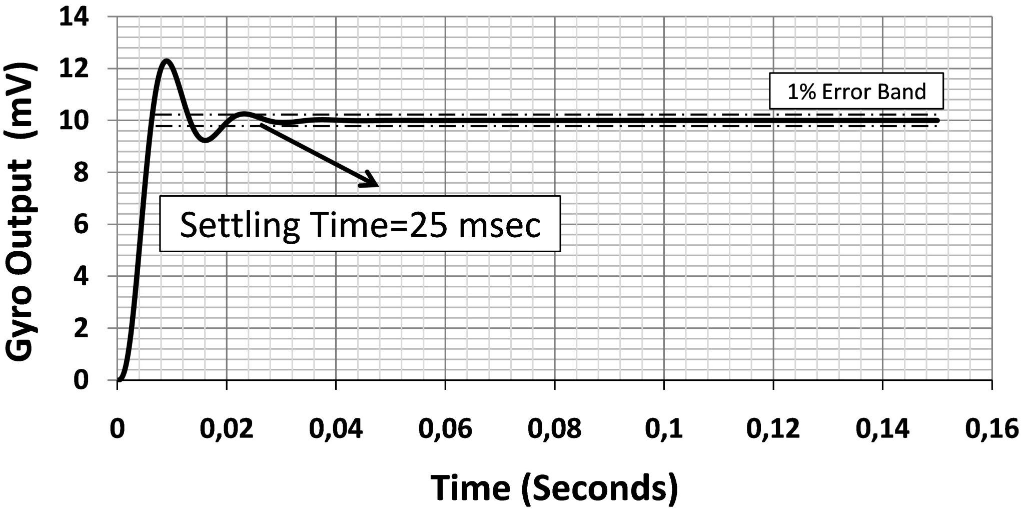

Figure 3.8: Step response of simplified sense system.

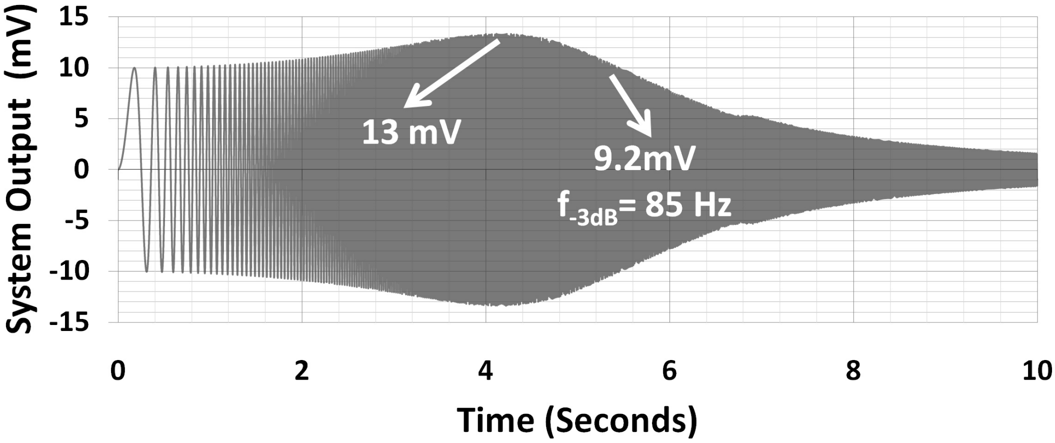

Figure 3.9: Step response of complete sysem.

Figure 3.10 shows step response of the complete system. These simulation results are completely consistent with the ones using LTI blocks including proposed envelope model. Figure 3.11 also shows the modulator input which is output of the instrumentation amplifier after the preamplifier. This signal directly gives information about sense motion. There is a significant displacement before system reaches its steady state. But amount of this signal is not critical, because output which carries information settles in a short period of time.

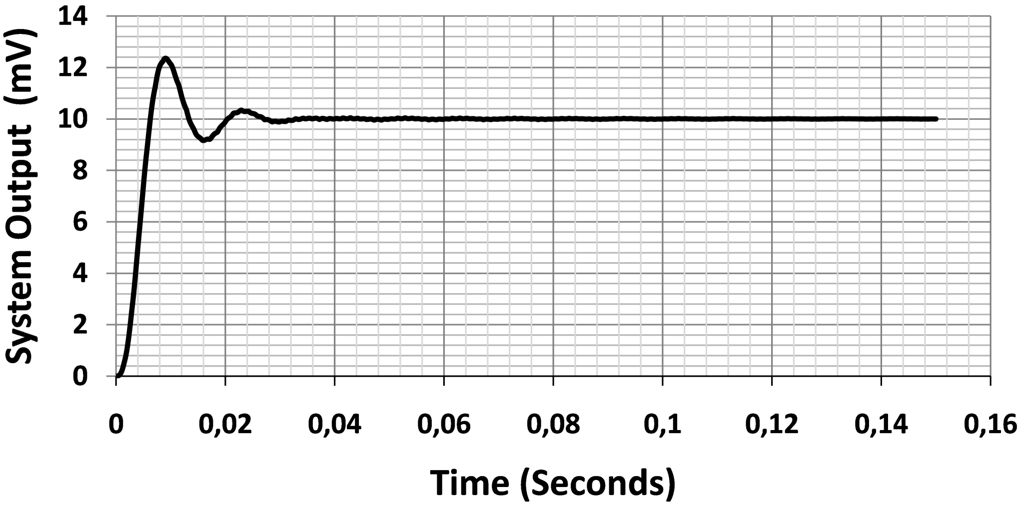

Figure 3.10: Frequency characteristics of the complete sysem.

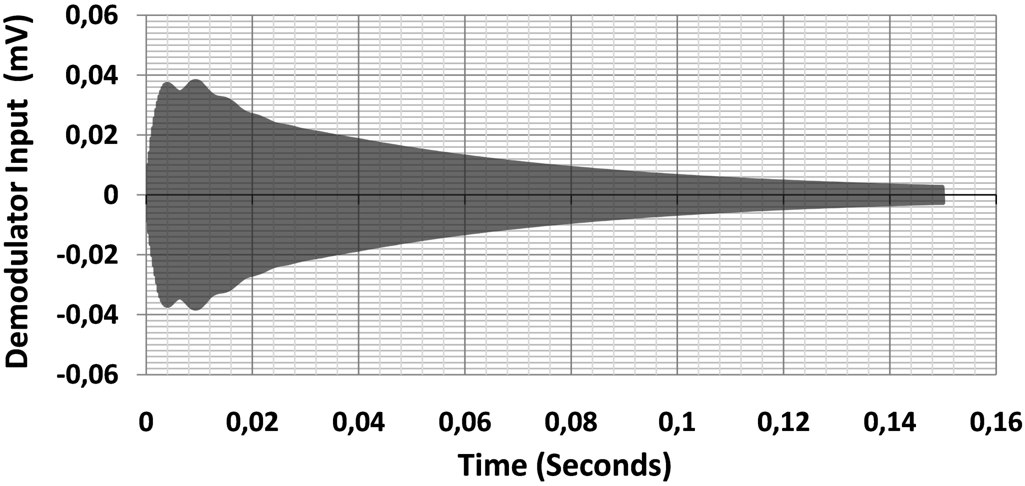

Figure 3.11: Signal regarding sense motion at the start-up.

3.3 Controller Design-Type II

If mismatch amount is high comparing to the desired bandwidth of the system, then contribution of the envelope model can be ignored since it will be very low in the open loop.

In other words, envelope model only behaves as a simple gain stage which does not require phase compensation using PID controller. In fact, pure integrator ($C(s) = K_I/s$) is enough for such a system which has only phase drops due to the integrator and low pass filter in the band of interest. Gain of the system can either be found by evaluating the sense mode transfer function at drive oscillation frequency or evaluating the envelope model at $s = 0$. Eq. 3.29 expresses this gain. Since frequency dependency of sense base-band behavior disappears for high mismatches, above controller design procedure and its implementation simplify. There is an only integrator gain parameter in the controller whose gain expression is given in Eq. 3.30 for 45° phase margin and low pass filter with 100 Hz cut-off frequency.

$$\begin{aligned} K_{SGain} &= \tilde{G}(s)\Big|_{s=0} = \frac{K_G \cdot \Delta\omega}{(\Delta\omega)^2} \\ K_I &= \frac{2 \cdot \pi \cdot f_{unity\,gain}}{K_{SGain} \cdot K_{mod} \cdot K_{dmod} \cdot K_{LPF}} \end{aligned} \tag{3.29}$$

$$\boxed{K_I = \frac{2 \cdot \pi \cdot f_{unity\,gain} \cdot \Delta\omega}{K_G \cdot K_{mod} \cdot K_{dmod} \cdot K_{LPF}}} \tag{3.30}$$

Although low mismatched operation is required for better noise performance, sensitivity of the mismatch amount with respect to the proof mass voltages is very large. Correspondingly, mismatch amount below 200 Hz is not used in current control loops. For this reason, pure integrator is used in our current designs instead of using PID controllers. This will also simplify the implementation of the controller: integrator can be implemented with a single Op-Amp but PID controllers need 4 Op-Amps as it is shown in Chapter 4.

Second controller design approach does not take the phase contribution of the envelope model into account: sensor dynamics are modeled with a simple gain stage. To be able to take the sensor dynamics as a simple gain stage, it is needed to guarantee that the gain and phase responses of the envelope model are almost flat. In other words, envelope model should behave as a simple gain stage in the desired bandwidth in open-loop configuration. Phase of this system can be written as:

$$\begin{aligned} \angle\tilde{G}(s)\Big|_{s=j\omega_{unity}} &= \angle\left(\frac{1}{s^2+\beta_S\cdot s+(\Delta\omega)^2}\right)_{s=j\omega_{unity}} \\ &= -tan^{-1}\left(\frac{\beta_S\cdot\omega_{unity}}{(\Delta\omega)^2-\omega_{unity}^2}\right) \end{aligned} \tag{3.31}$$

For 1° phase error, term inside the inverse tangent function should be 0.02. This condition results in the following equation:

$$\boxed{(\Delta\omega)^2 = \sqrt{50\cdot\beta_S\,\omega_{LPF}+\omega_{LPF}^2}} \tag{3.32}$$

In addition, gain of this envelope at the low pass filter cut off frequency can also be written as:

$$\left|\frac{1}{s^2+\beta_S\cdot s+(\Delta\omega)^2}\right|_{s=j\omega_{LPF}} = \sqrt{\frac{1}{\left((\Delta\omega)^2-\omega_{LPF}^2\right)^2+(\beta_S\cdot\omega_{LPF})^2}} \tag{3.33}$$

Second term in the denominator is very small comparing with the first term under the phase assumption. At DC frequency, gain can be expressed as:

$$\left|\frac{1}{s^2+\beta_S\cdot s+(\Delta\omega)^2}\right|_{s=0} = \frac{1}{(\Delta\omega)^2} \tag{3.34}$$

Eq.3.35 shows 10% gain error condition.

$$\boxed{\omega_{LPF}^2 = 0.09\cdot(\Delta\omega)^2 \Rightarrow \Delta\omega = 3.3\cdot\omega_{LPF}} \tag{3.35}$$

These both equations indicate the minimum mismatch amount to ignore the phase and gain changes depending on frequency. According to these results, frequency dependency of gain is negligible if mismatch amount is sufficiently higher than the low pass filter cut-off frequency. On the other hand, frequency dependency of phase not only depends on the low pass cut-off frequency but also sense mode bandwidth. This result shows that if bandwidth is low enough, mismatch amount can decrease to low pass cut-off frequency. Nevertheless, gain condition for mismatch express that mismatch amount should be larger than approximately 3 times of the low pass filter cut-off frequency. Correspondingly, if bandwidth is low enough, mismatch amount can roughly be taken as 3 times of the low-pass filter cut-off frequency.

Above analysis say that even quality factor is infinite, if condition for gain is satisfied, envelope model can be taken as a simple gain stage and controller can be designed according this loop. This conclusion is wrong. Though, frequency characteristics of the sense dynamics do not affect the system in the desired bandwidth, it will cause significant stability problems for high frequencies. This problem occurs if gain increase at resonance is not compensated by the integrator and low pass filter. Otherwise, over-all loop gain exceeds 0 dB. At this frequency, there is also sudden phase drop around 180° that ensures open-loop phase is much smaller than -180°. In Bode plot analysis, this fact tells that system is instable. In fact, system may not be instable since Bode plot analysis for stability is valid for simple systems such as analog amplifiers. More powerful tools, such as Nyquist plots, should be used for stability. Besides, even Bode plot analysis does not give direct information about system stability, it can be used a rough analysis. In simulations, it is observed that if gain increase due to resonance characteristics of envelope model is suppressed by the low-pass filter and integrator, transient performance is almost same as the designed results. Otherwise, close-loop settling performance becomes very poor; it can even be instable. Therefore, preventing the loop gain from reaching 0dB at resonance is a good method to have a system with a proper transient performance and safe stability margin. It can be attained, if the gain at envelope model at resonance is suppressed by the low pass filter and integrator in a substantial amount. After suppressing the increase of loop gain at envelope resonance, sense dynamics can now be modeled as a simple gain stage and pure integrator can be used a controller.

Mathematics of this condition is simple. Firstly, condition of taking sense envelope model as a gain stage implies that its characteristics in the band are flat. On the other hand, after the cut-off frequency of the system, there is a sudden gain increase which will cause significant stability problems. For low frequency values, gain of the envelope model is given in Eq. 3.36 and gain at resonance is given in Eq. Eq. 3.37. Eq. 3.38 expresses the amount of this increase.

$$\left|\tilde{G}(s)\right|_{s=j0} = \frac{K_G \cdot \Delta\omega}{(\Delta\omega)^2} \tag{3.36}$$

$$\left|\tilde{G}(s)\right|_{s=j\Delta\omega} = \frac{K_G \cdot \Delta\omega}{\beta_S \cdot \Delta\omega} \tag{3.37}$$

$$G_{Inc} = \frac{\Delta\omega}{\beta_S} \tag{3.38}$$

This increase should be suppressed by the integrator and low-pass filter for a meaningful gain margin. The suppression amount at resonance can simply be expressed in Eq. 3.39. First term of this equation shows the gain drop due to integrator and latter term shows the gain drop due to low pass filter. Unity gain frequency is selected as a reference because for 45°, it is a constant value for a given low pass filter: it is independent from sensor parameters.

$$G_{Dec} = \frac{\Delta\omega}{\omega_{unity}} \cdot \left(\frac{\Delta\omega}{\omega_{LPF}}\right)^2 \tag{3.39}$$

Critical amount of mismtach, then, can be found by equalizing 3.39 and 3.38. In order to have a safe stability margin, gain decrease should be larger than the gain increase coming from the sense dynamics.

$$G_{Dec} \geq G_{Inc} \Rightarrow \frac{\Delta\omega}{\beta_S} \geq \frac{\Delta\omega}{\omega_{unity}} \cdot \left(\frac{\Delta\omega}{\omega_{LPF}}\right)^2 \tag{3.40}$$

Therefore, minimum mismatch amount can be expressed as:

$$\boxed{\Delta\omega_{min} = \omega_{LPF} \cdot \sqrt{\frac{\omega_{unity}}{\beta_S}}} \tag{3.41}$$

Eq. 3.41 indicates that minimum mismatch amount increases with decreasing bandwidth. Lower bandwidth means higher quality factors, and higher quality factor is better in terms of better noise performance as it will be shown in Chapter 4. For the current system shown in Table 3.6, this critical amount of mismatch equals to approximately 320 Hz. Figure 3.12 shows Bode plot of open-loop system designed with pure integrator for the critical mismatch expressed by Eq. 3.41. Results are completely consistent with analytical work. Step response is given in Figure 3.13. Step response is almost identical with the system designed for PID controller. Furthermore, there is decaying ringing that is not observed in previous case. Reason for this ringing is the uncompensated envelope response. If mismatch amount is lowered, amplitude of ringing will increase and become dominant in settling. After some point, system becomes instable. This ringing shows the importance of the condition for second controller design approach. Finally, Figure 3.14 shows closed-loop bode plot of sense system. Bandwidth of this system is around 80Hz which is enough for tactical grade applications. Step response and bandwidth simulations are also repeated with complete system and these results are completely consistent with the results obtained using base-band equivalent model.

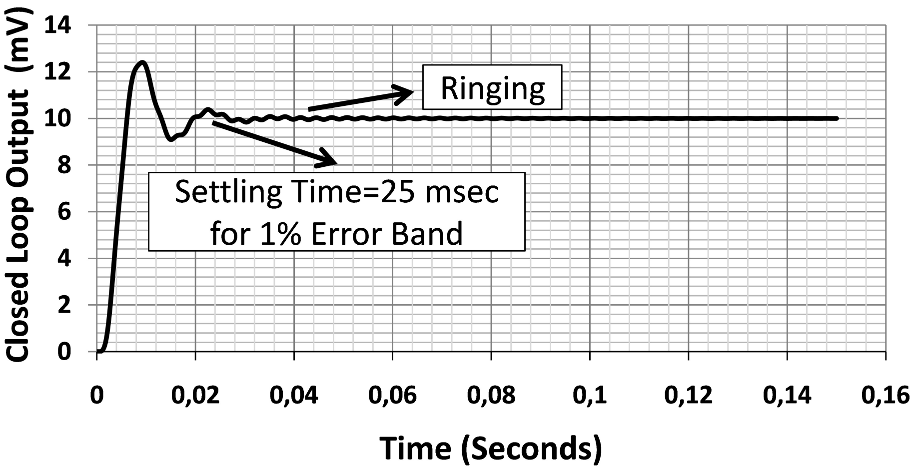

Figure 3.13: Step response for sense system with $\Delta f = 320Hz$.

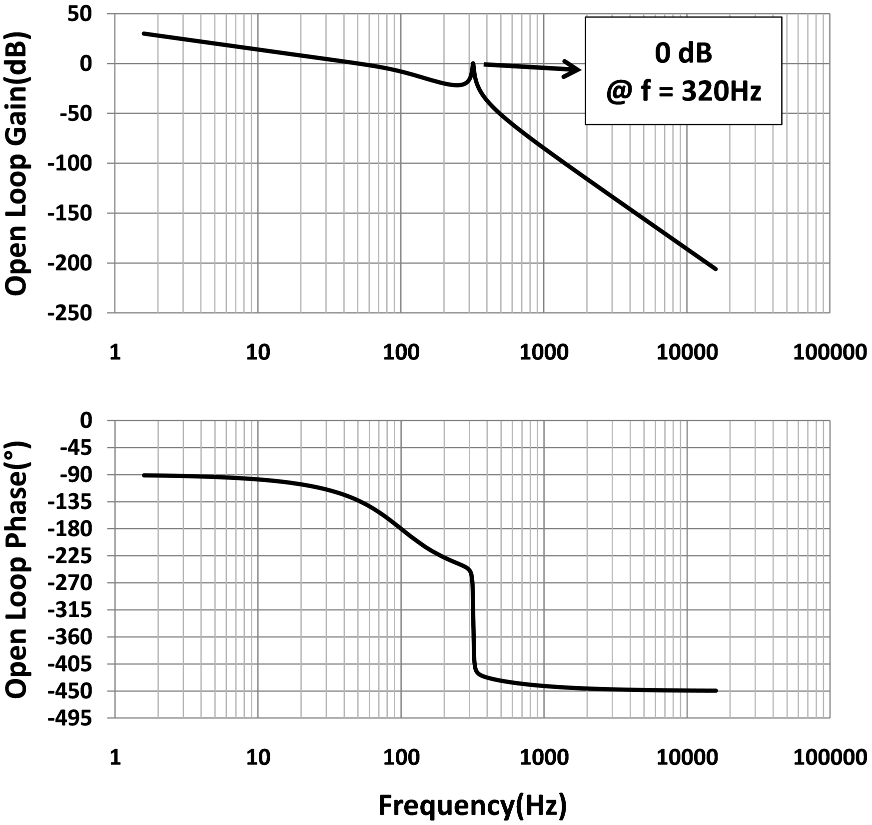

Figure 3.12: Open-loop Bode plot for sense system with $\Delta f = 320Hz$.

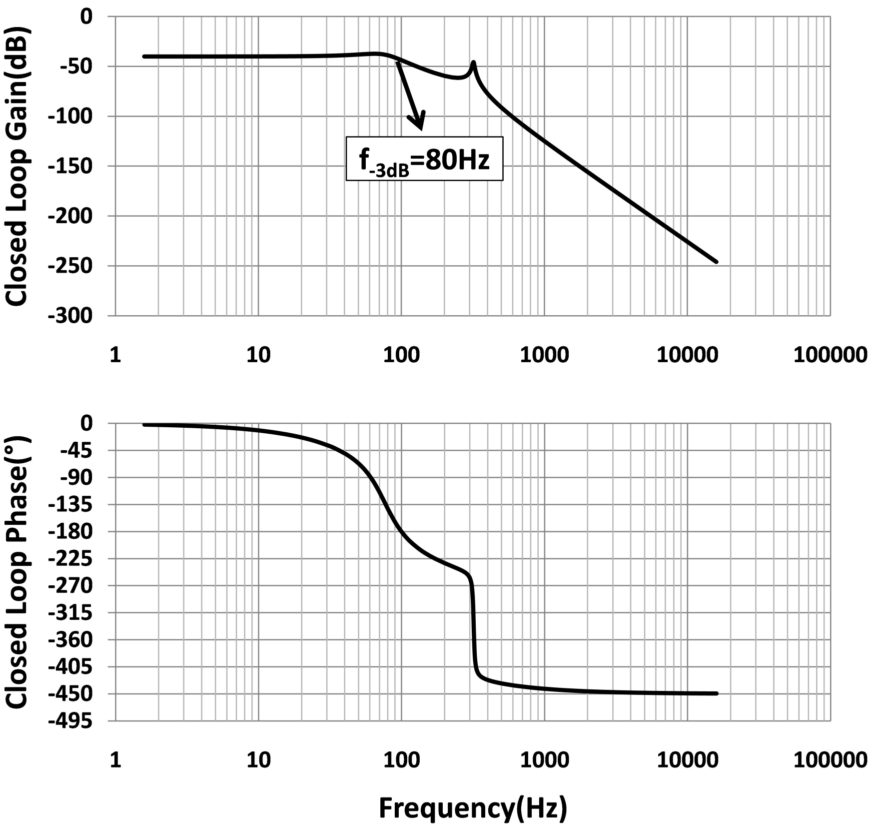

Figure 3.14: Closed-loop Bode plot for sense system with $\Delta f = 320Hz$.

3.4 Summary

The true controller design procedure is vital in terms of the functionality and the system performance. Since the architecture of the sense control loop is not LTI, it is difficult to follow an analytical design procedure. This chapter gives the base-equivalent model of sense dynamics and develops an analytical design procedure for PID controller and pure integrator controller. It is concluded that former controller is a powerful solution for a generic case, but if the resonance frequency separation between the drive and sense modes is high enough, pure integrator can be used. In that controller design approach, the sense dynamics can be modeled as a single gain stage. Minimum mismatch amount, which allows this design procedure in a safe manner, is also discussed in details.

CHAPTER 4

PERFORMANCE ANALYSIS AND CMOS IMPLEMENTATION

The discrete implementation of the analog controller consumes large volume. In addition, some necessary compensates used in the discrete implementation are quite expensive. CMOS provides a good solution for the miniaturization of the system and the cost reduction. On the other hand, reaching the performance of each discrete component is not an easy task in CMOS implementation, but it is possible to reach the overall performance of the system implemented with the discrete components with a proper system design in CMOS. The system limitations should be known for a good system design. Noise sources and their effects on the system performance should be analyzed carefully. This chapter gives a detailed work on the noise analysis introducing *noise folding* concept which increases electronics noise in a substantial amount. The rest of the chapter is organized as follows: Section 5.1 gives a brief information about the front-end electronics. Section 5.2 explains the basic blocks used in sense and drive controller discussed in Chapter 2 and Chapter 3. Section 5.3 analyzes the limitations coming from the circuit imperfections. Section 5.4 analyzes secondary noise effects quantitatively and qualitatively. Section 5.5 summarizes the chapter.

4.1 Front-end Electronics

In this thesis, the front-end electronics are implemented with the discrete electronics. Details of this part can be found in [3]. Circuit level diagram of the front-end electronics for the sense mode is shown in Figure 4.1. In this system, C_{int} is the integration capacitor, R_{DC} is the DC feedback resistor providing the DC bias of the Op-Amp. In sense mode, capacitive type

TIA is selected because of its high gain and low noise operation. This type of preamplifier gives the displacement information. Therefore, the regulated parameter in the sense mode is displacement of the sense motion. Drive mode front-end electronics is almost same with the front-end electronics of the sense mode. In the drive mode, there is only one read out electrode, so the second terminal of the instrumentation amplifier is grounded. In addition, resistive TIA is used for velocity regulation, since the Coriolis force is proportional to the drive mode velocity. In addition, use of the resistive type TIA does not require a phase shifter in the self-oscillation loop (positive feedback path), but capacitive type does.

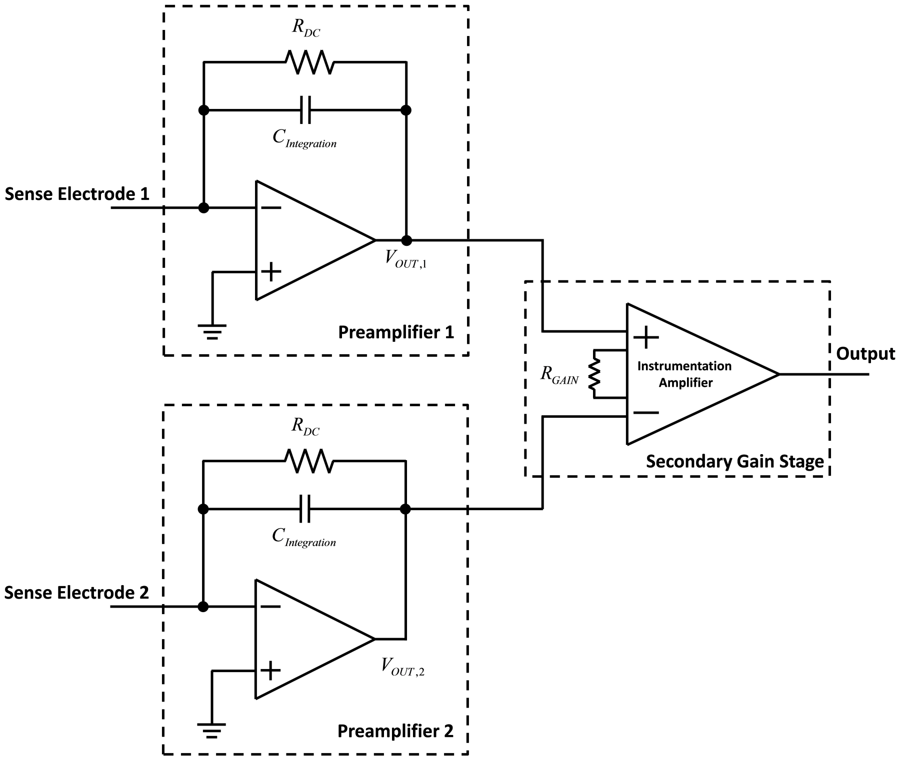

Figure 4.1: Circuit diagram of front-end electronics.

4.2 CMOS Design for Analog Controllers

Standard CMOS 0.6 μm process of X-Fab is used for the CMOS implementations of the analog controllers. The analog controller for the proposed systems mentioned in Chapter 2 and Chapter 3 are composed of a demodulator, a low-pass filter, an instrumentation amplifier, a controller (PI in drive mode and PID in sense mode), and a modulator. The implementations of these blocks are very easy, and there is no difference between the CMOS and discrete implementation. Core element of these blocks is Op-Amp. Maximum frequency of the signal which is processed in the controller does not exceed 15kHz in typical gyroscopes. As a result, there is no significant bandwidth challenging for Op-Amp design. Noise and offset are the two significant limitations for circuits of analog processing blocks. Especially, blocks operating at the base-band are very susceptible to offset and 1/f noise. Special topologies, such as Chopper stabilized and offset nullifying circuits, can solve both of these problems. However, it increases the implementation difficulty. Scope of this design is to verify the functionality instead of getting better performance. In 2007, it is observed that the input referred offset is higher than the predicted values indicated in process sheet [25]. Therefore, an external offset is necessary in order to operate the system to prevent the saturation of Op-Amps in later stages. Furthermore, an Op-Amp of X-Fab is used for this system. In the following subsections, blocks of the analog controller are going to be discussed.

4.2.1 Modulator

The modulator and demodulator used in this work is a simple switching modulator [25]. The Idea behind this type of a modulator is mixing square wave with the message signal. In demodulator, it is almost equivalent to multiplication with sinusoidal signal, since higher harmonics are rejected with the low-pass filter following the demodulator. Mathematics of this demodulation is expressed in Eq. 4.1.

$$
\begin{gathered}
V'_{out} = V_m \cdot sin(\omega \cdot t) \cdot \frac{4}{\pi} \cdot \textstyle\sum_{k=1}^{\infty} \frac{sin\left((2k-1)\cdot\omega\cdot t\right)}{2k-1} \\
V'_{out} = V_m \cdot sin(\omega \cdot t) \cdot \frac{4}{\pi} \cdot sin(\omega \cdot t) + V_m \cdot sin(\omega \cdot t) \cdot \frac{4}{\pi} \cdot \textstyle\sum_{k=2}^{\infty} \frac{sin\left((2k-1)\cdot\omega\cdot t\right)}{2k-1} \\
V'_{out} = V_m \cdot sin(\omega \cdot t) \cdot \frac{4}{\pi} \cdot sin(\omega \cdot t) + \underbrace{V_m \cdot \frac{2}{\pi} \cdot \sum_{k=2}^{\infty} \frac{cos\left((2k-2)\cdot\omega\cdot t\right) - cos\left(2k\cdot\omega\cdot t\right)}{2k-1}}_{\text{High frequency terms which are rejected by the low pass filter}}
\end{gathered}
\tag{4.1}
$$

The implementation of this circuit is easy. A 2x1 analog multiplexer which switches between the input and inverted input performs this operation. The clock of this analog multiplexer is the carrier signal. Circuit configuration is shown in Figure 4.2.

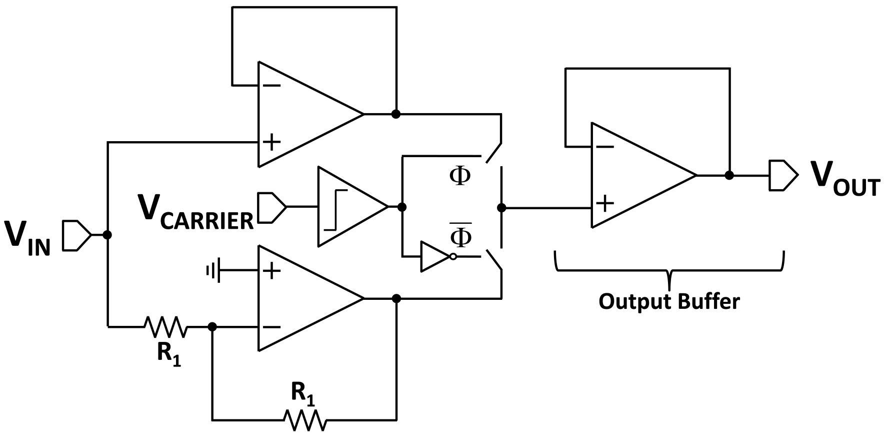

Figure 4.2: Circuit diagram of the modulator.

4.2.2 Low Pass Filter

The low pass filter is used to reject higher the harmonics coming from the demodulation. Low pass filters can be implemented with passive elements, but required capacitance and resistance values are quite high. Active filters do not require such high values, and they can give gains. Most popular active filter types are *multi feedback topology* (MFB) and Sallen Key filters. Main advantage of these filters is their component tolerance. In the drive and sense modes, different types of low pass filters are used. In the drive mode, gain of the low pass filter is critical, since it determines the amount of the deflection. For this reason, low pass filter gain programmability provides changing of the drive mode oscillation amplitude. With gain configuration, the MFB is simpler than the Sallen Key type low pass filter (it needs four passive components). On the other hand, the low pass filter gain only increases the loop gain, and this can also be achieved with the controller gain. To put differently, the gain of the low pass filter is not critical in the sense mode. In this case, Sallen Key configuration is simpler than MFB topology. For this reason, MFB is used in the drive mode controllers, and Sallen Key is used in the sense mode controllers. Figure 4.4 shows the circuit of the MFB type low pass filter. Eqs.4.2,4.3,4.4 show the transfer function, bandwidth, and gain of the MFB topology, respectively. Figure 4.3 shows the circuit of the Sallen Key type low pass filter. Eqs.4.5,4.6 show the transfer function and bandwidth, respectively for the Sallen-Key topology.

$$H_{SK}(s) = -\frac{1}{A \cdot s^2 + B \cdot s + C} \tag{4.2}$$

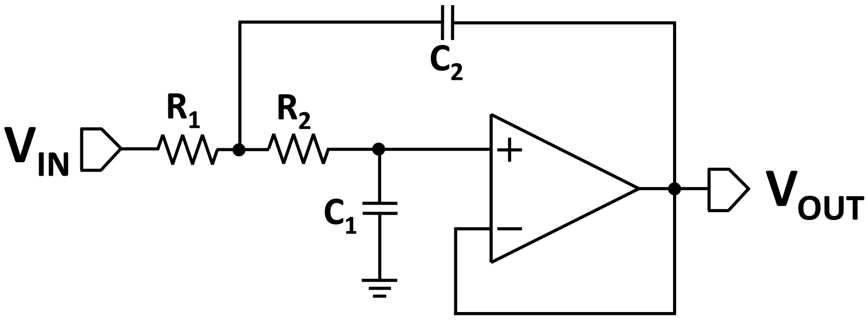

Figure 4.3: Sallen Key type low-pass filter.

where,

$$A = R_1 \cdot R_3 \cdot C_1 \cdot C_2$$
$$B = C_2 (R_1 + R_3) + \frac{R_1 \cdot R_3 \cdot C_2}{R_2}$$
$$C = \frac{R_2}{R_1}$$

$$f_C = \frac{1}{2\pi \cdot \sqrt{R_2 \cdot R_3 \cdot C_1 \cdot C_2}} \tag{4.3}$$
$$K_{MFB} = \frac{R_2}{R_1} \tag{4.4}$$

$$H_{SK}(s) = \frac{A}{s^2 + B \cdot s + C} \tag{4.5}$$

where,

$$A = C = \frac{1}{R_1 \cdot R_2 \cdot C_1 \cdot C_2}$$
$$B = \frac{1}{(R1//R2) \cdot C_2}$$

$$f_C = \frac{1}{2\pi \cdot \sqrt{R_1 \cdot R_2 \cdot C_1 \cdot C_2}} \tag{4.6}$$

4.2.3 Instrumentation Amplifier

The instrumentation amplifier is a difference amplifier. The main advantage of this topology is that it has a very high common mode rejection ratio (CMRR) which is satisfied by matching of resistors even if the CMRR of the Op-Amp is not sufficiently high. Its gain can be

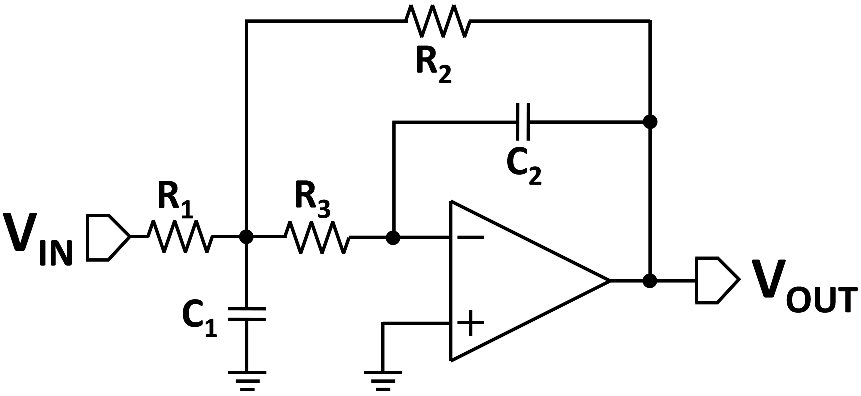

Figure 4.4: MFB type low-pass filter.

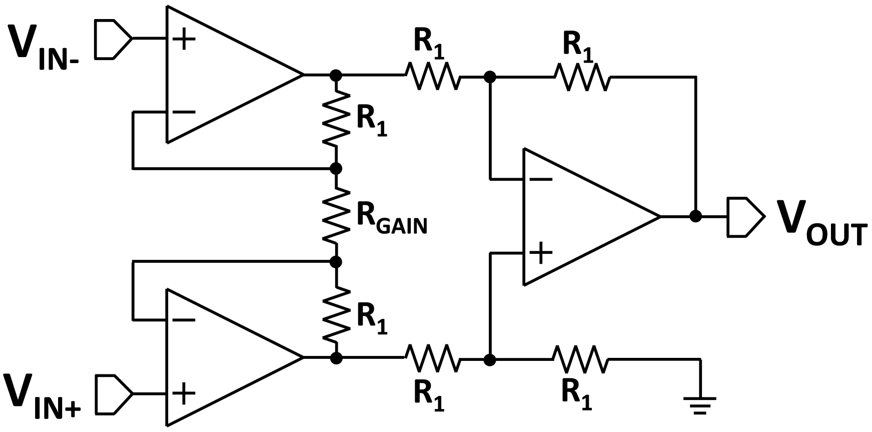

Figure 4.5: Circuit diagram of instrumentation amplifier.

programmed with a single resistor, as well. The circuit diagram is shown in Figure 4.5, and the gain expression is given in Eq. 4.7.

$$K_{InsAmp} = \frac{2R_1 + R_{GAIN}}{R_{GAIN}} \tag{4.7}$$

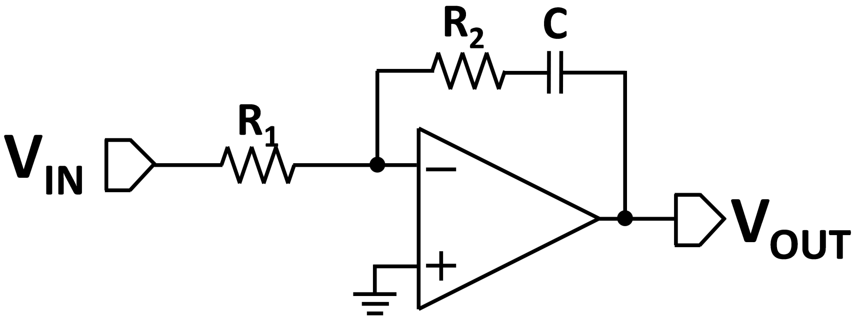

Figure 4.6: Circuit diagram of PI controller.

4.2.4 PI Controller

A single Op-Amp, one capacitor, and two resistors are enough for a PI controller as Figure 4.6 shows. Its parameters are expressed in Eq. 4.8 and Eq. 4.9.

$$K_P = -\frac{R_2}{R_1} \tag{4.8}$$

$$K_I = -\frac{1}{C \cdot R_1} \tag{4.9}$$

4.2.5 PID Controller

The PID controller needs four Op-Amps if it is desired to set PID parameters independently. The circuit configuration is shown in Figure 4.7. Its parameters are expressed in Eq. 4.10, Eq. 4.11, and Eq. 4.12. In Figure 4.7, R_C is the compensation resistor which limits the gain for high frequencies. This resistance reduces noise and improves the stability of the PID controller.

$$K_P = \frac{R_{P2}}{R_{P1}} \cdot \frac{R_{GAIN}}{R_1} \tag{4.10}$$

$$K_I = \frac{1}{R_I \cdot C_I} \cdot \frac{R_{GAIN}}{R_1} \tag{4.11}$$

$$K_D = R_D \cdot C_D \cdot \frac{R_{GAIN}}{R_1} \tag{4.12}$$

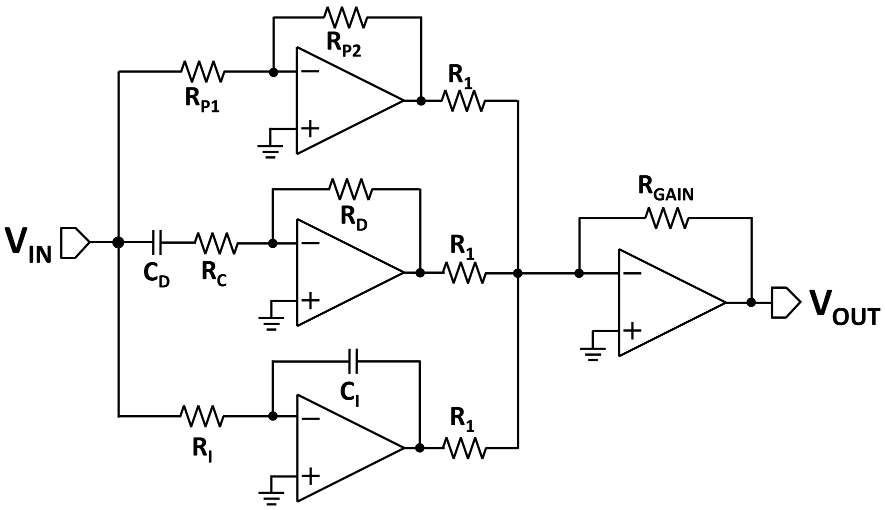

Figure 4.7: Circuit diagram of PID controller.

4.3 Performance Analysis

Major noise source of a gyroscope system is composed of electronics noise and a mechanical Brownian noise. The effect of the drive mode system has a negligible effect on the noise performance of the complete system. For this reason, in the first order analysis of the noise, sense mode will be analyzed. The effect of the noise sources can be investigated in the sense mode closed-loop with the following procedures. 1) Find out the input referred force noise of the sensor which is nothing but the Brownian noise. 2) Find out the output referred noise of the preamplifier. Output-referred noise is preferred, because preamplifier carries out current-to-voltage conversion and current noise is critical if the input current noise of the Op-Amp is not low enough. In other words, there are two dominant noise sources of the preamplifier Op-Amp. These noise sources can be combined at the output. 3) Find out each individual input referred noise of the circuit blocks of the controller. Since, all of the blocks in the controller process voltages, feedback loop is conducted in the voltage domain. As a result, the input referred voltage noise is enough for characterizing the over-all system performance. 4) Find out noise gains of each individual noise sources at the system output. Then, divide this amount with the closed-loop gain in order to characterize input-referred rate-equivalent noise. First and second steps are performed in [3]. In this section, noise contributions of the controller at the output block will be, firstly, discussed.

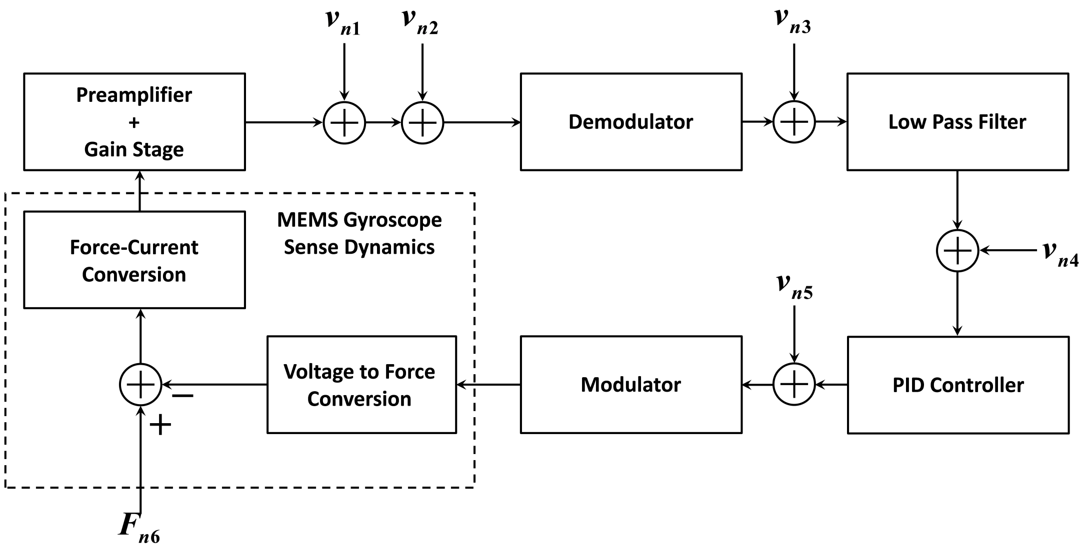

Figure 4.8: Noise sources of sense system.

Loop gain for each noise source is different. Difference comes from the feed-forward gain. Noise transfer function for a generic noise source, v_i can be written as:

$$H_{noise,i}(s) = \frac{A_i(s)}{1 + S_{OL}(s)} \tag{4.13}$$

where, open-loop transfer function can simply be expressed for the compensated system with 45° phase margin combining 3.25 and 3.26. Table 4.1 shows feed-forward gains of the noise sources shown in Figure 4.8.

$$\begin{aligned} S_{OL}(s) &= 2\pi \cdot \overbrace{f_{unity,gain}}^{50\text{ Hz}} \cdot F(s) \cdot \frac{1}{s} \\ &= 314 \cdot F(s) \cdot \frac{1}{s} \end{aligned} \tag{4.14}$$

In fact, even if the noise analysis can be performed by treating the noise as a signal, it results in some discrepancies with the actual system performance. In the operation of the switching modulators, it is assumed that the input of the modulated system is band-limited. In a typical operation, this assumption is true, because open-loop itself behaves as a low pass filter that does not allow the high frequency components exist in the loop. On the other hand, the injected noise of the electronic components is not needed to be band-limited and this in-

Table 4.1: Feed-forward gains of the noise sources.

v_i	Description of the noise source	Forward Gain, $A_i(s)$
v_{n1}	Output referred noise of the pre-amplifier and subsequent gain stage	$K_{dmod} \cdot F(s) \cdot C(s)$
v_{n2}	Input referred noise of the demodulator	$K_{dmod} \cdot F(s) \cdot C(s)$
v_{n3}	Input referred noise of the low-pass filter	$F(s) \cdot C(s)$
v_{n4}	Input referred noise of the controller	$C(s)$
v_{n5}	Input referred noise of the modulator	$\tilde{G}(s) \cdot K_{dmod} \cdot F(s) \cdot C(s)$
v_{n6}	Input referred force-equivalent noise of sense mode of gyroscope	$\tilde{G}(s)/K_{V/F} \cdot K_{dmod} \cdot F(s) \cdot C(s)$

jected noise cause failure of the above assumption even if the feedback signal is band-limited. Failure of this assumption comes from the noise folding of the switching systems, such as sample and hold circuits. In the following section, the noise folding of the modulators and demodulators will be discussed in details.

4.3.1 Noise Folding in Modulator and Demodulator

In the previous works, the modulator is simply modeled as a simple gain stage in finding the output noise of the gyro sense system [2, 3, 47]. However, the signal gain is different than the noise gain because of noise folding in the switching modulator. The noise folding due to the demodulator comes from the modulation property in the frequency domain. In the operational principle of the switching modulator, it is assumed that the input of the demodulator is band-limited. This is correct for the rate signal, but noise is spread into a complete band. In fact, the feedback signal coming from the sensor is filtered by the mechanical resonator. By the same token, the low pass filter and the controller reject higher frequency components, as well. On the other hand, the electronic noise contribution of the preamplifier and the following gain stage directly feeds the modulator input. Since, the feedback is very weak for higher frequencies, the noise at the demodulator input is directly composed of its own input referred noise and the front-end electronics noise. This input referred noise is folded into the band under interest which increases the noise density in this band. This folding is visualized in Figure 4.9.

It is seen that each segment, whose bandwidth equals to the sampling frequency, is multiplied by the Fourier coefficient of the square wave which demodulates the corresponding segment

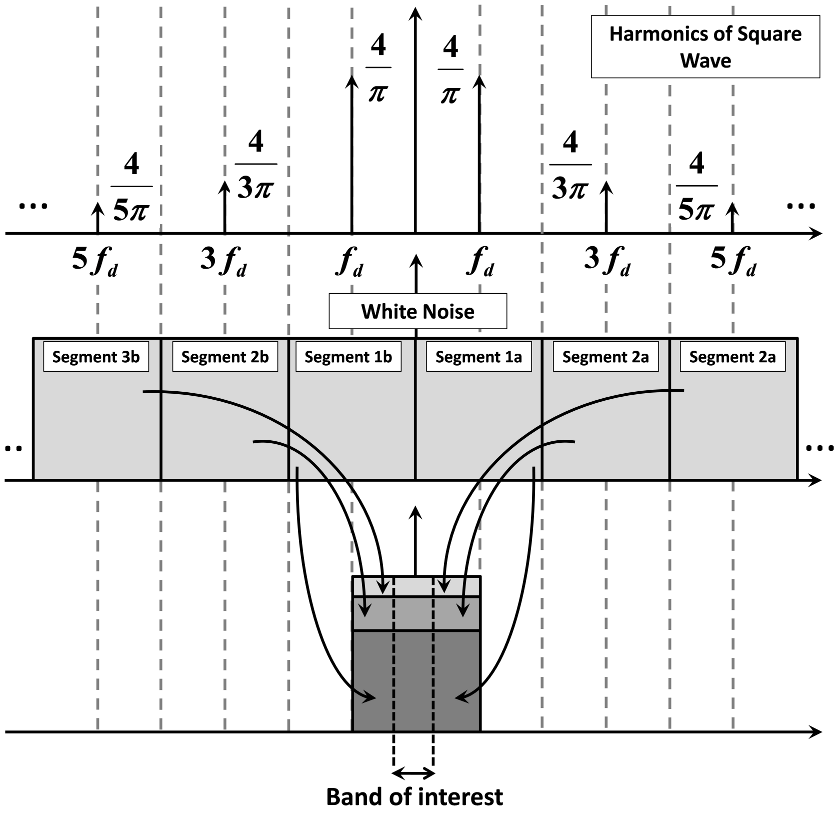

Figure 4.9: Visualization of noise folding in demodulator.

to the base-band. The amount of the new density depends on the noise bandwidth at the demodulator input and the folding amount. The noise at the demodulator input is composed of the front-end electronics noise and the demodulator's input referred noise. The noise contribution of the demodulator is mainly composed of the Op-Amps used in buffering and inverting stages. On the other hand, same amount of the noise is also valid for the preceding stages constituting the front-end electronics. Since these noises are increased with the significant gain of the preamplifier and secondary gain stage, the contributions of these noise sources is much larger than the noise of the demodulator itself. In addition, since the noise is determined by these stages, the noise band is nothing but the bandwidth of the front-end electronics. As a result, a rough analysis can be performed to determine the amount of the folding. Neglecting the noise at the out of the band of electronics, effect of the i^{th} segment is:

$$v_{ni} = w \cdot \frac{4}{\pi \cdot (2i - 1)} \tag{4.15}$$

where, w is the white noise density. Folding of the Flicker noise is negligible, because this noise source is only effective in lower frequencies. For higher frequencies, white noise is dominant, thus the folding of the white noise source is much more than folding of Flicker noise.

$$v_n = \sum_{i=1}^{i=k} v_{ni} = w \cdot \sum_{i=1}^{i=k} \frac{4}{\pi \cdot (2i-1)} \tag{4.16}$$

where, $k = \dfrac{BW}{2 \cdot f_d}$ neglecting the noise out of the noise band, BW.

Summation in Eq.4.16 can be approximated using Riemann sum by excluding the some of the first terms. Eq. 4.16 can be written in the following generic form using Riemann summation.

$$v_n = w \cdot \frac{4}{\pi} \left(\sum_{i=1}^{i=k0-1} \frac{1}{2i-1} + \underbrace{\sum_{i=k0}^{i=k} \frac{1}{2i-1}}_{\int_{x=k0}^{x=k+1} \frac{\mathrm{d}x}{2x-1}} \right) \tag{4.17}$$

$k0$ should be determined in order to minimize the error resulting from the Riemann summation. If the difference between $1/(2k0-1)$ and the integration from $k0$ to $k0+1$ is small enough, then the overall percentage error is guaranteed to be small enough, as well. 10% error is a fair error for noise analysis. Therefore, if the difference mentioned above corresponds to the 10% of the term $1/(2k0-1)$, overall error will be smaller than 10%. Using this approach, the following equation can be obtained.

$$0.9 \cdot \frac{1}{2k0-1} = \int_{x=k0}^{x=k0+1} \frac{\mathrm{d}x}{2x-1} = 0.5 \cdot ln\left(\frac{2k0+1}{2k0-1}\right) \tag{4.18}$$

Rearranging the terms, following equation can be obtained.

$$1.8 = ln\left(\frac{2k0+1}{2k0-1}\right) \cdot (2k0-1) \tag{4.19}$$

Solving Eq. 4.19, k0=5 is obtained. As a result, can be written as followings.

$$\begin{aligned} v_n &= w \cdot \frac{4}{\pi} \left(\sum_{i=1}^{i=4} \frac{1}{2i-1} + 0.5 \cdot ln\left(\frac{2k+1}{9}\right)\right) \\ &= w \cdot \frac{4}{\pi} \left(1 + 0.676 + 0.5 \cdot ln\left(\frac{2k+1}{9}\right)\right) \end{aligned} \tag{4.20}$$

In current system, bandwidth of the second gain stage is 700kHz (for 20 gain) [37]. In addition, the resonance frequency of the drive mode is around 10kHz, therefore k is approximately

35. Then, Eq. 4.3.1 becomes:

$$v_n = \underbrace{w \cdot \frac{4}{\pi} \cdot (1 + 1.71)}_{\text{Noise Gain}} \tag{4.21}$$

This equation shows that even if the signal gain of demodulation equals to $4/\pi$, noise gain for white noise is approximately 2.71 times of this value. As it has been mentioned before, this folding is not valid for Flicker noise. In fact, Flicker noise also folds, but white noise dominates this amount. Thus, gain equals to signal gain at demodulator for Flicker noise. As a final note, noise contribution of the front-end electronics includes not only white noise, but also the band-limited noise coming from the current noise of the preamplifier Op-Amps and biasing resistor. Since, preamplifier is nothing but an integrator filtering high frequency noises, the folding amount of these current noises is negligible.

Same case is also true for modulator. Noise folds to the band of interest which is around drive resonance frequency. Fortunately, its input noise is band-limited due to the filter characteristics of the controller and low-pass filter. On the other hand, input stages of the modulator have a wide band white noise. Eq. 4.21 can be used to determine the noise gain of the input referred white noise of modulator. The bandwidth of the input stages is expected to be 1MHz, so that noise gain is roughly 2.9. Folding of its Flicker noise is again negligible, so modulator noise gain for Flicker noise equals to the signal gain, as well.

Even if the gain of the white noise increases due to the folding, noise at the output of the low pass filter, after the demodulator is at the base-band. For this reason, the noise increase due to the folding at the output can be interpreted as the increase of the input referred noise of the demodulator in the band of the interest. This new noise is different than the actual input referred white voltage noise density w, so this new input referred noise is called effective white noise density, w_{eff}. Similar interpretation can also be made for the modulator. This interpretation of the noise folding enables us to follow the same procedure of the signal analysis in the noise analysis. Figure 4.10 and Eq. 4.22 visualize this approach. In Eq. 4.22, K_{fold} is the ratio between the noise gain and signal gain of the modulator and demodulator.

$$v_{n,out,mod} = \underbrace{w \cdot K_{fold}}_{w_{eff}} \cdot A_i - v_{out,n} \cdot \beta_i \tag{4.22}$$

Result of Eq. 4.22 enables to use the system proposed in Chapter 3 in the noise analysis, as well. To put it differently, effective white noise (w_{eff}), is the base-band equivalent noise of the

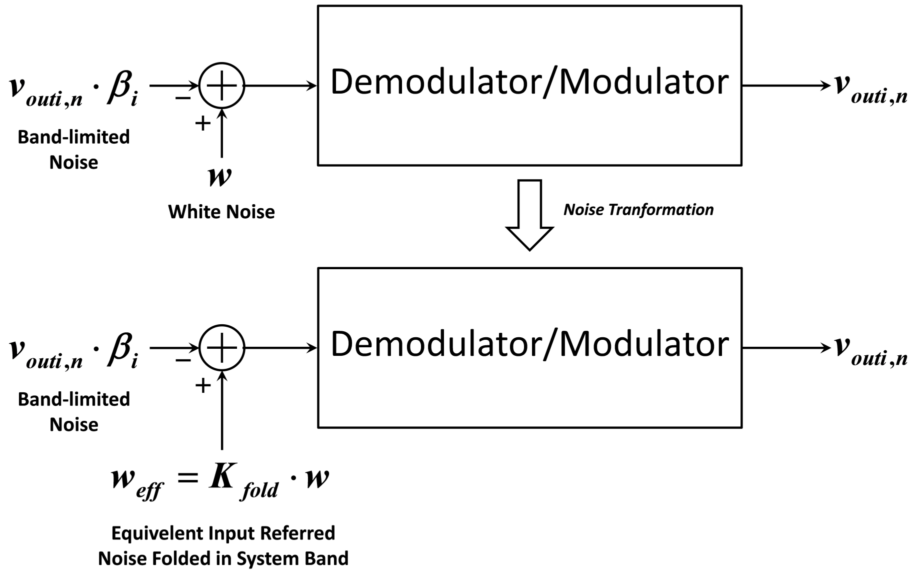

Figure 4.10: Effect of folding on input referred noise.

modulators/demodulators. Following section is going to analyze the amount of electronics' noise.

4.3.2 Noise Sources

The front-end electronics noise performance is discussed in [3]. Noise expression of an output of the second gain stage, which is made up with an instrumentation amplifier, is expressed as:

$$\begin{aligned} v_{n1} = \Bigg(& 2 \cdot i^2_{n,preamp} \cdot \left(\frac{1}{sC_{int}}\right)^2 \cdot 2 + i^2_{n,RDC} \cdot \left(\frac{1}{sC_{int}}\right)^2 \\ & +2 \cdot v^2_{n,preamp} \cdot \left(1 + \frac{C_{in,eff}}{C_{int}}\right)^2 + v^2_{n,insamp} \Bigg)^{0.5} \cdot G_{insamp} \end{aligned} \tag{4.23}$$

where, $i_{n,preamp}$ is the input referred current noise of the preamplifier Op-Amp, $i_{n,RDC}$ is the current noise of the feedback resistance to set DC operating points of the amplifier, $v_{n,preamp}$ is the input referred voltage noise of the preamplifier Op-Amp, and v_{insamp} is the input referred voltage noise of the second gain stage. C_{int} is the integration capacitance of the preamplifier, and $C_{in,eff}$ is the total capacitance between preamplifier input and ground. This capacitance is composed of the static capacitance of the sensor and input capacitance of the preamplifier. 2 in noise expression comes from the differential reading of the sense mode. Noise of the second gain (instrumentation amplifier) stage is gain dependent, since noise of the last stage of the instrumentation amplifier and resistances used in it have less affect with increasing gain. If gain is sufficiently high, then input referred noise of the instrumentation amplifier is composed of two times of the input referred voltage noise of the Op-Amps used in the first stage (since there are two Op-Amps) and voltage noise of the gain resistance. Flicker noise of this part is neglected; Flicker dominated portion is out of the band of interest after demodulation.

As it was mentioned before, current noises of the Op-Amps cause a band-limited noise at the second gain stage output. As a result, the folding of these noise sources due to modulation has a negligible effect. On the other hand, other noise sources are white noise in a wide band, therefore folding of them is important.

Input referred noise of the demodulator is only composed of the noise of the Op-Amps used for the buffering and inverting stages. Since similar gained version of these noise amounts also come from the preceding front-end electronics, contributions of these noise sources can be neglected. On the other hand, the output of the demodulator is now at base-band, so it suffers from the Flicker noise, and offset drifts in a significant amount. This contribution can be decreased by increasing the gain before demodulation. This is equivalent to the increase in β_i. Noise contribution of the following stages, which is dominated by the Flicker noise, can be minimized in a similar manner.

Therefore, it can be concluded that system noise is dominated by noise of the front-end electronics. Effective input referred white noise density can be found by using Eq. 4.23 and noise folding property shown in Eq. 4.21. This effective white noise density can be written as:

$$w_{eff} = \sqrt{2 \cdot v_{n,preamp}^2 \cdot \left(1 + \frac{C_{in,eff}}{C_{int}}\right)^2 + v_{n,insamp}^2} \cdot G_{insamp} \cdot K_{fold} \tag{4.24}$$

Even current noises are shaped by the integrator, its response is flat for the system band. As a result, this noise source behaves as a white noise, as well. Note that the folding of this noise source is less than the folding of voltage noises, so its folding effect is ignored. Combining this result with Eq. 4.24, equivalent voltage noise density coming from the front-electronics can be found as:

$$v_{n1} = \sqrt{w_{eff}^2 + v_{n,insamp}^2} \cdot G_{insamp} \tag{4.25}$$

Although the effect of the Flicker noise can be minimized by increasing the gain before the demodulation, its effect still dominates the complete system performance if operation length is long. To put it differently, Flicker noise determines the bias instability. Therefore, for the other noise sources, even if white noise contributions are neglected, Flicker noise contributions should be taken into account. Eq. 4.26 shows the input referred voltage noise of demodulator. This noise source is mainly composed of the Flicker noise of the output buffer of demodulator. Note that noise of the output buffer is divided by signal gain to obtain the input referred value.

$$v_{n2} = v_{n,Flicker} \cdot \frac{1}{K_{dmod}} = \sqrt{\frac{K_{1/f}}{K_{dmod}^2} \frac{1}{f}} \tag{4.26}$$

where, $K_{1/f}$ is the constant for Flicker (1/f) noise. By the same token, v_{n3} can be written as in terms of Flicker noise of the Op-Amp. Since, Flicker noise is dominant noise source for lower frequencies, in the low pass filters capacitors can be taken as open-circuit to determine input referred voltage noise of the low pass filter. In that configuration, Sallen-Key low pass filter behaves as a buffer. Thus, input referred voltage noise of the low pass filter can be expressed as:

$$v_{n3} = v_{n,Flicker} = \sqrt{\frac{K_{1/f}}{f}} \tag{4.27}$$

Similar work can be conducted for controller. Controller includes 4 Op-Amps. Effect of last summer stage is very low, since preceding stages gives huge gain to low frequency signals including input referred voltage noise of the input Op-Amps. As a result, they dominate the noise performance of controller. Taking the Flicker noise of these three Op-Amps into account, following equation can be obtained:

$$v_{n4} = \sqrt{3} \cdot v_{n,Flicker} = \sqrt{3} \cdot \sqrt{\frac{K_{1/f}}{f}} \tag{4.28}$$

Because of the filtering characteristics of the controller, most of the noises coming from the former stages are rejected. Therefore, it is not true to neglect white noise contribution of the noise sources after the controller. For that reason, the input referred noise is composed of both Flicker and white noise. Using the folding property of the modulator and combining it with the Flicker noise, Eq. 4.29 and Eq. 4.30 are obtained. In Eq.4.30 there are three white noise sources, two of them are input Op-Amps used in the modulator. Their noise folds to the base-band, so their effective value is larger than the actual density values. On the other hand, output noise of the Op-Amp is not folded. In order to refer it in input, its value is divided by the signal gain.

$$v_{n5,1/f} = \sqrt{\frac{K_{1/f}}{K_{dmod}^2}\frac{1}{f}} \tag{4.29}$$

$$v_{n5,white} = v_{n,Op-Amp}\sqrt{\left(\frac{1}{K_{dmod}}\right)^2 + 2\cdot K_{fold,mod}^2} \tag{4.30}$$

$$\tag{4.31}$$

The noise of the mechanical sensor is also a white noise (Brownian noise) which is defined in terms of force. It is expressed in the following equation.

$$F_{n6} = \sqrt{4kT\frac{m_S\cdot\omega_S}{Q_s}} \tag{4.32}$$

In the following section, total noise is going to be derived using individual noise sources discussed in this section.

4.3.3 Total Output Noise Coming From Sense Mode Electronics

The gain of each individual noise sources is given in Eq.4.14 and Table 4.1. If the loop gain of the system is sufficiently high in the system band, then analysis becomes much simpler. In fact, the loop gain starts to decrease at higher frequencies before the system bandwidth. On the other hand, this assumption holds in a big portion of the total bandwidth. In addition, it is also possible to increase the closed-loop bandwidth larger than the desired bandwidth such that the loop gain is high enough in the complete band of interest. This can easily be achieved by increasing the low pass cut-off filter frequency. In a generic case, assuming that the loop gain is much higher than the unity gain in the closed-loop bandwidth is fair. Because of this assumption, the noise gain of the individual noise sources are simplified as Eq. 4.33 indicates.

$$H_{noise} = \frac{A_i}{1+S_{OL}(s)} = \frac{A_i}{1+\beta_i\cdot A_i} = \frac{1}{\beta_i} \tag{4.33}$$

Eq. 4.33 tells that the noise follows the path between the node at which it is identified and the output as Figure 4.11 shows. In fact, all the electronics blocks have flat gains for the system band excluding sensor response. The controller also does not have flat response, but it does not exist in any feedback path. The sensor gain is dependent on frequency, and actual affect of the sensor can be analyzed using envelope model. Because of the resonance characteristics of the envelope model, white noise is shaped. This shaping characteristic becomes affective especially for the low mismatch operation. If the mismatch amount is not low, then the frequency dependent characteristics of the system is negligible, and β_i becomes a simple gain stage. Thus, white effect of white noise can be found by dividing the noises by this scalar. These scalar feedback factors are shown in Table 4.2.

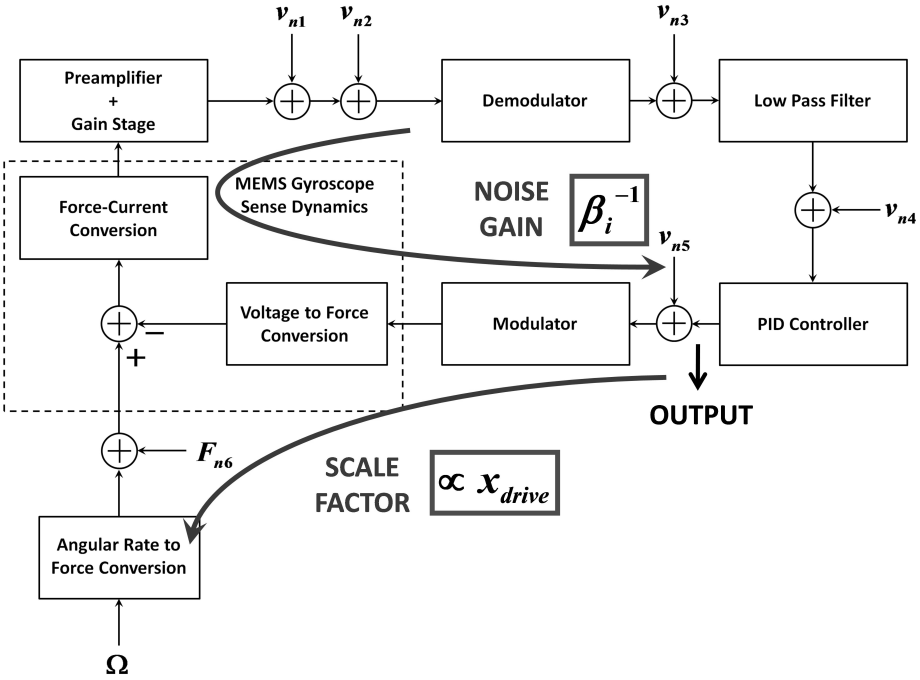

Figure 4.11: Noise paths between the noise sources and the output.

Table 4.2: Feed-back factors for noise sources.

v_i	β_i
v_{n1}	$K_G \cdot K_{mod}/(\Delta\omega \cdot K_{dmod})$
v_{n2}	$K_G \cdot K_{mod}/(\Delta\omega \cdot K_{dmod})$
v_{n3}	$K_G \cdot K_{mod}/(\Delta\omega)$
v_{n4}	$K_{mod}/(\Delta\omega) \cdot K_{LPF}$
v_{n5}	1
F_{n6}	$K_{V/F}$

Combining these results, it is possible to determine the white noise density and the Flicker noise constant. In order to achieve it, it is needed to superpose them in the power domain, since they are uncorrelated noise sources.

$$v_{out,total,white} = \sqrt{\left(\frac{v_{n1}}{\beta_1}\right)^2 + \left(\frac{v_{n5,white}}{\beta_5}\right)^2 + \left(\frac{F_{n6}}{\beta_6}\right)^2} \tag{4.34}$$

$$v_{out,total,1/f} = \sqrt{\left(\frac{v_{n2}}{\beta_2}\right)^2 + \left(\frac{v_{n3}}{\beta_3}\right)^2 + \left(\frac{v_{n4}}{\beta_4}\right)^2 + \left(\frac{v_{n5,1/f}}{\beta_5}\right)^2} \tag{4.35}$$

Table 4.3 shows the parameters for noise densities derived in previous section for discrete front-end electronics, discrete and IC controllers. Datasheets for discrete modulator chip (AD630) does not include any information for noise densities. Effective input capacitance in the below table is composed of not only sensor output capacitance, 5.4pF but also input capacitance of the preamplifier Op-Amp (AD8608) which is 11.4pF and wire bonding capacitance that equals to approximately 1pF. Therefore, resultant effective input capacitance reaches to approximately 18pF. Table 4.4 shows the feedback factor values for each noise source. Table 4.5 shows the expected densities and values of feedback factors using the relations Eqs. 4.25, 4.26, 4.27, 4.28, 4.29, 4.32, and Table 4.4.

Table 4.3: Noise density parameters [37, 38, 39, 40].

System Portior	Noise Source	Values
Front-end Electronics	$v_{n,preamp}$	$6.5nV/\sqrt{Hz}$
	$v_{in,insamp}$	$8nV/\sqrt{Hz}$
	G_{insamp}	20
	$C_{in,eff}$	18pF
	C_{int}	3.9pF
	K_{fold}	2.7
	$i_{n,preamp}$	$10fA/\sqrt{Hz}$
	$i_{n,RDC}$	$\sqrt{4kT/470M} = 18nV/\sqrt{Hz}$
Discrete Electronics	$v_{n,Op-Amp}$	$22nV/\sqrt{Hz}$
	$K_{1/f}$	$60nV^2$
	$K_{fold,mod}$	$2.7nV/\sqrt{Hz}$
	$v_{n2,n5}$	Not available (taken as 0)
CMOS Controller	$v_{n,Op-Amp}$	$10nV/\sqrt{Hz}$
	$K_{1/f}$	$800nV^2$
	$K_{fold,mod}$	2.9
Sensor	m_S	$8.34 \cdot 10^{-8}kg$
	ω_S	$13000 \cdot 2\pi = 82000rad/sec$
	Q_S	3000

Using the values in Table 4.4, total output noise densities are expressed in Table 4.6. Output noise is important, but the input referred noise values express the minimum detectable signals.

Table 4.4: Noise densities.

System Portion	Feedback Factor	Values
Front-end Electronics+Sensor	$K_{V/F}$	$16\mu N/V$
	K_G	290
	$\Delta\omega$	$300Hz \cdot 2\pi$
Discrete Electronics	K_{LPF}	6.5
	K_{dmod}	$8/\pi$
	K_{mod}	$8/\pi$
Discrete Electronics	K_{LPF}	1
	K_{dmod}	$4/\pi$
	K_{mod}	$4/\pi$

Table 4.5: Noise densities and feedback factors for each individual noise sources.

System Portion	Noise Densities	Values	β_i
Discrete Electronics Electronics	v_{n1}	$1.97\mu V/\sqrt{Hz}$	0.4
	v_{n2}	0	0.4
	v_{n3}	$60nV/\sqrt{f}$	1
	v_{n4}	$60nV/\sqrt{f}$	6.5
	$v_{n5,white}$	0	1
	$v_{n5,1/f}$	0	1
CMOS Controller	v_{n1}	$1.97\mu V/\sqrt{Hz}$	0.4
	v_{n2}	$630nV/\sqrt{f}$	0.4
	v_{n3}	$800nV/\sqrt{f}$	0.510
	v_{n4}	$1.4\mu V/\sqrt{f}$	0.510
	$v_{n5,white}$	$10nV/\sqrt{Hz}$	1
	$v_{n5,1/f}$	$800nV/\sqrt{f}$	1
Sensor	F_{n6}	$200fN/\sqrt{Hz}$	62500

For that reason, rate-equivalent input referred noises are needed to be found to determine the minimum detectable signals. Signal gain from rate to output, which is called *scale factor*, in closed-loop system is expressed in Eq. 4.36.

$$\begin{aligned} V_{out} &= F_{Coriolis} \cdot \frac{1}{\beta_6} \\ F_{Coriolis} &= \Omega \cdot 2X_D \cdot m_{PM} \cdot \omega_D \\ SF = \frac{V_{out}}{\Omega} &= \frac{2X_D \cdot m_{PM} \cdot \omega_D}{K_{V/F}} \end{aligned} \tag{4.36}$$

Rate equivalent input referred noise can be found by dividing the output noise with scale factor. The overall procedure for finding out the input referred noise can also be visualized in

Table 4.6: Output voltage noise densities.

Controller Electronics	Output Noise Densities	Values
Discrete Electronics	$v_{out,total,white}$	$5\mu/\sqrt{Hz}$
	$v_{out,total,1/f}$	$60nV/\sqrt{f}$
CMOS Electronics	$v_{out,total,white}$	$5\mu/\sqrt{Hz}$
	$v_{out,total,1/f}$	$3.6\mu V/\sqrt{f}$

Figure 4.11. It is a robust parameter in the closed-loop which directly depends on mechanical features of the sensor and proof mass voltage affecting the voltage-to-force conversion. The scale factor for the current sensors for 10V proof mass voltages is around $7.5mV/°/sec$. This value corresponds to $2.1\mu V/°/hour$. Resultant input referred noise is same as the open-loop noise values. This can be seen by investigating the resultant expressions shown Table 4.2. In Chapter 1, relations between the Flicker noise constant and the bias instability (BI); the white noise density and the angle random walk (ARW) are given. These relations are given in the following equations:

$$\text{BI} = \text{Flicker Noise Density Constant} \cdot \overbrace{\sqrt{2 \cdot ln(2)}}^{1.18} \tag{4.37}$$

$$\text{ARW} = \text{White Noise Density} \cdot \underbrace{\sqrt{0.5}}_{0.71} \tag{4.38}$$

Table 4.7 gives rate-equivalent noise values. Table 4.7 shows rate-equivalent noise densities and Allan deviations. It is observed that angle random walk is the same for the controller implementation for both CMOS and discrete electronics. In fact, this reason is the dominant behavior of the front-end electronics. Its contribution can be decreased either by using lower noise Op-Amps and decreasing mismatch. Later work increases the feedback factor, which reduces the noise gain for front-end electronics. Mismatch can be lowered up to approximately

Table 4.7: Rate-equivalent input referred noise densities and Allan Deviations.

Controller Electronics	Output Noise Densities	Values	Allan Deviations
Discrete Electronics	$\Omega_{in,total,white}$	$2.5°/hr/\sqrt{Hz}$	$ARW = 0.03°/\sqrt{hour}$
	$\Omega_{out,total,1/f}$	$28.8m°/hr/\sqrt{f}$	$BI = 0.034°/hour$
CMOS Electronics	$\Omega_{out,total,white}$	$2.5°/hr/\sqrt{Hz}$	$ARW = 0.03°/\sqrt{hour}$
	$\Omega_{out,total,1/f}$	$1.7°/hr/\sqrt{f}$	$BI = 2°/hour$

100Hz, if PID controller design procedure is applied. In that case, noise shaping of the sense mode resonator becomes dominant. This changes the above analysis in a certain amount. In addition, in CMOS low noise Op-Amp design is a straightforward work and CMOS provides a lot of advantageous in low noise CMOS Op-Amp design. 1) Input referred voltage noise can be decreased by increasing dissipated DC current and increasing the transistor dimensions. The most dominant transistor with respect to their noise contributions are input transistors. On the other hand, increasing their dimension increases input capacitance which results in increasing noise gain. An optimization can be performed in order to obtain the best dimensions. 2) If no-protection diode is used in the sense-mode, there will be no noise current of the Op-Amp. Protection diodes prevent unrecoverable damages due to the contact of the proof mass voltage and the preamplifier input. This is a serious problem in drive mode, but it is less probable in sense mode.

In contrary to the advantageous of CMOS implementation for angle random, bias instability significantly suffers from high Flicker noise owing to inherent high 1/f noise of CMOS Op-Amps. In addition, offset drifts also affects bias instability in a considerable amount. Effect of these noise sources can also be suppressed by increasing transistor areas. In addition, offset cancellation techniques can be used which will enhance the bias instability in a substantial amount. In bias instability, sensor drifts also take role but its contribution significantly decreases with quadrature nulling [3].

Voltage densities give valuable information for the selection/design of ADC constituting back-end electronics. Integrating the white noise and Flicker noise densities in between 0.1Hz and 100Hz band gives approximately $25\mu V_{rms}$ noise. For 3.3V CMOS process, it corresponds to 17-bit dynamic range. The best candidate for such a dynamic range for 100Hz bandwidth is Sigma-Delta type ADC as it was mentioned in Chapter 1. In addition, implementation of such an ADC is simple in CMOS.

4.4 Secondary Noise Sources

Dominant noise sources are discussed in details for closed-loop sense mode. On the other hand, there are secondary noise sources which significantly decrease the performance of the gyroscope if they are completely ignored in the design procedure. These noise sources are mainly phase noise, noise of the proof mass voltage, and noise of the electronic reference voltage.

4.4.1 Phase Noise

In the sense mode, it is assumed that there is a perfect phase-sensitive demodulation. Nevertheless, there are always a certain amount of error between the carrier and input signal. These errors can be both deterministic and stochastic. The latter term is nothing but a phase noise. Assuming that, the carrier signal is a pure sinusoidal signal having a phase noise ϕ_n with respect to the input signal. Then, mathematical expressions of the input and the carrier signal can be written as the followings:

$$c(t) = \text{Carrier Signal} = cos(\omega_D t + \phi_n) \tag{4.39}$$

$$x(t) = \text{Input Signal} = r(t) \cdot cos(\omega_D t) + q(t) \cdot sin(\omega_D t) \tag{4.40}$$

where, $r(t)$ is the rate signal, and $q(t)$ is the quadrature signal.

$$\begin{aligned} y(t) &= \text{Output Signal} = (c(t) \cdot x(t)) * f(t) \\ &= \frac{1}{2}(r(t) \cdot (cos(2\omega_D t + \phi_n) + cos(\phi_n)) + q(t) \cdot (sin(2\omega_D t + \phi_n) - sin(\phi_n))) * f(t) \end{aligned} \tag{4.41}$$

where, $f(t)$ is the impulse response function of the low pass filter. In the above equation, high frequency signals are suppressed by the low-pass filter. Therefore, output takes the following form.

$$y(t) = r(t) \cdot \frac{cos(\phi_n)}{2} - q(t) \cdot \frac{sin(\phi_n)}{2} \tag{4.42}$$

Using Taylor's series expansion, output can be expressed as:

$$y(t) = r(t) \cdot \frac{1}{2} - r(t) \cdot \frac{\phi_n^2}{2} + q(t) \cdot \frac{\phi_n}{2} \tag{4.43}$$

First term in Eq. 4.43 is the desired rate dependent signal. Latter terms are noise components due to the phase noise. This part is expressed in Eq. 4.45.

$$y_n(t) = -r(t) \cdot \frac{\phi_n^2}{2} + q(t) \cdot \frac{\phi_n}{2} \tag{4.44}$$

This noise source can be incorporated into the v_{n2} in Figure 4.8 which is the effective input referred noise of the demodulator. In the above analysis, demodulator gain is taken as unity, but whatever the demodulator gain, input referred noise value will be the same. Correspondingly, above equation can be written as:

$$V_{dmod,in,n}(t) = -r(t) \cdot \frac{\phi_n^2}{2} + q(t) \cdot \frac{\phi_n}{2} \tag{4.45}$$

In addition, affect of the deterministic phase error can be investigated using the same relation in Eq. 4.45. In this case, it is seen that there will be offset due to the phase error and quadrature signal. Therefore, if it drifts, output also drifts will worsen bias instability.

In Eq. 4.45, it is clear that noise is mixed with rate signal and quadrature signal. Former is a weak signal, since rate signal is multiplied with square of the phase noise. If phase noise is not dramatically high, then this portion can be neglected. In fact, for zero rate, this term is completely negligible, assuming that there is no electrical offset in the system. On the other hand, it is seen that phase noise directly multiplies with the quadrature signal. This fact tells that the quadrature signal does not only cause drifts at the output, but also increases the effect of the phase noise at the output. This is why the quadrature cancellation improves angle random walk [3]. So, if quadrature signal is minimized with an initial calibration or a real time cancellation, effect of the phase noise of the demodulator can be canceled.

In the above analysis, effect of the phase noise at the demodulator is investigated. Similarly, phase-noise of the modulator is also important. In fact, it is very critical, since noise gain of the modulator is unity and it cannot be improved by decreasing mismatch. Again assume that the carrier signal is pure sinusoidal. Therefore, output the modulator can be expressed as followings:

$$V_{out,mod} = V_{in} \cdot cos(\omega_D t + \phi_n) = V_{in} \cdot cos(\omega_D t) \cdot cos(\phi_n) - V_{in} \cdot sin(\omega_D t) \cdot sin(\phi_n) \tag{4.46}$$

Using the Taylor's series expansion, above expression can be written as followings:

$$\begin{aligned} V_{out,mod} &= V_{in} \cdot cos(\omega_D t + \phi_n) \\ &= V_{in} \cdot cos(\omega_D t) - V_{in} \cdot cos(\omega_D t)\frac{\phi_n^2}{2} - V_{in} \cdot sin(\omega_D t) \cdot \phi_n \end{aligned} \tag{4.47}$$

First term in Eq. 4.47 is nothing but an offset. Second term is very low unless phase noise is very large. The most effective noise component is the final value. In this expression, it is seen that if there is no input coming from the controller output, there will be noise. On the other hand, if there are some offsets, then the noise increases with increasing offset. Fortunately, this term is also filtered in the loop because of the phase sensitive demodulation, but because of the phase errors, a portion of this noise contributes to the output noise. The effective phase noise of the modulator can be found easily by multiplying the third term in Eq. 4.47 with the carrier of the demodulator including a phase error, ϕ_e. This result can also be reached by finding out the effect of the phase noise of the modulator at the modulator input and then dividing the resultant value with the gain between the modulator and demodulator output. In the first step, the output noise equals to the multiplication of the input phase noise of the modulator with the carrier of the demodulator and the gain used in the second step. For this reason, gains cancel each other in these both two steps.

$$V_{mod,in,n} = V_{in} \cdot \phi_n \cdot \phi_e \tag{4.48}$$

Phase error is includes both offset (ϕ_{off}) and random error ($\phi_{n,dmod}$). The random error in demodulator and phase noise are correlated, and in a typical case they are expected to be equal to each other. Therefore, the above equation can also be written as followings:

$$V_{mod,in,n} = V_{in} \cdot \phi_n \cdot \phi_{off} + V_{in} \cdot \phi_n \cdot \phi_{n,dmod} \tag{4.49}$$

Second term in Eq. 4.49 is very low comparing with the first term. Consequently, Eq.4.49 is simpified to Eq. 4.50.

$$V_{mod,in,n} = V_{in} \cdot \phi_n \cdot \phi_{off} \tag{4.50}$$

This result expresses that two non-ideal behavior of the sense mode system increases the effect of the phase noise at the output in a considerable amount. These non-ideal behaviors are DC errors in the sense mode system and phase error at the demodulator. Therefore, in CMOS designs blocks operating at DC should have a very low DC offsets, and phase errors should be minimized. Furthermore, it is very obvious that phase errors should be under control by using a PLL based actuation for the optimum performance.

Finally, in the controller designs phase of the demodulator is determined for the mismatched case. However, decreasing the mismatch amount will increase the phase error, therefore increase the effect of the modulator phase noise. This conflicts with the result which tells that decreasing mismatch improves the overall system performance. Unfortunately, input referred phase noise cannot be improved by decreasing mismatch, because of the its unity noise gain as expressed above. For this reason, for a high performance system phase noise and DC offsets should be minimized, since there is always a phase error for low mis-match amount which is necessary to reduce noise contribution of other electronics.

4.4.2 Noise of the Proof Mass Voltage and Analog Reference Voltage

Noise of the proof mass voltage affects the system noise from two paths: 1) Electrical coupling from the static capacitance between the proof mass and sense electrode. 2) Electro-mechanical coupling due to the effect of the proof mass voltages on the voltage-to-force and displacement-to-current processes.

Electrical coupling is due to the electrical path through the static capacitance between sense electrode and proof mass. The effect of this noise can be written as in the following equation.

$$V_{preamp,out} = V_{PM,n} \cdot \frac{C_{static}}{C_{int}} \tag{4.51}$$

where, C_{int} is the integration capacitance of the preamplifier, and C_{static} is the static capacitance between the proof mass and the sense node. In sense mode, there is differential reading; therefore, output of the preamplifier can be written as followings:

$$V_{ins-amp,out} = V_{PM,n} \cdot \frac{\Delta C_{static}}{C_{int}} \tag{4.52}$$

where, K_ins is the gain of the instrumentation amplifier, and ΔC_{static} is the mismatch amount of the static capacitances for the two sense electrodes. Eq. 4.52 shows that effect of the proof mass noise is zero if the static capacitance is matched perfectly. Moreover, proof mass voltage can be filtered with a simple low pass filter. Since, the band of interest in the front-end electronics is around the carrier frequencies, filter will remove the noise in the band of interest. Here, the important result is that electrical coupling is almost insensitive to the drifts of the supply.

Electro-mechanical coupling is the second path between the proof mass noise and gyroscope output. Output of the gyroscope is composed of the rate and quadrature terms. Rate and output relation is determined by the closed-loop dynamics, but quadrature and output relation is determined by the open-loop dynamics. The reason is that loop-gain is very low for quadrature signal due to the phase sensitive demodulation. Therefore, output of the sense mode system can be written as:

$$V_{out} = \Omega \cdot K_{\Omega/F} \cdot \frac{1}{K_{V/F}} + F_Q \cdot K_{F/x} \cdot K_{x/I} \cdot \alpha \tag{4.53}$$

where, α is the inverse of the feedback factor between the sensor output and controller output of the sense mode. In the above equation, voltage-to-force constant and displacement-to-current scalars are proportional to the proof mass voltage. Besides, rate-to-force constant

$K_{\Omega/F}$ and F_Q depends on the drive mode displacement. In drive mode dynamics it is shown that drive mode displacement is inversely proportional to the displacement-to-current conversion gain which is proportional to the proof mass voltage. As a result, 4.53 can be written as followings in terms of the proof mass voltage:

$$V_{out} = \frac{\Omega \cdot a_1}{V_{PM}^2} + k_Q \cdot a_2 \tag{4.54}$$

In Eq. 4.54, k_Q is the scalar indicating the relation between the force and drive mode displacement. Eq. 4.54 shows that proof mass noise only mixed with the rate. Therefore, if there is no rate, proof mass noise cannot be coupled to the output due to this electro-mechanical path. By writing proof mass voltage in terms of a constant bias and small signal deviation, output noise can be written as:

$$V_{out,VPMn} = \frac{\Omega \cdot a_1}{(V_{PM0} + V_{PM,n})^2} = \frac{\Omega \cdot a_1}{V_{PM0^2} \cdot \left(1 + \frac{V_{PM,n}}{V_{PM0}}\right)^2} \tag{4.55}$$

Using Taylor's series expansion above expression can be written as:

$$V_{out,VPMn} = \frac{\Omega \cdot 2 \cdot a_1}{V_{PM0}^3} \cdot V_{PM,n} \tag{4.56}$$

If there is no electrical offset, this noise is zero. If there is an offset, this will increase the effect of this noise source. The important point in the above equation is that this path is sensitive to the drifts of the proof mass voltages which cannot be filtered with low pass filter in contrary to the electrical path.

If single supply is wanted to use in the gyroscope system, reference voltage of the analog blocks (i.e., non-inverting terminal of the preamplifier, reference terminal of the instrumentation amplifier), cannot be grounded. Therefore, noise of the voltage feeding these reference terminals directly affect the output. In most of the blocks, this noise has the same gain as the input referred voltage noise of the Op-Amps. In order to have a good performance, reference generator, which is typically a band-gap reference, should be low-noise. Besides, its noise should be filtered. Therefore, its affect for the blocks operating at higher frequencies can be suppressed. It will decrease the overall noise contribution coming from the reference voltage generator in a significant amount, since filter especially decreases the effect of this noise source on the front-end electronics.

4.5 Summary

The controller implementation with CMOS electronics miniaturizes the complete system. It is observed that CMOS electronics can reach the angle random walk performance of the discrete electronics. On the other hand, in order to improve the bias instability, offset and the Flicker noise cancellation techniques can be used to eliminate the Flicker noise contributions, and offset drifts. In addition, the noise folding of the switching demodulator increases the effective white noise density of the overall system in a substantial amount. Finally, it is shown that DC offsets in the sense mode increases the effect of the phase noise which contributes to the angle random walk and the bias instability.

CHAPTER 5

TEST RESULTS

This chapter presents the test results of a complete gyroscope system including the drive and sense mode controllers. Proposed analytical design procedures are verified with test results. Section 6.1 describes the system set-up. Section 6.2 gives test results of the two type of the drive mode controllers implemented in the CMOS technology: the conventional system with the improved controller design procedure and the new generation simplified drive mode controller. Section 6.3 gives test results verifying the accuracy of the proposed base-band equivalent model for the mismatch operation. In addition, it also includes test results showing the importance of the accurate controller design on the system performance. Section 6.4 verifies the operation of the CMOS system, and gives performance results for the open-loop and the closed-loop configuration. Section 6.5 concludes this chapter.

5.1 System Setup

The tests of MEMS gyroscopes include two major steps: scale factor test, and noise test. A scale factor test is needed to determine the gyroscope responsivity, linearity and range. Second test gives information about minimum detectable angle rate levels for different integration times. These results also give information about the noise densities. Output noise values are divided by the scale factor in order to refer the output noise to the input, .

The controllers are implemented with the discrete electronics and the CMOS electronics. Figure 5.1 shows the die photograph of the CMOS chip including drive and sense mode controllers. The new generation simplified controller is used in the performance tests, because of its simplicity. A PCB has been designed combining the CMOS electronics and the sensor module which is a vacuumed packaged including the preamplifier and the second gain stage. In addition, this PCB also includes a voltage regulator, output buffer and quadrature nulling Op-Amps. The Last circuitry inverts the DC potential for the quadrature calibration, since the quadrature nulling requires two voltages having opposite polarities [3]. This part only minimizes the quadrature signal: it does not carry out dynamic quadrature cancellation with a feedback loop. Though, the CMOS chip includes both the drive and sense systems, two CMOS chips are used for each control. One of the controller for each chip is blocked. The reason is to isolate these systems: if one of them fails, the other one can continue its operation. This is practical for such a prototype work. Figure 5.2 shows the PCB photograph.

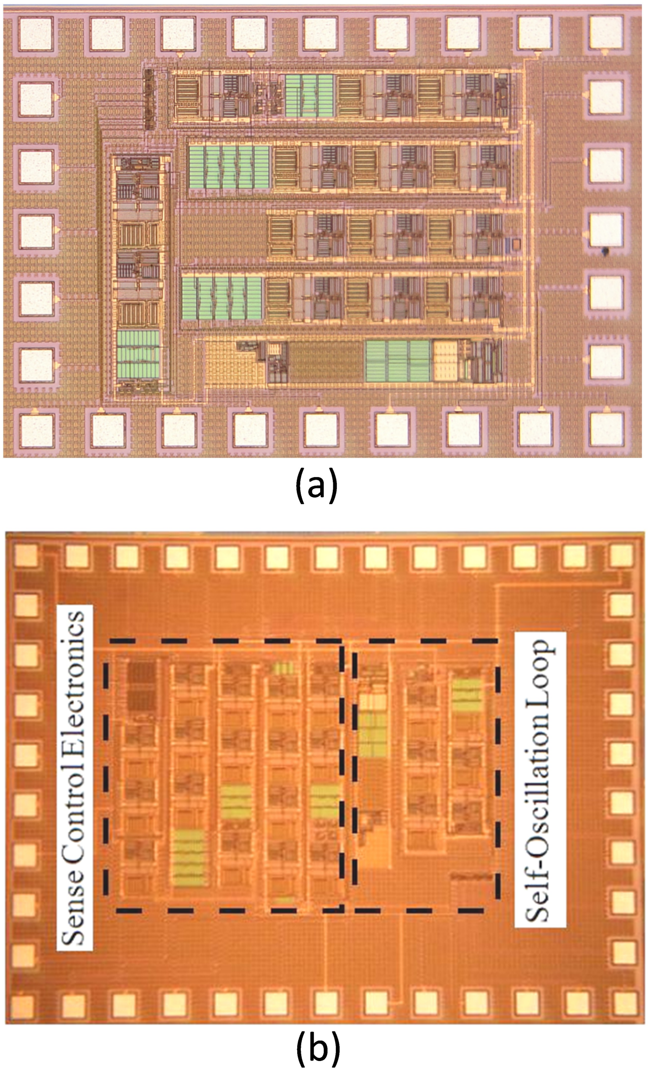

Figure 5.1: Photograph of the CMOS chips (a) conventional drive mode controller (b) new generation drive mode controller and sense mode controller.

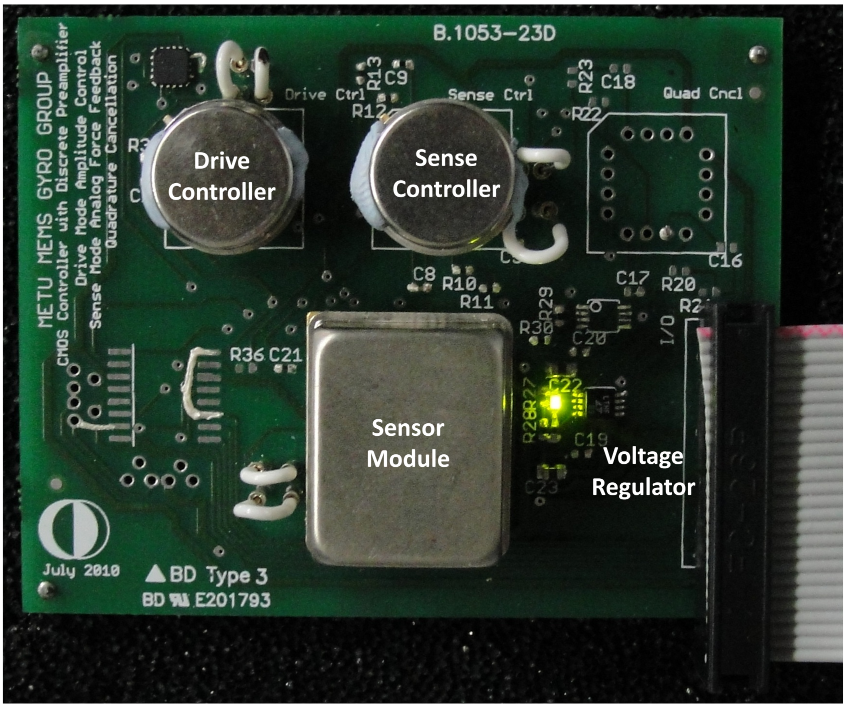

Figure 5.2: Photograph of the PCB.

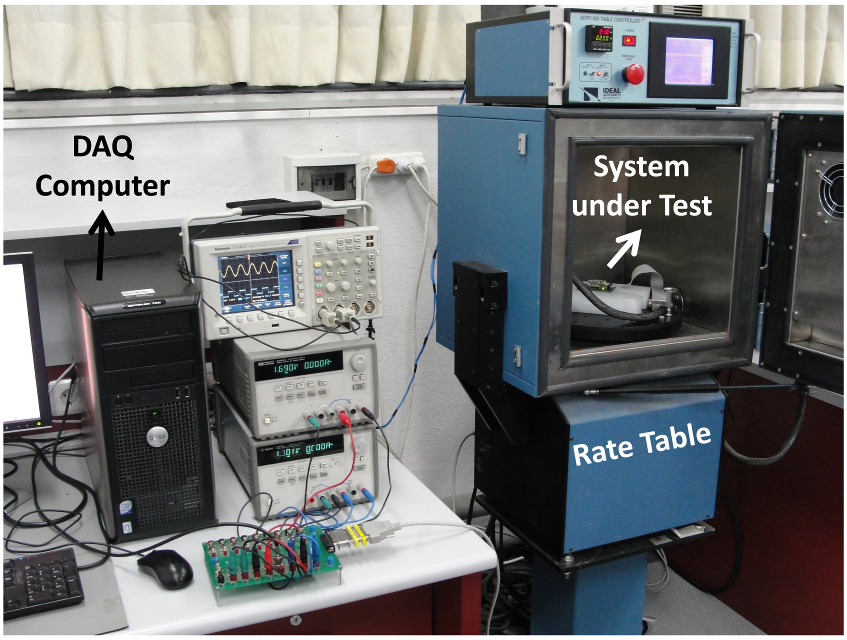

Figure 5.3: Photograph of the set-up.

Figure 5.3 shows the system set-up. Test set-up is composed of two voltage supplies, an oscilloscope, a rate table, and a computer including data acquisition (DAQ) card. Two supplies are necessary to set the drive mode oscillation amplitude, the quadrature calibration, and the DC supplies of the system. The scale factor tests are performed with the rate table with which sensor responsivity is measured. A control of the rate table is conducted with the computer. This computer is also used for the acquisition of the analog output coming from the gyroscope.

5.2 Drive Mode Controller Test Results

The classic drive mode controller has been optimized according to its non-linear settling and LTI steady-state characteristics. Test results of the optimization of the classic drive mode controller has been performed with the system implemented with discrete electronics. Figure 5.4 shows settling of the classic drive mode controller.

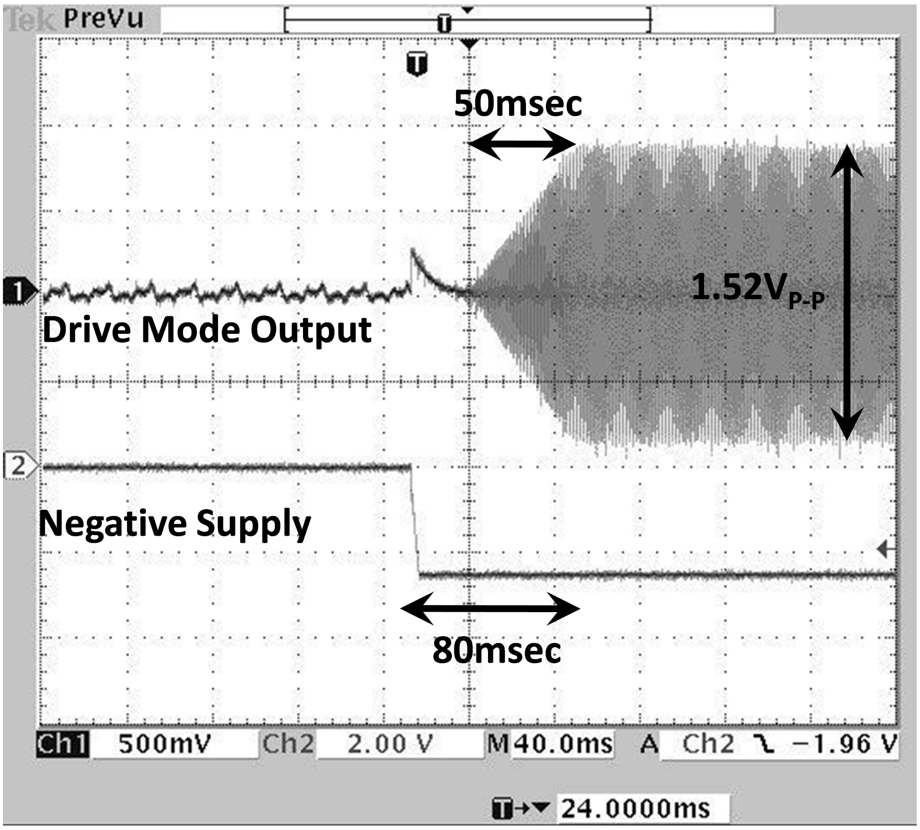

Figure 5.4: Settling of the conventional drive mode controller with the new design controller approach.

The settling of the system is approximately 50 msec which is completely consistent with the simulation result. In previous works, the best value is around 100 msec [3]. In fact, LTI optimization, discussed in Chapter 2, is applied to this system. In previous works, the settling time even exceeds a few seconds with a considerable overshoot. The sensor model used in the simulation is different than the device under test, but controller parameters are updated according to the design procedure discussed in Chapter 2. There are two signals in Figure 5.4. The below signal is used for triggering the drive mode settling. This triggering signal is the negative supply of the CMOS chips. Note that there is a delay between system-power-up and start-up of the self-oscillation. This is due to the settling of the complete system including the external electronics. In addition to the external electronics, limited start-up time of the DC supplies contributes this delay. The peak-to-peak voltage measured in this test corresponds to approximately a 4μm drive mode oscillation amplitude.

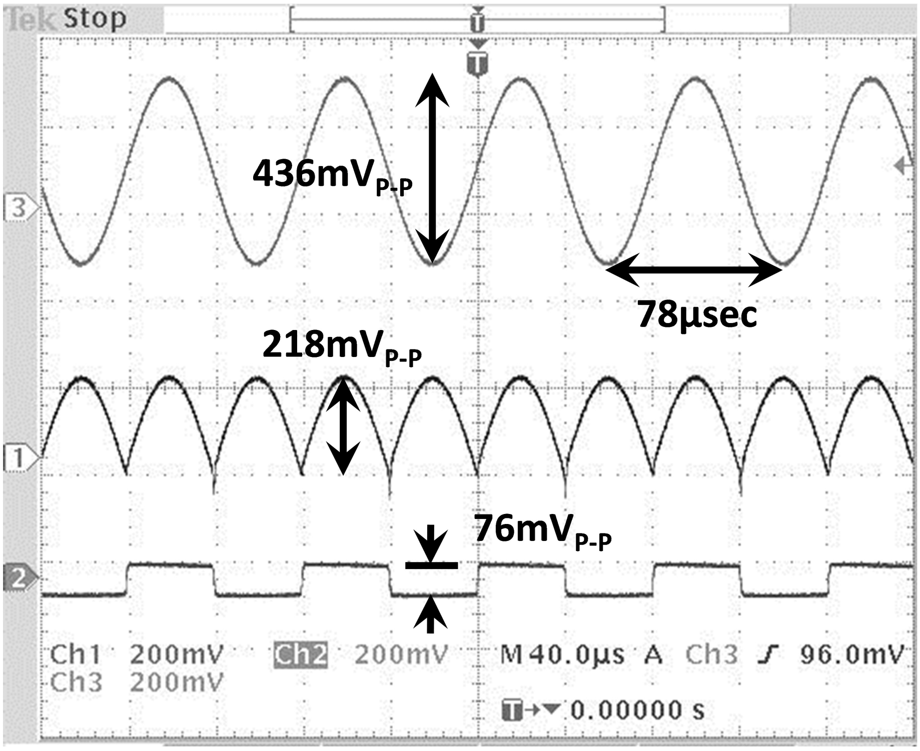

Figure 5.5: Steady state signals of the conventional drive mode controller.

Figure 5.5 verifies the functionality of the conventional CMOS controller. There are three signals on the oscilloscope screen. First waveform is the demodulator input which is nothing but the sensor module output: output of the secondary gain stage. Second waveform is the demodulator output. The carrier and message inputs of this demodulator are same, so observed output is a rectified signal. Third waveform shows the feedback voltage actuating the sensor. Ratio between the sensor module output and first harmonic of the actuating voltage gives the resonance gain of the corresponding sensor module. It is almost equal to the 14dB which is the typical measured gains for the current designs with 10V proof mass voltage which is the case in this test.

In this design, offset calibrations are necessary because of the unexpected offsets coming from the Op-Amps used from the XFAB library. Firstly, the demodulator input cannot be rectified properly if the incoming signal from the sensor module has no DC. For this reason, loop gain decreases due to the reduction of the conversion gain between the amplitude to the DC in the demodulator. An offset is given to that incoming signal with a simple RC network which directly couples the AC signal to the demodulator input in order to obtain a perfect full-wave rectified signal. Secondly, the negative saturation level of the Op-Amps used in the CMOS chips is around -1.5V which is bigger than the reference level (-1.55V). Accordingly, this part does not work properly at the steady state, since the low pass filter cannot give the desired steady state voltage which equals to the reference level, and it enters saturation resulting in the breaking of the feedback. In order to solve this problem, an offset is given to the output of the instrumentation amplifier. This offset decreases the targeted steady state value of the low pass filter output, so it can operate perfectly. In fact, the reference value is also buffered with an Op-Amp; therefore, the buffer Op-Amp also enters the saturation region, and it cannot give the reference value: its output is the negative saturation level. Fortunately, this does not yield a functionality problem.

Figure 5.6 shows the steady state signals of the new generation drive mode controller. The square wave signal comes from the positive feedback and the sinusoidal signal is the negative feedback output. Latter signal should equal to the first harmonic of the former signal. Due to the delays of the system, there is an error, but it is still fair for the drive mode regulation. The regulation strength can be increased by sacrificing the drive mode oscillation amplitude.

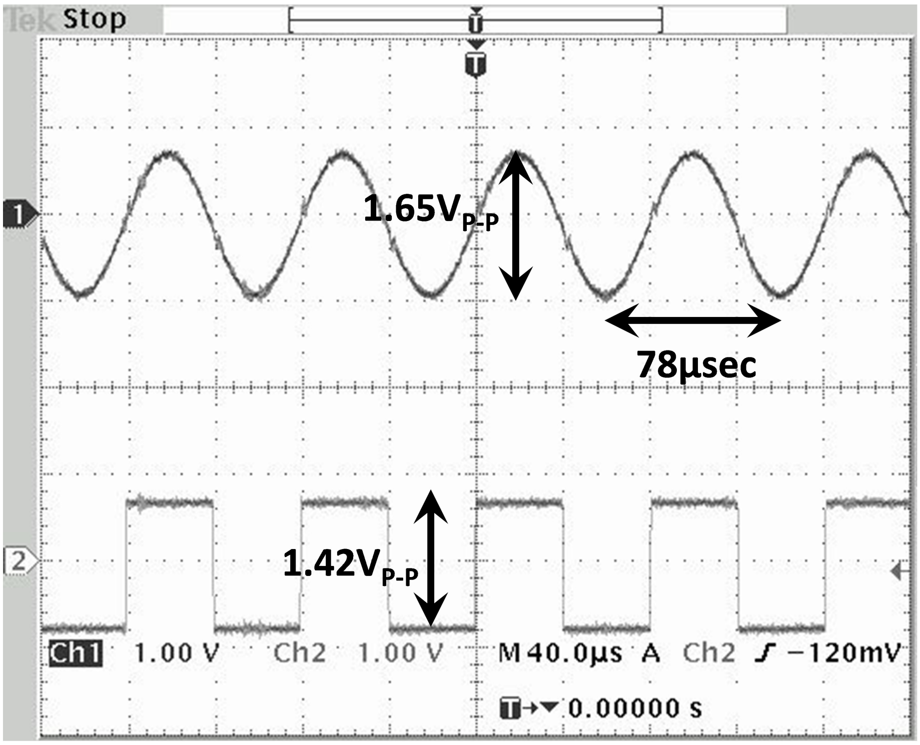

Figure 5.6: Steady state signals of new generation simplified drive mode controller.

Figure 5.7 shows the settling of the new generation drive mode system. Because of the low loop gain, the settling time is around 300 msec. On the other hand, as Figure 5.8 shows this amount can further be improved up to 27 msec. The first conventional drive mode system with the new controller design approach, settling performance of this system is much better than the new generation simplified drive mode controller for large displacements. On the other hand, the second system is much simpler than the former one, and it can be used in several applications. In fact, its settling time is still much lower than the settling time reported in previous works [2, 25].

5.3 Sense Mode Controller Test Results

Accuracy of the sense mode base-band equivalent models is verified by investigating the stability limit of the closed-loop system. Stability limits are found firstly in the simulations of the closed-loop system which are constructed with complete model, base-band equivalent model, and simplified base-band equivalent model which only includes the gain characteristics of the

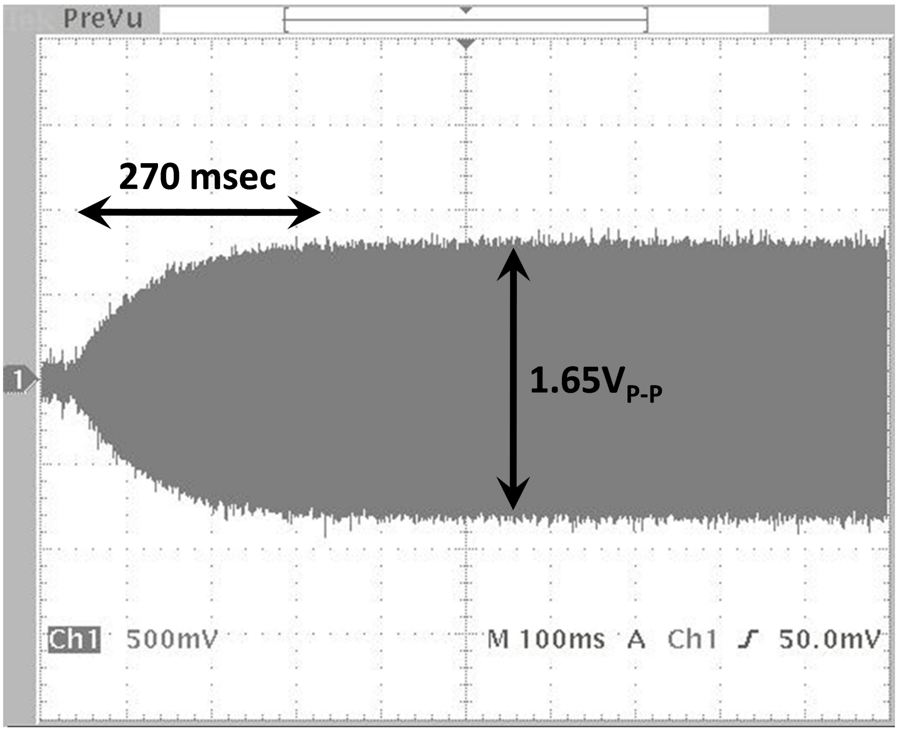

Figure 5.7: Settling of new generation simplified drive mode controller.

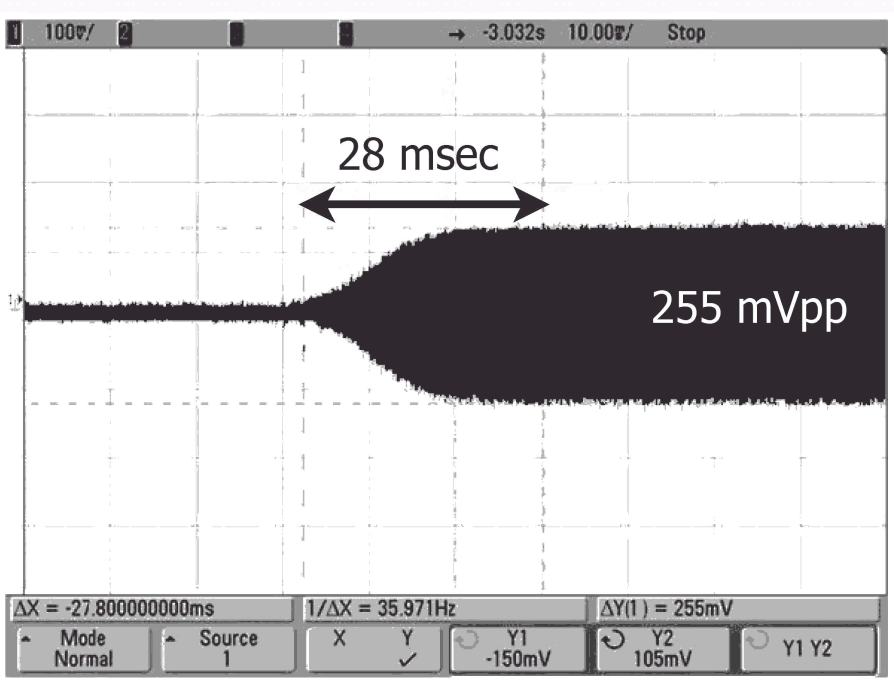

Figure 5.8: Settling of new generation simplified drive mode controller with larger loop gain.

sense mode. A pure integrator is used as a controller. Table 5.1 shows the controller values for which the system is stable. If the controller value exceeds this limit, system has a sustain oscillation. The gain for this oscillation corresponds to the stability limit.

Table 5.1: Comparison of predicted stability region for over-simplified and new baseband models, and the measured stable region of the actual system.

Integrator Gain		
Predicted by Over-Simplified Model	Predicted by Over-Simplified Model	Measured
<8.7	<2.9	<2.8

Table 5.1 shows that the base-band equivalent model has high accuracy. It is seen that this model can safely be used in real systems. On the other hand, ignoring frequency dependent characteristics causes significant problems in terms of the stability. Even if the system is stable, there is a significant deviation in the transient performance of the system and bandwidth.

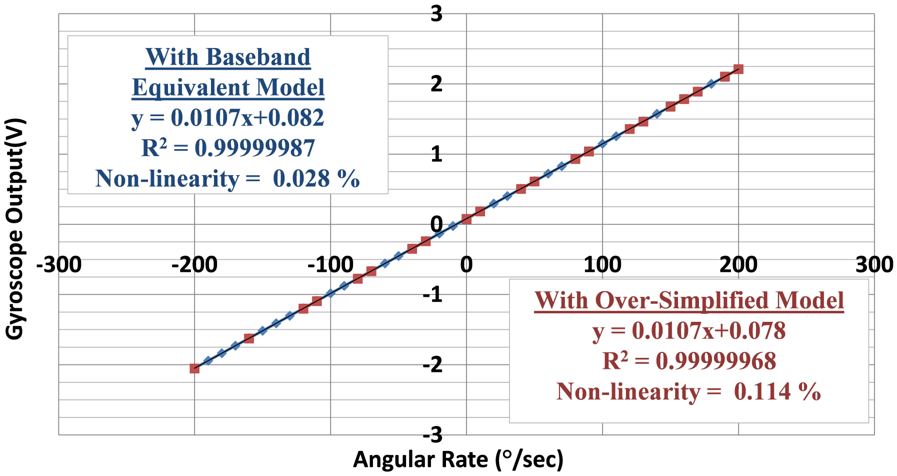

Figure 5.9: Measured angular rate response and non-linearity of a MEMS gyroscope with controllers based on over-simplified.

In addition, the operation at the stability limit also results in substantial performance degradation. Figure 5.9 and 5.10 present the measured angular rate response, linearity, and noise performance of the gyroscope when operated with different controller parameters using both the over-simplified and new baseband models. Design basing on the simplified-model causes an operation near to the stability limit. It is observed that linearity, angle random walk, and bias instability performance improves by factors of 4, 9 and 3, respectively, for the system designed with the new baseband model, verifying the improvement with the proposed model.

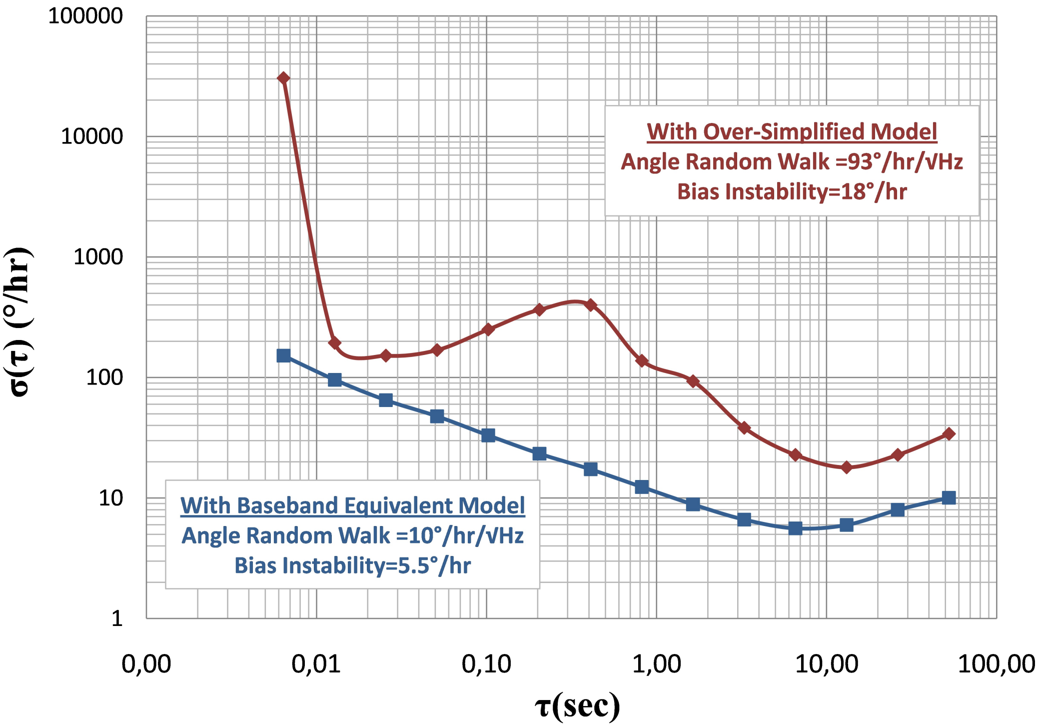

Figure 5.10: Measured noise performance of a MEMS gyroscope with controllers based on over-simplified and baseband equivalent models.

5.4 Performance Results obtained with CMOS chip

Both open-loop and closed-loop operations are performed with the CMOS chip. In the open-loop operation, it is observed that the Flicker noise highly dominates the system response. Flat characteristics of the Allan deviation stem from the Flicker noise. As it was mentioned in Chapter 4, increasing the gain before the Flicker noise sources will directly decreases the effect of these noise sources. This gain increase decreases both the angle random walk and the bias instability from $7.1°/hr/\sqrt{Hz}$ to $2.2°/hr/\sqrt{Hz}$ and $3.3°/hr$ to $3°/hr$, respectively. Figure 5.11 and Figure 5.12 show these results. Second angle random walk is very near to the theoretical limit which is around $2°/hr/\sqrt{Hz}$ for 4μm drive displacement. In these Allan variance curves, the trend of the noise level decreases as τ decreases due to the low pass filter characteristics of the closed-loop sense mode: lower τ corresponds to the high frequency noises, and they are rejected by the closed-loop dynamics.

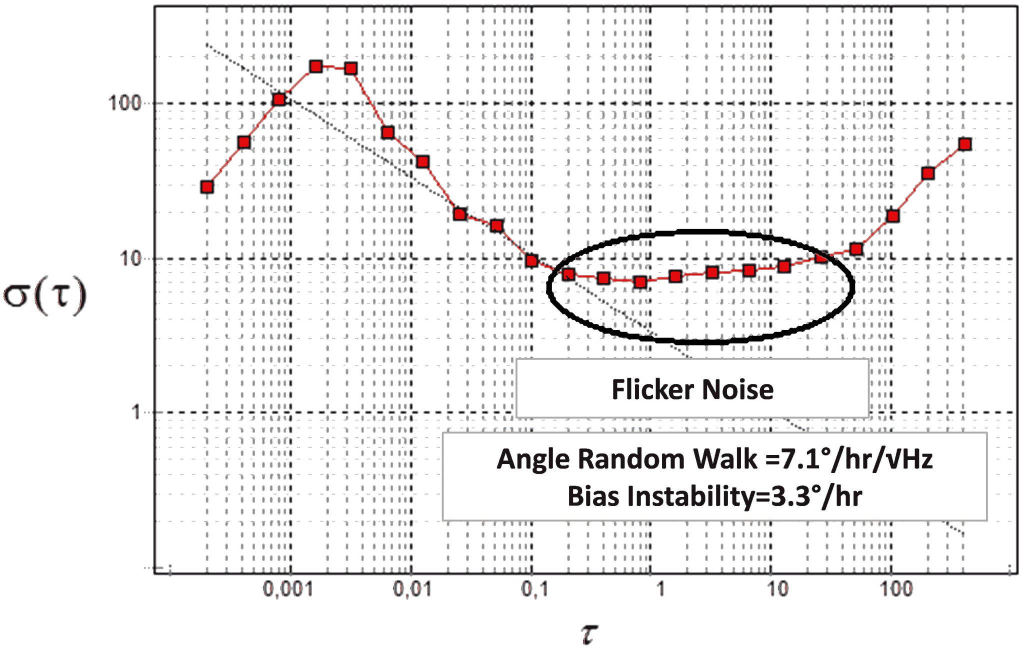

Figure 5.11: Allan Variance plots for open-loop sense mode system with default gains.

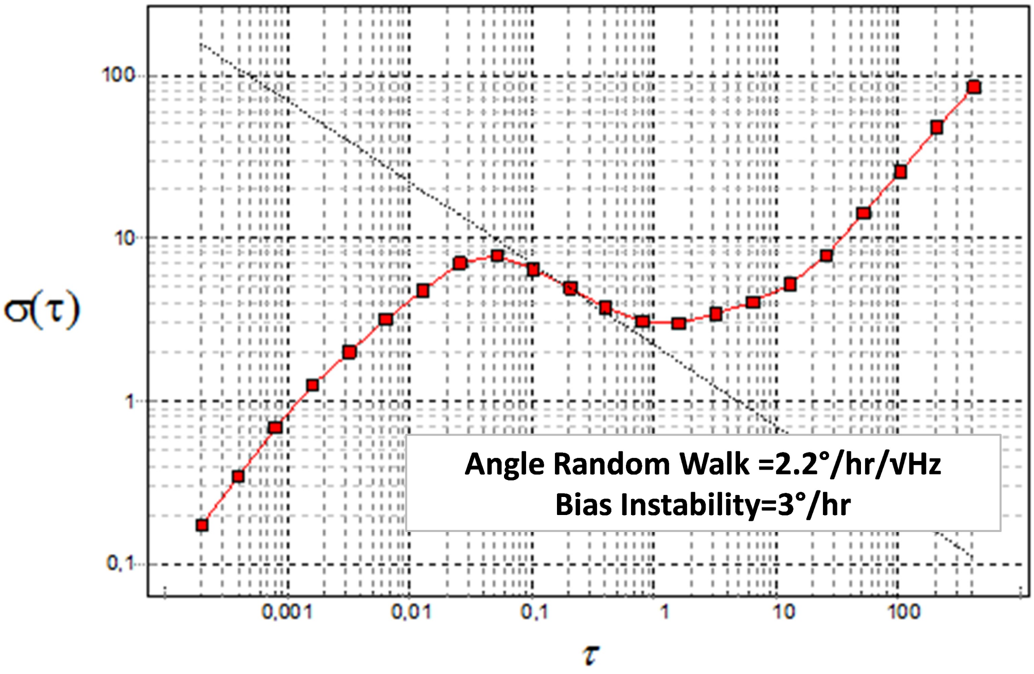

Figure 5.12: Allan Variance plots for open-loop sense mode system with larger gains before demodulator.

In the closed-loop operation, system operates perfectly. It has a robust scale factor which is almost independent from the sensor parameters and ambient conditions. In addition, it is verified that the sense output of the gyro module is almost 0. On the other hand, noise results of closed-lop system deteriorates as Figure 5.13 shows.

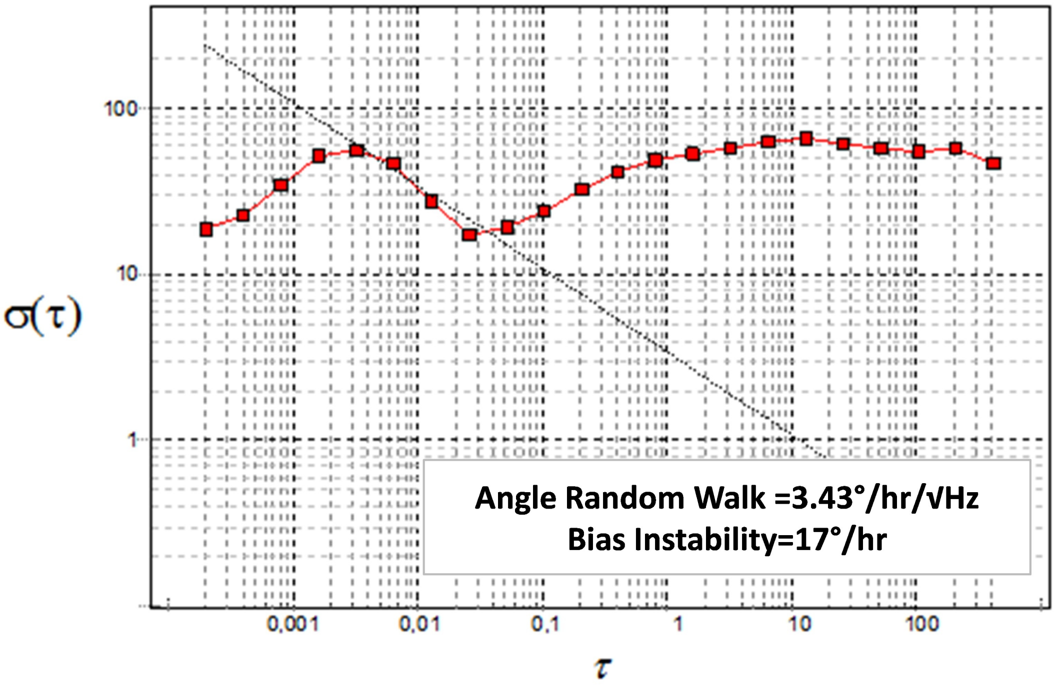

Figure 5.13: Allan Variance plots for closed-loop sense mode system.

In fact, if the feedback network noise is negligible, then noise degradation is not expected. This is observed in the closed-loop systems implemented with discrete electronics. On the other hand, there is a performance degradation in CMOS controllers . The reason is likely to be the extra noise injection coming from the feedback network which is dominated by the modulator noise. In Chapter 4, it is seen that the noise contribution of the modulator is very small comparing with the front-end electronics' noise contribution. In that analysis, secondary noise effects such as phase noise are neglected. On the other hand, analysis of the secondary noise sources show that phase noise of the modulator becomes effective if there is a phase error at the demodulator and DC offset in the modulator input due to the offset of the Op-Amps. In discrete implementation, special Op-Amps (chopper stabilized Op-Amps) are used. Thus, there is no offset in zero rate condition if quadrature force is canceled with an initial calibration, or an on-line cancellation. This is why in discrete implementations, modulator noise is negligible. On the other hand, in the CMOS system there is a significant amount of offset which increases the effect of the phase noise. This fact is also verified by observing the noise performance of the system with decreasing the mismatch. In the closed-loop operation, it is expected that the system performance improves with decreasing the mismatch. On the other hand, if overall noise is dominated by the phase noise of modulator, then it will directly refer to the output. Decreasing mismatch does not suppress the effect of this noise source. In contrary to reduction of noise at the output, it increases in tests. This result is totally consistent with the discussion in Chapter 4: decreasing mismatch amount increases the phase error between the demodulator carrier and incoming signal, so effect of the phase noise at the output increases if there is a DC offset at the modulator input. To conclude, in order to obtain better performance, it is needed to minimize the DC offset and decrease the phase noise by using a PLL.

5.5 Summary

In this chapter, the new control design procedure for the conventional drive mode controller is applied and very good results are obtained. In addition, the base-band equivalent model is verified with the test results by observing the stability limits. The effect of the closed-loop on the linearity is also verified. Importance of the true controller design on the system performance is demonstrated, as well. Finally, the complete CMOS controller is tested, and it is seen that there is an unexpected performance degradation in the closed-loop. It is concluded that the reason for this performance reduction is the phase-noise of the modulator.

CHAPTER 6

CONCLUSION AND FUTURE WORK

This work presents a comprehensive study on the controller design and its implementation in a CMOS technology. Both the drive and sense mode closed-loop systems are discussed in details, and they are optimized for the best settling time and bandwidth. The new base-band equivalent model for the sense mode system is derived, and the controller design procedure is presented. Accomplishments and results of this research can be listed as follows:

1. The detailed system level analysis has been carried out for the drive mode system. Firstly, the drive mode system has been optimized for the settling time. Pole-zero cancellation technique is used for the compensation of the low frequency pole coming from the envelope model. Settling of the drive mode system has been reduced up to 20 msec in the simulations. This value can further be improved by increasing the cut-off frequency of the low pass filter. Nevertheless, increasing the cut-off frequency degrades the filter's suppression of the high harmonics of the drive mode oscillation frequency. In addition, this settling time has been obtained with a 60° phase margin ensuring a robust operation.
2. The circuit imperfections coming from the implementation have been taken into account, and optimization has been done for the settling time. It is observed that there is a significant discrepancy between the simulation results and measured values if drive mode system is forced to have a low settling time. It is concluded that the saturation of the Op-Amp in the PI controller causes this discrepancy. This non-linear behavior of the controller is analyzed, and the transient performance of the drive mode is optimized again. The optimization results show that the proposed design procedure gives also the best solution for the actual drive mode system, but the resultant performance is worse

than the ones obtained with the idealized system. The accuracy of the analysis performed for this non-ideal case has been verified with the test results. 50 msec settling time has been achieved with no overshoot. This result demonstrates the best value in literature among the gyroscopes whose control is carried out by the analog electronics.

3. The new generation drive mode controller topology is introduced. This system promises very high performance in terms of the drive mode transient performance. On the other hand, there is a strict trade-off between the drive mode displacement and settling time.

4. The base-band equivalent model for sense dynamics has been derived. The base-band equivalent model for sense system is, firstly presented in literature, for mismatch operation. The analytical design procedure is developed using this model. This comprehensive study basing on the simple control theories is firstly reported, as well. Two methods are discussed in details: PID controller and integral controller. The former one provides a strong control which can be used in either low or high frequency mismatch amounts. On the other hand, the second controller is effective for high mismatch amounts. It is shown that sense dynamics can be modeled as a simple gain stage if mismatch amount is high enough. The minimum mismatch amount enabling the use of this simple method is analyzed in details. Controller design approaches are verified with the system level simulations.

5. Performance analysis has been conducted for the analog sense mode controller. The noise folding of the modulator and demodulator is firstly presented for these systems. It is seen that this feature of the modulator/demodulators increases the electronic noise power of the system by a factor of 2.5. Minimum attainable angle random walk and bias instability values are found for the controllers implemented with the discrete and CMOS electronics. Secondary noise sources are also investigated. It is observed that the circuit imperfections, such as the DC offsets and phase errors, increase the effect of the phase noise at the output in a substantial amount.

6. The CMOS implementation of the proposed controllers has been carried out. These are the first functional ASIC chips for the MEMS gyroscopes developed at METU. This work provides a low cost and low volume solution for the controller implementation. The open-loop configuration has been resulted in a $2.2^\circ/hr/\sqrt{Hz}$ angle random walk and $3^\circ/hr$ bias instability. Angle random walk result is very close to the theoretical

value. The closed-loop results are also promising for the tactical grade applications, but there is a performance degradation for the closed-loop sense mode system. Reasons for this discrepancy are discussed. It is concluded that the DC offsets considerably increase the effect of the phase noise of the modulator, which is not available in the open-loop system. This extra noise of the modulator increases the noise of the closed-loop system.

Major achievement of this thesis is the development of effective and simple design procedures for the analog control of the MEMS gyroscopes. The analog controller is implemented in a CMOS technology. Functionality of these chips are verified, but there are limitations in their performances. To increase the performance further, some of the future research topics are listed below:

1. A complete gyroscope ASIC should be designed including the front-end electronics, drive mode control, sense mode control, and the quadrature cancellation. Circuits of this new ASIC should be carried out according to the well defined system requirements. In addition, better technology, such as 0.35μm CMOS process should be used for robust and high performance circuits. X-Fab 0.35μm CMOS process has been used for a new preamplifier topology implemented with custom circuit blocks, such as band-gap reference and Op-Amps, instead of available blocks in the library of the IC manufacturer. The first results show that this process is very good in terms matching and robustness. In the new ASIC, circuits operating at the DC band should have offset nullifying property to suppress the Flicker noise, offset drifts, and the effect of the phase noise at the output.

2. The feedback network noise should be minimized by reducing the phase noise of the drive mode system. PLL can be used to reject the phase noise, but this will complicate the design.

3. The analog to digital conversion should be as close as possible to the CMOS system. Firstly, an external ADC should be combined with CMOS electronics. In later works, this ASIC should be integrated with other electronics in a single CMOS chip.

4. A digital control should be performed for a smart system combining several loops. It requires a careful circuit and system level designs, but these systems are today's trend which promise very high performances.

REFERENCES

[1] S. E. Alper, “MEMS Gyroscopes for Tactical-Grade Inertial Measurement Applications,” *Dissertation for the Degree of Doctor of Philosophy*, Middle East Technical University, September 2005.

[2] E. Sahin, “High Performance Readout and Control Electronics for MEMS Gyroscopes,” *M.S. Thesis*, Middle East Technical University, February 2009.

[3] E. Tatar, “Quadrature Error Compensation and Its Effects on the Performance of Fully Decoupled MEMS Gyroscopes,” *M.S. Thesis*, Middle East Techical University, September 2010.

[4] S. Sung, S. Yu, W. T. Sung, C. J. Kim, and Y. J. Lee, “A Novel Control Loop Design and Its Application to the Force Balance of Vibratory Rate Sensor,” *International Jorunal of Control, Automation, and Systems*, Vol.7, pp.545-552, 2009.

[5] S. An, Y. S. Oh, K. Y. Park, S. S. Lee, and C. M. Song, “Dual-axis microgyroscope with closed-loop detection,” *Sensors and Actuators A*, Vol. 73, pp.1-6, 1999.

[6] W. T. Sung, S. Sung, J. G. Lee, and T. Kong, “Design and performance test of a MEMS vibratory gyroscope with a novel AGC force rebalance control,” *Journal of Micromechanics and Microengineering*, pp.1939-1948, 2007.

[7] C. D. Ezewke and B. E. Boser, “A Mode-Matching Sigma-Delta Closed-Loop Vibratory Gyroscope Readout Interface with $0.004°/s/\sqrt{Hz}$ Noise Floor over a 50Hz Band,” *IEEE International Solid-State Circuits Conference (ISSCC 2008)*, pp.580-582, 2008.

[8] J. Raman, E. Cretu, P. Rombouts, and L. Weyten, “A Closed-Loop Digitally Controlled MEMS Gyroscope With Unconstrained Sigma-Delta Force-Feedback,” *IEEE Sensors Journal*, Vol.9, No.3, pp.297-305, 2009.

[9] C. D. Ezewke and B. E. Boser, “A $0.2°/hr$ Micro-Gyroscope with Automatic CMOS Mode Matching,” *IEEE International Solid-State Circuits Conference (ISSCC 2007)*, pp.386-387, 2008.

[10] M. Egretzberger and A. Kugi, “A dynamical envelope model for vibratory gyroscopes,” *Journal of Microsystems Technology*, Vol.16, pp.777-786, 2010.

[11] R. P. Leland, “Adaptive Control of a MEMS Gyroscope Using Lyapunov Methods,” *Journal of IEEE Transactions on Control Systems Technology*, Vol. 14, No. 2, 2006.

[12] J. Cui, X. Z. Chi, H. T. Ding, L. T. Lin, Z. C. Yang, and G. Z. Yan,“Transient response and stability of the AGC-PI closed-loop controlled MEMS vibratory gyroscopes,” *Journal of Micromechanics and Microengineering*, Vol. 19.

[13] N. Yazdi, F. Ayazi, and K. Najafi, “Micromachined Inertial Sensors,” *Proceedings of the IEEE*, Vol.86, No.8, pp.1640-1659, August 1998.

[14] K. Azgin, Y. Temiz, and T. Akin, “An SOI-MEMS Tuning Fork Gyroscope With Linearly Coupled Drive Mechanism,” *The 20th IEEE Int. MicroElectroMechanical Systems Conf. (MEMS 2007)*, pp. 607-610, Kobe, Japan, January 2007.

[15] K. Azgin, “High performance MEMS Gyroscopes,” *M.S. Thesis*, Middle East Techical University, February 2007.

[16] D. Lapadatu, B. Blixhavn, R. Holm, and T. Kvisteroy, “SAR500 - A High-Precision High-Stability Butterfly Gyroscope with North Seeking Capability,” *Position Location and Navigation Symposium (PLANS 2010) 2010*, pp.6-13, Indian Wells, CA, USA, May 2010.

[17] R. R. Ragan and D. D. Lynch, “Inertial technology for the future, Part X: Hemispherical resonator gyro,” *IEEE Trans. Aerosp. Electron. Syst.*, Vol. AES-20, pp. 414-444, 432, 1984.

[18] M. A. Erismis, “MEMS Accelerometers and Gyroscopes for Inertial Measurement Units,” *M.S. Thesis*, Middle East Technical University, September 2004.

[19] A. Sharma, M. F. Zaman, and F. Ayazi, “A Sub-0.2 °/hr Bias Drift Micromechanical Silicon Gyroscope With Automatic CMOS Mode-Matching,” *IEEE Journal of Solid-State Circuits*, Vol. 44, No. 5, pp.1593-1608, 2009.

[20] R. Voss, K. Bauer, W. Ficker, T. Gleissner, W. Kupke, M. Rose, S. Sassen, J. Schalk, H. Seidel, and E. Stenzel, “Silicon Angular Rate Sensor for Automotive Applications with Piezoelectric Drive and Piezoresistive Readout,” *Tech. Dig. 9th Int. Conf. Solid-State Sensors and Actuators (Transducers’97)*, Chicago, IL, June 1997, pp. 879-882.

[21] S. E. Alper, Y. Temiz, and T. Akin, “A Compact Angular Rate Sensor System Using a Fully Decoupled Silicon-on-Glass MEMS Gyroscope,” *Journal of Microelectromechanical Systems*, Vol. 17, No. 6, pp. 1418-1429, 2008.

[22] C. Acar and A. M. Shkel, “An Approach for Increasing Drive-Mode Bandwidth ”of MEMS Vibratory Gyroscopes,” *Journal of Microelectromechanical Systems*, Vol. 14, No. 3, pp. 520-528, 2005.

[23] E. Tatar, S. E. Alper, and T. Akin, “Effect of quadrature error on the performance of a fully-decoupled MEMS gyroscope,” *The 24th IEEE Int. MicroElectroMechanical Systems Conf. (MEMS 2011)*, pp.569-572, Cancun, Mexico, January 2011.

[24] K. Sahin, “A Wide-Bandwidth High-Sensitivity MEMS Gyroscope,” *M.S. Thesis*, Middle East Technical University, July 2008.

[25] Y. Temiz, “Advanced Readout and Control Electronics for MEMS Gyroscopes,” *M.S. Thesis*, Middle East Technical University, August 2007.

[26] N. Yazdi, H. Kulah, and K. Najafi, “Precision readout circuits for capacitive microaccelerometers,” *Proceedings of IEEE Sensors*, Vol.1, pp. 28 - 31, 2004.

[27] J. A. Geen, S. J. Sherman, J. F. Chang, and S. R. Lewis, “Singlechip Surface Micromachined Integrated Gyroscope with 50Â°/h Allan Deviation,” *IEEE Journal of Solid-State Circuits*, Vol. 37, pp.1860-1866, 2002.

[28] http://en.wikipedia.org/wiki/Allan_variance, Last access: 20.01.2010.

[29] IEEE Standard Specification Format Guide and Test Procdure for Single-Axis Interferometric Fiber Optic Gyros, *IEEE, Std 952-1997*, pp. 65, September 1997.

[30] J. Wu, G.K. Fedder, and L.R. Carley, “A low-noise low-offset capacitive sensing amplifier for a 50-μg/$\sqrt{Hz}$ monolithic CMOS MEMS accelerometer,” *IEEE Journal of Solid-State Circuits*, Vol. 39, May 2004, pp. 722-730.

[31] M. AbdelGhany, K.Khairallah, M. Elsayed, A. Emira, and S. Sedky, “A universal gyroscope driving circuit with 70dB amplitude control range,” *53rd IEEE International Midwest Symposium on Circuits and System (MWSCAS 2010)*, pp.252-255, 2010.

[32] B. R. Johnson, E. Cabuz, H. B. French, and R. Supino, “Development of a MEMS Gyroscope for Northfinding Applications,” *Position Location and Navigation Symposium (PLANS 2010)*, pp.168-170, 2010.

[33] B. Chaumet, B. Leverrier, C. Rougeot, and S. Bouyat, “A New Silicon Tuning Fork Gyroscope for Aerospace Applications,” *Symposium Gyro Technology*, pp. 1.1-1.13, Karlsruhe, Germany, September 2009.

[34] A. Makdissi, F. Vernotte, and E. De Clercq, “Stability Variances: A Filter Approach,” *IEEE Transactions on Ultrasonics, Ferroelectrics, and Frequency Control*, Vol. 57, no. 5, May 2010.

[35] IEEE Standard Specification Format Guide and Test Procedure for Coriolis Vibratory Gyros , *IEEE Std 1431-2004*, pp.1-69, 2004.

[36] Crossbow Technolog Inc. website, http://www.xbow.com/pdf/Bias_Stability_Measurement.pdf, Last access: 02.01.2010.

[37] Analog Devices, “AD8222 Precision, Dual-Channel Instrumentation Amplifier,” Datasheet, 2010.

[38] Analog Devices, “AD8608 Precision, Low Noise, CMOS, Rail-to-Rail, Input/Output Operational Amplifiers,” Datasheet, 2010.

[39] Analog Devices, “AD8630 Zero Drift, Single-Supply, Rail-to-Rail Input/Output Operational Amplifier,” Datasheet, 2010.

[40] Analog Devices, “AD630 Balanced Modulator/Demodulator,” Datasheet, 2004.

[41] T. Northemanna, M. Maurera, S. Rombacha, A. Buhmanna, and Y. Manolia, “A Digital Interface for Gyroscopes Controlling the Primary and Secondary Mode using Bandpass Sigma-Delta modulation,” *Sensors and Actuators A*, Vol. 162, pp. 388-393, 2010.

[42] L. Aaltonen and K. A. I. Halonen, “An Analog Drive Loop for a Capacitive MEMS Gyroscope,” *Analog Integrated Circuit and Signal Processing*, Vol. 63, pp. 465-476.

[43] A. Shaban, M. El-Badry, and A. El-Sayed, “Analysis and Design of Gyro-Drive Mode Loop with Amplitude Control,” *4th International Design and Test Workshop (IDT)*, pp. 1-4, 2009.

[44] Z. Wang, Z. Li, and W. Lu, “A New Self-Oscillation Loop for MEMS Vibratory Gyroscopes,” *7th International Conference on ASIC (ASICON ’07)*, pp. 1046-1049, 2007.

[45] Q. Zheng, L. Dong, D. H. Lee, and Z. Gao, “Active Disturbance Rejection Control for MEMS Gyroscopes,” *IEEE Transactions on Control Systems Technology*, Vol. 17, pp. 1432-1438,2009.

[46] A. Sharma, “CMOS Systems and Circuits for Sub-Degree per Hour MEMS Gyroscopes,” *Dissertation for the Degree of Doctor of Philosophy*, Georgia Institute of Technology, December 2007.

[47] M. W. Putty, “A Micromachined Vibrating Ring Gyroscope,” *Dissertation for the Degree of Doctor of Philosophy*, The University of Michigan, 1995.

[48] F. L. Lewis, *Applied Optimal Control and Estimation, Prentice-Hall*, 1992.

[49] W. A. Clark, “Micromachined Vibratory Rate Gyroscopes”, *Dissertation for the Degree of Doctor of Philosophy*, University of California, Berkeley, December 1997.

[50] S. Park and R. Horowitz, “Adaptive control for the conventional mode of operation of MEMS gyroscopes,” *J. Microelectromech. Syst. IEEE* Vol.12, pp.101-108, 2003.

[51] L. Dong, “Adaptive Control System for a Vibrational MEMS Gyroscope with Time-Varying with Rotation Rates,” *Dissertation for the Degree of Doctor of Philosophy*, The University of Alabama, May 2005.

[52] J. W. Song, J. G. Lee, T. Kang, Y. K. Kim, H. Chung, H. K. Chang, “Feedback Controller Design for an In-Plane Gimbaled Micro Gyroscope Using H∞ and State Weighted Model Reduction Techniques,” *Proc. ICCAS 2002*, Muju Resort, Korea, pp. 228-233, 2002.

[53] W. T. Sung, J. G. Lee, J. W. Song, and T. Kang T “H∞ Controller Design of MEMS Gyroscope and Its Performance Test,” *Proc. PLANS 2004*, Monterey, CA, USA, April 2004 pp. 63-69, 2004.

[54] N. Yazdi, F. Ayazi, and K. Najafi, “Micromachined Inertial Sensors,” *Proceedings of the IEEE*, Vol. 86, pp.1640-1659, 2002.

Appendix A

Derivations of Base-band Equivalent Models

A.1 Capacitive Interface, $\Phi = 90°$

$$p(t) = x(t) \cdot cos(\omega_D t) = x(t) \cdot \frac{e^{j\omega_D t} + e^{-j\omega_D t}}{2} \tag{A.1}$$

$$P(s) = X(s) * \frac{\delta(s + j\omega_D) + \delta(s - j\omega_D)}{2} = \frac{X(s + j\omega_D) + X(s - j\omega_D)}{2} \tag{A.2}$$

Output of this system equals to the multiplication of the input signal and transfer function of the sense mode of gyroscope.

$$R(s) = P(s) \cdot G(s) = \frac{X(s + j\omega_D) + X(s - j\omega_D)}{2} \cdot G(s) \tag{A.3}$$

Relation between demodulator output and gyroscope output is similar to the Eq. A.2. In this case, input is multiplied with sine signal, instead of cosine signal.

$$Z(s) = \frac{R(s + j\omega_D) - R(s - j\omega_D)}{2j} \tag{A.4}$$

$$Z(s) = \frac{X(s + 2j\omega_D) + X(s)}{4j} \cdot G(s + j\omega_D) - \frac{X(s) + X(s - 2j\omega_D)}{4j} \cdot G(s - j\omega_D) \tag{A.5}$$

$$\begin{aligned} Y(s) &= Z(s) \cdot F(s) \\ &= X(s) \cdot \frac{G(s + j\omega_D) - G(s - j\omega_D)}{4j} \\ &\quad + \underbrace{\left(\frac{X(s + 2j\omega_D)}{4j} \cdot G(s + j\omega_D) - \frac{X(s - 2j\omega_D)}{4j} \cdot G(s - j\omega_D)\right)}_{\text{Filtered out by the Low Pass Filter for band-limited input}} \cdot F(s) \\ &\cong X(s) \cdot \frac{G(s + j\omega_D) - G(s - j\omega_D)}{4j} \end{aligned} \tag{A.6}$$

Sense mode dynamics for capacitive preamplifier can be expressed in Eq. A.7.

$$G(s) = \frac{K_S}{s^2 + \frac{\omega_S}{Q_S} \cdot s + \omega_S^2} \tag{A.7}$$

where,

$$K_S = \underbrace{\frac{\partial C_{S,act}}{\partial x} \cdot V_{PM}}_{\alpha_{V/F}} \cdot \underbrace{\frac{\partial C_{S,sense}}{\partial x} \cdot V_{PM}}_{\alpha_{x/I}} \cdot \underbrace{\frac{1}{C_{Pre-amp}}}_{\alpha_{I/V}} \cdot \frac{1}{m_S}$$

Eq. A.7 can be expanded as Eq. A.8 shows.

$$G(s) = \frac{K_S}{2j\omega_S\sqrt{1-1/4Q_S^2}} \left(\frac{1}{s + \dfrac{\omega_S}{2 \cdot Q_S} - j\omega_S\sqrt{1-1/4Q_S^2}} - \frac{1}{s + \dfrac{\omega_S}{2 \cdot Q_S} + j\omega_S\sqrt{1-1/4Q_S^2}} \right) \tag{A.8}$$

Inserting Eq. A.8 into Eq. A.6, Eq. A.9 is obtained.

$$\begin{aligned} Y(s) = X(s) \cdot F(s) \cdot \frac{K_S}{-8\omega_S\sqrt{1-\dfrac{1}{4Q_S^2}}} &\left(\frac{1}{s + \dfrac{\omega_S}{2 \cdot Q_S} - j\omega_S\sqrt{1-1/4Q_S^2} + j\omega_D} \right. \\ - \frac{1}{s + \dfrac{\omega_S}{2 \cdot Q_S} - j\omega_S\sqrt{1-1/4Q_S^2} - j\omega_D} &- \frac{1}{s + \dfrac{\omega_S}{2 \cdot Q_S} + j\omega_S\sqrt{1-1/4Q_S^2} + j\omega_D} \\ \left. + \frac{1}{s + \dfrac{\omega_S}{2 \cdot Q_S} + j\omega_S\sqrt{1-1/4Q_S^2} - j\omega_D} \right) & \end{aligned} \tag{A.9}$$

Combining the conjugate terms, Eq. A.9 takes the following form.

$$\begin{aligned} Y(s) = X(s) \cdot F(s) \cdot \frac{K_S}{-8\omega_S\sqrt{1-\dfrac{1}{4Q_S^2}}} &\left(\frac{2\left(s + \dfrac{\omega_S}{2 \cdot Q_S}\right)}{s^2 + \dfrac{\omega_S}{Q_S} \cdot s + \underbrace{\left(\dfrac{\omega_S}{4Q_S}\right)^2 + \left(\omega_S\sqrt{1-\dfrac{1}{4Q_S^2}} + w_D\right)^2}_{\omega_H^2}} \right. \\ &\left. - \frac{2\left(s + \dfrac{\omega_S}{2 \cdot Q_S}\right)}{s^2 + \dfrac{\omega_S}{Q_S} \cdot s + \underbrace{\left(\dfrac{\omega_S}{4Q_S}\right)^2 + \left(\omega_S\sqrt{1-\dfrac{1}{4Q_S^2}} - w_D\right)^2}_{\omega_L^2}} \right) \end{aligned} \tag{A.10}$$

This equation also shows two resonator system: one of them has a resonance frequency around ω_H and other has a resonance frequency around ω_L. Second term, whose resonance frequency is around ω_L, is rejected by the low pass filter. Thus, over-all system is expressed by Eq.A.11.

$$Y(s) = X(s)\cdot F(s)\cdot \frac{-K_S}{4\omega_S\sqrt{1-\dfrac{1}{4Q_S^2}}}\cdot\frac{s+\dfrac{\omega_S}{2\cdot Q_S}}{s^2+\underbrace{\dfrac{\omega_S}{Q_S}}_{\beta_S}\cdot s+\omega_L^2} \tag{A.11}$$

Moreover the gyroscope is operating at high vacuum levels. This fact allows us to neglect $1/4Q_S^2$ expression in the above equation.

$$\boxed{G_{env}(s) = -\frac{K_S\cdot F(s)}{4\omega_S}\cdot\frac{s+\dfrac{\omega_S}{2\cdot Q_S}}{s^2+\beta_S\cdot s+\omega_L^2}} \tag{A.12}$$

A.2 Resistive Interface, $\Phi = 0°$

$$p(t) = x(t)\cdot cos(\omega_D t) = x(t)\cdot\frac{e^{j\omega_D t}+e^{-j\omega_D t}}{2} \tag{A.13}$$

$$P(s) = X(s) * \frac{\delta(s+j\omega_D)+\delta(s-j\omega_D)}{2} = \frac{X(s+j\omega_D)+X(s-j\omega_D)}{2} \tag{A.14}$$

Output of this system equals to the multiplication of the input signal and transfer function of the sense mode of gyroscope.

$$R(s) = P(s)\cdot G(s) = \frac{X(s+j\omega_D)+X(s-j\omega_D)}{2}\cdot G(s) \tag{A.15}$$

Relation between demodulator output and gyroscope output is same as Eq. A.14.

$$Z(s) = \frac{R(s+j\omega_D)+R(s-j\omega_D)}{2} \tag{A.16}$$

$$Z(s) = \frac{X(s+2j\omega_D)+X(s)}{4}\cdot G(s+j\omega_D)+\frac{X(s)+X(s-2j\omega_D)}{4}\cdot G(s-j\omega_D) \tag{A.17}$$

$$\begin{aligned}
Y(s) &= Z(s)\cdot F(s)\\
&= X(s)\cdot\frac{G(s+j\omega_D)+G(s-j\omega_D)}{4}\\
&\quad+\underbrace{\left(\frac{X(s+2j\omega_D)}{2}\cdot G(s+j\omega_D)+\frac{X(s-2j\omega_D)}{4}\cdot G(s-j\omega_D)\right)}_{\text{Filtered out by the Low Pass Filter for band-limited input}}\cdot F(s)\\
&\cong X(s)\cdot\frac{G(s+j\omega_D)+G(s-j\omega_D)}{4}
\end{aligned} \tag{A.18}$$

Sense mode dynamics for resistive preamplifier can be expressed in Eq. A.19.

$$G(s)=\frac{K_S\cdot s}{s^2+\dfrac{\omega_S}{Q_S}\cdot s+\omega_S^2}\tag{A.19}$$

where,

$$K_S=\underbrace{\frac{\partial C_{S,act}}{\partial x}\cdot V_{PM}}_{\alpha_{V/F}}\cdot\underbrace{\frac{\partial C_{S,sense}}{\partial x}\cdot V_{PM}}_{\alpha_{x/I}}\cdot\underbrace{R_{Pre-amp}}_{\alpha_{I/V}}\cdot\frac{1}{m_S}$$

Eq. A.19 can be expanded as Eq. A.20 shows.

$$\begin{aligned}G(s)=\frac{K_S}{2j\omega_S\sqrt{1-1/4Q_S^2}}&\left(\frac{-\dfrac{\omega_S}{2\cdot Q_S}+j\omega_S\sqrt{1-1/4Q_S^2}}{s+\dfrac{\omega_S}{2\cdot Q_S}-j\omega_S\sqrt{1-1/4Q_S^2}}\right.\\&\left.-\frac{-\dfrac{\omega_S}{2\cdot Q_S}-j\omega_S\sqrt{1-1/4Q_S^2}}{s+\dfrac{\omega_S}{2\cdot Q_S}+j\omega_S\sqrt{1-1/4Q_S^2}}\right)\end{aligned}\tag{A.20}$$

Inserting Eq. A.35 into Eq. A.33, Eq.A.21 is obtained.

$$\begin{aligned}Y(s)=X(s)\cdot F(s)\cdot\frac{K_S}{8j\omega_S\sqrt{1-\dfrac{1}{4Q_S^2}}}&\left(\frac{-\dfrac{\omega_S}{2\cdot Q_S}+j\omega_S\sqrt{1-1/4Q_S^2}}{s+\dfrac{\omega_S}{2\cdot Q_S}-j\omega_S\sqrt{1-1/4Q_S^2}+j\omega_D}\right.\\-\frac{-\dfrac{\omega_S}{2\cdot Q_S}+j\omega_S\sqrt{1-1/4Q_S^2}}{s+\dfrac{\omega_S}{2\cdot Q_S}-j\omega_S\sqrt{1-1/4Q_S^2}-j\omega_D}&+\frac{-\dfrac{\omega_S}{2\cdot Q_S}-j\omega_S\sqrt{1-1/4Q_S^2}}{s+\dfrac{\omega_S}{2\cdot Q_S}+j\omega_S\sqrt{1-1/4Q_S^2}+j\omega_D}\\&\left.-\frac{-\dfrac{\omega_S}{2\cdot Q_S}-j\omega_S\sqrt{1-1/4Q_S^2}}{s+\dfrac{\omega_S}{2\cdot Q_S}+j\omega_S\sqrt{1-1/4Q_S^2}-j\omega_D}\right)\end{aligned}\tag{A.21}$$

Combining the conjugate terms, Eq. A.21 takes the following form.

$$
\begin{aligned}
Y(s) =& X(s) \cdot F(s) \cdot \frac{K_S}{8 j\omega_S \sqrt{1 - \dfrac{1}{4Q_S^2}}} \qquad \text{(A.22)} \\
&\cdot \left(\frac{-2j\omega_S \left(\dfrac{1}{2 \cdot Q_S} \cdot \left(\omega_S \sqrt{1 - 1/4Q_S^2} + \omega_D \right) + \left(s + \dfrac{\omega_S}{2 \cdot Q_S} \right) \sqrt{1 - 1/4Q_S^2} \right)}{s^2 + \dfrac{\omega_S}{Q_S} \cdot s + \underbrace{\left(\dfrac{\omega_S}{4Q_S} \right)^2 + \left(\omega_S \sqrt{1 - \dfrac{1}{4Q_S^2}} + w_D \right)^2}_{\omega_H^2}} \right. \\
&\left. - \frac{-2j\omega_S \left(\dfrac{1}{2 \cdot Q_S} \cdot \left(\omega_S \sqrt{1 - 1/4Q_S^2} - \omega_D \right) + \left(s + \dfrac{\omega_S}{2 \cdot Q_S} \right) \sqrt{1 - 1/4Q_S^2} \right)}{s^2 + \dfrac{\omega_S}{Q_S} \cdot s + \underbrace{\left(\dfrac{\omega_S}{4Q_S} \right)^2 + \left(\omega_S \sqrt{1 - \dfrac{1}{4Q_S^2}} - w_D \right)^2}_{\omega_L^2}} \right) \qquad \text{(A.23)}
\end{aligned}
$$

This equation also shows two resonator system: one of them has a resonance frequency around ω_H and other has a resonance frequency around ω_L. Second term, whose resonance frequency is around ω_L, is rejected by the low pass filter. Thus, over-all system is expressed by Eq.A.25.

$$
\begin{aligned}
Y(s) =& X(s) \cdot F(s) \cdot \frac{K_S}{8 j\omega_S \sqrt{1 - \dfrac{1}{4Q_S^2}}} \qquad \text{(A.24)} \\
&\cdot \frac{-2j\omega_S \left(\dfrac{1}{2 \cdot Q_S} \cdot \left(\omega_S \sqrt{1 - 1/4Q_S^2} - \omega_D \right) + \left(s + \dfrac{\omega_S}{2 \cdot Q_S} \right) \sqrt{1 - 1/4Q_S^2} \right)}{s^2 + \dfrac{\omega_S}{Q_S} \cdot s + \left(\dfrac{\omega_S}{4Q_S} \right)^2 + \left(\omega_S \sqrt{1 - \dfrac{1}{4Q_S^2}} - w_D \right)^2} \qquad \text{(A.25)}
\end{aligned}
$$

Assuming, sense and drive mode resonance frequencies are much higher than the frequency separation and quality factor is high, above expression is simplified as followings:

$$
Y(s) = X(s) \cdot \frac{K_S \cdot F(s)}{4} \cdot \frac{s + \dfrac{\omega_S}{2 \cdot Q_S}}{s^2 + \beta_S \cdot s + \omega_L^2} \tag{A.26}
$$

Therefore, base-band equivalent model can be found as:

$$\boxed{G_{env}(s) = \frac{K_S \cdot F(s)}{4} \cdot \frac{s + \dfrac{\omega_S}{2 \cdot Q_S}}{s^2 + \beta_S \cdot s + \omega_L^2}} \tag{A.27}$$

A.3 Resistive Interface, $\Phi = 90°$

$$p(t) = x(t) \cdot cos(\omega_D t) = x(t) \cdot \frac{e^{j\omega_D t} + e^{-j\omega_D t}}{2} \tag{A.28}$$

$$P(s) = X(s) * \frac{\delta(s + j\omega_D) + \delta(s - j\omega_D)}{2} = \frac{X(s + j\omega_D) + X(s - j\omega_D)}{2} \tag{A.29}$$

Output of this system equals to the multiplication of the input signal and transfer function of the sense mode of gyroscope.

$$R(s) = P(s) \cdot G(s) = \frac{X(s + j\omega_D) + X(s - j\omega_D)}{2} \cdot G(s) \tag{A.30}$$

Relation between demodulator output and gyroscope output is similar to the Eq. A.29. In this case, input is multiplied with sine signal, instead of cosine signal.

$$Z(s) = \frac{R(s + j\omega_D) - R(s - j\omega_D)}{2j} \tag{A.31}$$

$$Z(s) = \frac{X(s + 2j\omega_D) + X(s)}{4j} \cdot G(s + j\omega_D) - \frac{X(s) + X(s - 2j\omega_D)}{4j} \cdot G(s - j\omega_D) \tag{A.32}$$

$$\begin{aligned}
Y(s) &= Z(s) \cdot F(s) \\
&= X(s) \cdot \frac{G(s + j\omega_D) - G(s - j\omega_D)}{4j} \\
&\quad + \underbrace{\left(\frac{X(s + 2j\omega_D)}{4j} \cdot G(s + j\omega_D) - \frac{X(s - 2j\omega_D)}{4j} \cdot G(s - j\omega_D) \right)}_{\text{Filtered out by the Low Pass Filter for band-limited input}} \cdot F(s) \\
&\cong X(s) \cdot \frac{G(s + j\omega_D) - G(s - j\omega_D)}{4j}
\end{aligned} \tag{A.33}$$

As it is given above, sense mode dynamics for resistive preamplifier can be expressed in Eq. A.34.

$$G(s) = \frac{K_S \cdot s}{s^2 + \dfrac{\omega_S}{Q_S} \cdot s + \omega_S^2} \tag{A.34}$$

where,

$$K_S = \underbrace{\frac{\partial C_{S,act}}{\partial x} \cdot V_{PM}}_{\alpha_{V/F}} \cdot \underbrace{\frac{\partial C_{S,sense}}{\partial x} \cdot V_{PM}}_{\alpha_{x/I}} \cdot \underbrace{R_{Pre-amp}}_{\alpha_{I/V}} \cdot \frac{1}{m_S}$$

Eq. A.34 can be expanded as Eq. A.35 shows.

$$G(s) = \frac{K_S}{2j\omega_S\sqrt{1-1/4Q_S^2}}\left(\frac{-\frac{\omega_S}{2\cdot Q_S} + j\omega_S\sqrt{1-1/4Q_S^2}}{s+\frac{\omega_S}{2\cdot Q_S} - j\omega_S\sqrt{1-1/4Q_S^2}} - \frac{-\frac{\omega_S}{2\cdot Q_S} - j\omega_S\sqrt{1-1/4Q_S^2}}{s+\frac{\omega_S}{2\cdot Q_S} + j\omega_S\sqrt{1-1/4Q_S^2}}\right) \tag{A.35}$$

Inserting Eq. A.35 into Eq. A.33, Eq. A.36 is obtained.

$$\begin{aligned} Y(s) = X(s)\cdot F(s)\cdot \frac{K_S}{-8\omega_S\sqrt{1-\frac{1}{4Q_S^2}}}\Bigg(&\frac{-\frac{\omega_S}{2\cdot Q_S} + j\omega_S\sqrt{1-1/4Q_S^2}}{s+\frac{\omega_S}{2\cdot Q_S} - j\omega_S\sqrt{1-1/4Q_S^2} + j\omega_D} \\ &- \frac{-\frac{\omega_S}{2\cdot Q_S} + j\omega_S\sqrt{1-1/4Q_S^2}}{s+\frac{\omega_S}{2\cdot Q_S} - j\omega_S\sqrt{1-1/4Q_S^2} - j\omega_D} - \frac{-\frac{\omega_S}{2\cdot Q_S} - j\omega_S\sqrt{1-1/4Q_S^2}}{s+\frac{\omega_S}{2\cdot Q_S} + j\omega_S\sqrt{1-1/4Q_S^2} + j\omega_D} \\ &+ \frac{-\frac{\omega_S}{2\cdot Q_S} - j\omega_S\sqrt{1-1/4Q_S^2}}{s+\frac{\omega_S}{2\cdot Q_S} + j\omega_S\sqrt{1-1/4Q_S^2} - j\omega_D}\Bigg) \end{aligned} \tag{A.36}$$

Combining the conjugate terms, Eq. A.36 takes the following form.

$$Y(s) = X(s)\cdot F(s)\cdot \frac{K_S}{-8\omega_S\sqrt{1-\frac{1}{4Q_S^2}}} \tag{A.37}$$

$$\begin{aligned} \cdot\Bigg(&\frac{-\frac{\omega_S}{Q_S}\cdot s - \frac{\omega_S^2}{2\cdot Q_S^2} + 2\cdot\omega_S\cdot\sqrt{1-\frac{1}{4Q_S^2}}\cdot\left(\omega_D + \sqrt{1-\frac{1}{4Q_S^2}}\cdot\omega_S\right)}{s^2 + \frac{\omega_S}{Q_S}\cdot s + \underbrace{\left(\frac{\omega_S}{4Q_S}\right)^2 + \left(\omega_S\sqrt{1-\frac{1}{4Q_S^2}} + w_D\right)^2}_{\omega_H^2}} \\ &-\frac{-\frac{\omega_S}{Q_S}\cdot s - \frac{\omega_S^2}{2\cdot Q_S^2} + 2\cdot\omega_S\cdot\sqrt{1-\frac{1}{4Q_S^2}}\cdot\left(\omega_D - \sqrt{1-\frac{1}{4Q_S^2}}\cdot\omega_S\right)}{s^2 + \frac{\omega_S}{Q_S}\cdot s + \underbrace{\left(\frac{\omega_S}{4Q_S}\right)^2 + \left(\omega_S\sqrt{1-\frac{1}{4Q_S^2}} - w_D\right)^2}_{\omega_L^2}}\Bigg) \end{aligned} \tag{A.38}$$

This equation also shows two resonator system: one of them has a resonance frequency around ω_H and other has a resonance frequency around ω_L. Second term, whose resonance frequency is around ω_L, is rejected by the low pass filter. Thus, over-all system is expressed by Eq.A.40.

$$Y(s) = X(s) \cdot F(s) \cdot \frac{K_S}{-8\omega_S \sqrt{1 - \dfrac{1}{4Q_S^2}}} \tag{A.39}$$

$$\cdot \frac{-\dfrac{\omega_S}{Q_S} \cdot s - \dfrac{\omega_S^2}{2 \cdot Q_S^2} + 2 \cdot \omega_S \cdot \sqrt{1 - \dfrac{1}{4Q_S^2}} \cdot \left(\omega_D - \sqrt{1 - \dfrac{1}{4Q_S^2}} \cdot \omega_S\right)}{s^2 + \dfrac{\omega_S}{Q_S} \cdot s + \left(\dfrac{\omega_S}{4Q_S}\right)^2 + \left(\omega_S \sqrt{1 - \dfrac{1}{4Q_S^2}} - w_D\right)^2} \tag{A.40}$$

Using Taylor's series approximation, numerator can be simplified as followings:

$$\sqrt{1 - x} \cong 1 - \frac{x}{2} \Rightarrow \sqrt{1 - \frac{1}{4Q_S^2}} \cong 1 - \frac{1}{8Q_S^2} \tag{A.41}$$

With the assumption of a high quality factor, Eq. A.40 is simplified to:

$$Y(s) = X(s) \cdot F(s) \cdot \frac{K_S}{4} \cdot \frac{\dfrac{s}{2 \cdot Q_S} + \Delta\omega + \dfrac{\omega_D}{8Q_S^2}}{s^2 + \beta_S \cdot s + \omega_L^2} \tag{A.42}$$

Therefore, base-band equivalent model can be found as:

$$\boxed{G_{env}(s) = \frac{K_S \cdot F(s)}{4} \cdot \frac{\dfrac{s}{2 \cdot Q_S} + \Delta\omega + \dfrac{\omega_D}{8Q_S^2}}{s^2 + \beta_S \cdot s + \omega_L^2}} \tag{A.43}$$